AFOSR-TR-0693

REPORT DOCUMENTATION PAGE

Form Approved
OMB No. 0704-0188

1. AGENCY USE ONLY *(Leave blank)*	2. REPORT DATE	3. REPORT TYPE AND DATES COVERED
	October 31, 1997	Final Report for September 15, 1996 - May 31, 1997

4. TITLE AND SUBTITLE
Transformation Weakening of Ceramic Composite Interfaces

5. FUNDING NUMBERS
AFOSR 49620-96-1-0464

6. AUTHOR(S)
Professor Waltraud M. Kriven

7. PERFORMING ORGANIZATION NAME(S) AND ADDRESS(ES)
University of Illinois at Urbana-Champaign
Dept. of Materials Science and Engineering
1304 W. Green Street
Urbana, IL 61801

8. PERFORMING ORGANIZATION REPORT NUMBER

9. SPONSORING / MONITORING AGENCY NAME(S) AND ADDRESS(ES)
AFOSR/NC, Division of Chemistry and Materials Science
110 Duncan Ave., Suite B115
Bolling AFB, DC 20332-0001

NA

10. SPONSORING / MONITORING AGENCY REPORT NUMBER

11. SUPPLEMENTARY NOTES

12a. DISTRIBUTION / AVAILABILITY STATEMENT
Public Availability
Approved for public release; distribution unlimited.

DTIC QUALITY INSPECTED 2

12b. DISTRIBUTION CODE

13. ABSTRACT *(Maximum 200 words)*

A new concept for achieving graceful failure in oxide composites is studied. It is based on debonding of a weak interphase between a matrix and an interphase in a laminated composite. The interphase can be thermally or shear stress induced by transformation weakening, which results from an accompanying significant volume contraction and/or unit cell shape change, on cooling from a high temperature to low temperature crystal structure. Mullite/cordierite laminates with a $\beta \rightarrow \alpha$-cristobalite transformation weakened interphase were investigated in order to demonstrate interphase debonding behavior. The laminate showed fracture behavior dependent on a critical size effect. The grain size of polycrystalline β-cristobalite was controlled by annealing. With increasing annealing time, the strength decreased due to the formation of internal microcracks in the cristobalite layer which occurred spontaneously during thermally-induced transformation. A hot-pressed laminate, annealed for 10 h at 1300 °C, had an average grain size of 4.2 μm and a strength of 131 MPa. Its work of fracture was 2.38 kJ/m^2 with a non-catastrophic fracture behavior. The indentation response indicated crack deflection along the cristobalite debonding interphase.

14. SUBJECT TERMS	15. NUMBER OF PAGES
Transformation weakening of interphases, mullite-cordierite laminates, cristobalite interphase, debonding, toughening mechanism, thermally-induced, shear-induced transformation	119
	16. PRICE CODE

17. SECURITY CLASSIFICATION OF REPORT	18. SECURITY CLASSIFICATION OF THIS PAGE	19. SECURITY CLASSIFICATION OF ABSTRACT	20. LIMITATION OF ABSTRACT

EXTRA

CERAMICS DIVISION

MATERIALS SCIENCE AND ENGINEERING

University of Illinois

Urbana, Illinois

TRANSFORMATION WEAKENING OF CERAMIC COMPOSITE INTERFACES

A final research report for grant number
F49620-96-1-0464

FINAL REPORT
For the period Sept 15th 1996 to May 31st 1997

Oct 31st 1997

Prepared for:
Dr. Alexander Pechenik
Program Manager,
Directorate of Chemistry and Materials Science,
AFOSR
110 Duncan Ave, Suite B115,
Bolling Air Force Base, DC 20332-0001

Prepared by:

The University of Illinois at Urbana-Champaign,
Department of Materials Science and Engineering,
1304 West Green St., Urbana, IL 61801

Principal Investigator
Professor Waltraud M. Kriven

Table of Contents

Section 1. Introduction and Overall Objectives 3
2. Accomplishments 4
3. Personnel Supported 4
4. Publications 5
5. Interactions/Transitions 5
6. New Discoveries, Inventions or Patents 7
7. Honors/Awards 7
8. Synopsis of Theses 8
9. Reprints and Preprints 8

SECTION I INTRODUCTION AND OVERALL OBJECTIVES

Introduction to transformation weakening of interfaces

The concept of "phase transformation weakening" introduced by Professor Kriven has led to the search for a displacive or martensitic phase transformation with a negative volume change or large shape change at fiber/matrix or laminate/matrix interfaces (see Table 1). Several materials are considered to be promising candidates as "phase transformation weakeners". Preliminary studies have been conducted on enstatite (MgO. SiO_2 or $MgSiO_3$), which is accompanied by a 5.5 % volume contraction on transformation. In applying such a phase transformation, a distinction is drawn between a thermally induced transformation and a shear stress induced transformation. Figure 1 illustrates a mechanism for shear stress induced weakening of an interface and thereby, overall toughening of a composite. The difference between a shear induced mechanism and a thermally induced one is that in the latter, all the interfacial grains have already been transformed prior to crack approach.

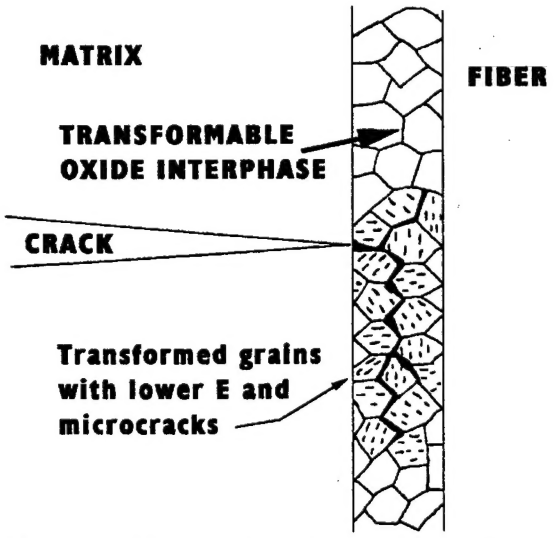

Fig. 1 Schematic diagram illustrating "transformation weakening of ceramic interphases" leading to overall toughening of a ceramic matrix composite. In thermally induced transformations, all interphases are pre-transformed before the approach of a crack with some consequent loss of overall strength of the material. In the ideal shear-stress induced case, an on-coming crack induces a transformation in is immediate environment, with strength only minimally reduced throughout the bulk. Maximum toughening is achieved since the propagating crack need to do work to overcome the nucleation barrier and cause transformation, and onset of the other synergistic toughening mechanisms occurs.

Thus, fiber/matrix interfaces in ceramic matrix composites must be sufficiently strong to provide for mechanical integrity of the composites, but also weak enough to prevent transition of cracks from matrix to fibers. This project explores a fundamentally new concept of a "variable-strength"

interface, viz., one that is strong when no cracks are present, but suddenly weakens and arrests the propagation of a crack when it arrives near such an interface. The effect is produced by coating ceramic fibers with a thin layer of a ceramic material capable of quick, stress-induced transformation with a negative volume change and/or a large unit cell shape change.

Overall Objectives

Thus, the objective of this work was to investigate a novel concept for developing superior fiber-matrix interfaces in ceramic matrix composites by utilizing the "transformation weakening effect." Since many of the transformable phases are oxides, this work opens the door to high temperature, oxidation resistant composites. The proposed transformation weakening mechanism for toughening of fiber-reinforced, oxide, ceramic composites is illustrated in Fig. 1.

In this work the concept would be tested on model laminate systems, using processing, mechanical evaluaiton and microstructure characterization techniques of XRD, SEM, TEM, HVEM , to measure the amount of transformed material.

SECTION 2. ACCOMPLISHMENTS

The main accomplishments of this work have been written up and submitted for publication. They are presented in Section 9 of this report as reprints and preprints.

SECTION 3. PERSONNEL SUPPORTED

- Professor Waltraud M. Kriven (PI).
- Dr. Dong Zhu, mechanical testing expert was partially supported on this grant and for six months on an AFOSR STTR with Containerless Research Incorporated.
- Dr. Sang Jin Lee, processing expert, visiting scientist with partial funding for living expenses, from Korea. Supplemented his salary at $16,000 per annum for 1 year.
- Mr. My H. Nguyen, for operating expenses; student worked as a teaching assistant.

SECTION 4. PUBLICATIONS

Journal Papers:

- "Synthesis and Microstructure of Mullite Fibers Grown From Deeply Undercooled Melts," W. M. Kriven, D. Zhu and M. H. Jilavi, K. R. Weber, B. Cho, J. Felten, and P. C. Nordine. Ceramic Microstructures '96, edited by A. P. Tomsia and A. M. Glaeser, Plenum Pub., (1997) in press.

- "Shear Induced Transformation and Plasticity in Enstatite," D. Zhu and W. M. Kriven, J. Am. Ceram. Soc., accepted.

- "Crystallization and Densification of Nano-size, Amorphous Cordierite Powder Prepared by a Solution-Polymerization Route," S. J. Lee and W. M. Kriven, J. Amer. Ceram. Soc., submitted.

- "Toughening of Ceramic Composites by Transformation Weakening of Ceramic Interphases. Part I: Powder Preparation and Critical Size Effect," S. J. Lee and W. M. Kriven, J. Amer. Ceram. Soc., submitted.

- "Toughening of Ceramic Composites by Transformation Weakening of Ceramic Interphases. Part II: Mullite/Cordierite Laminate with β-cristobalite Interphase," W. M. Kriven and S. J. Lee, J. Am. Ceram. Soc., submitted.

- "Polymerized Organic-Inorganic Synthesis of Mixed Oxides," M. A. Gulgun, M. H. Nguyen and W. M. Kriven, J. Amer. Ceram. Soc., submitted.

Conference Proceedings:

- "Microstructure and Interfacial Properties of a Laser Ablation Coated, Fiber-Reinforced Ceramic Composite," D. Zhu, H. Chung, M. Jilavi, W. M. Kriven, and J. Mazumder, Cer. Eng and Sci. Proc. **18** [3] (1997) 105-112.

- "Synthesis and Characterization of Mullite and YAG Fibers Grown from Deeply Undercooled Melts," D. Zhu, M. H. Jilavi, W. M. Kriven. Cer. Eng. and Sci. **18** [3] (1997) 31-38.

SECTION 5. INTERACTIONS/TRANSITIONS

(a) Participation at meetings, conferences, seminars

Invited lectures and seminars

- "Displacive Transformations and their Applications in Structural Ceramics," W. M. Kriven* Invited lecture presented at the Crystallographic Colloquium, Institut fur Kristallographie und Angewandte Mineralogie der Ludwig-Maximilian-Universitat Munchen, Theresienstrasse 41, D-80333 Munchen; per Professor F. Frey, 16th May 1997.

- "Chemical Synthesis of Oxide Powders via Polymeric Stearic Entrappment," W. M. Kriven. * Invited lecture per Professor Peter Greil (Head), presented at the Institute of Werkstoffwissenschaften III, (Materials Science) University of Erlangen-Nurnberg, Germany, June 1997.

Conference Presentations

- "Interfacial Modification of Fiber Reinforced Cement Composites, C. M. Huang,* C. Y. Yuh, D. Zhu and W. M. Kriven. [Abstract #HH8.3] presented at the Materials Research Society Fall Annual Meeting, Boston MA, Dec 2-6 (1996).

- "Oxide Laminates with High Strength and Work of Fracture," D. H. Kuo* and W. M. Kriven, Invited paper [abstract # W12.6] presented at the Materials Research Society Fall Annual Meeting, Boston MA, Dec 2-6 (1996).

- "Electron Microscopy Characterization and Evaluation of Oxide Fibers," D. Zhu, M. H. Jilavi and W. M. Kriven.* Abstract [#C-0023-97F] presented at the 21st Annual Cocoa Beach Conference and Exposition Jan 12-16th (1997), Cocoa Beach, Florida.

- "Laser Ablated Oxide Coatings for Oxide Fibers," M. H. Jilavi, W. M. Kriven,* H. Chung, and J. Mazumder. Abstract [#C-0006-97F] presented at the 21st Annual Cocoa Beach Conference and Exposition Jan 12-16th (1997), Cocoa Beach, Florida.

- "A Novel Technique for Producing Ceramic Fibers," J. J. Felten*, J. K. R. Weber, P. C. Nordine, B. Cho, N. Lockwood, W. M. Kriven, M. H. Jilavi, and D. Zhu. Abstract [# C-0018-97F] presented at the 21st Annual Cocoa Beach Conference and Exposition Jan 12-16th (1997), Cocoa Beach, Florida.

- "Fabrication, Microstructure and Mechanical Response of Zirconia Containing Lanthanum Phosphate and Yttrium Phosphate Laminates," D. H. Kuo* and W. M. Kriven. Abstract [#C-0165-97F] presented at the

21st Annual Cocoa Beach Conference and Exposition Jan 12-16th (1997), Cocoa Beach, Florida.

(b) Consultative and advisory functions

None

(c) Transitions

- A Science and Technology Transfer (STTR) contract with the Containerless Research Inc., Evanston, IL, was awarded for directional crystallization of oxide (e.g., mullite and YAG) fibers. Contract is through the AFOSR and is due to start on Oct 1st 1996 for six months.

(d) Interdisciplinary Collaborations

- Feb 1997 - July 1997 (inclusive)
  Visiting professor on sabbatical leave at :
  The Institut fur Kristallographie und Angewandte Mineralogie,
  (Institute for Crystallography and Applied Mineralogy)
  Ludwig-Maximilians-Universitat, Munchen
  Theresienstrasse 41,
  D 80333 Munchen, Germany

- Have co-authored three publications with Professor Thomas Mackin, Assistant Professor, Dept. of Mechanical and Industrial Engineering, UIUC.

SECTION 6. NEW DISCOVERIES, PATENTS OR PATENT DISCLOSURES

None

SECTION 7. HONORS OR AWARDS

None

Received prior to Grant period

- Fellow of the American Ceramic Society, 1995.

- Brunauer Award (1988), jointly with Dr. C.J. Chan. and Prof. J.F. Young. Awarded by the Cements Division of the American Ceramic Society, for the Best Paper of the Year.

- Brunauer Award (1991), jointly with Dr. O.O. Popoola and Prof. J.F. Young. Awarded by the Cements Division of the American Ceramic Society, for the Best Paper of the Year.

SECTION 8 SYNOPIS OF THESIS

None

SECTION 9 REPRINTS AND PREPRINTS

Toughening of Ceramic Composites by Transformation Weakening of Interphases (Part I. Powder Preparation and Critical Size Effect of Chemically Stabilized β-cristobalite)

Sang-Jin Lee* and Waltraud M. Kriven*

Department of Materials Science and Engineering, University of Illinois at Urbana-Champaign, Urbana, Illinois 61801, USA

Abstract

A chemically stabilized β-cristobalite, which shows phase transformation weakening behavior, was prepared by a solution-polymerization route employing PVA solution as an organic carrier. Ca^{2+} and Al^{3+} cations were used as the stabilizers. An amorphous-type cristobalite powder with an average particle size of 0.3 μm and BET specific surface area of 80 m^2/g was prepared by a ball-milling for 12 h after calcination at 750 °C for 1 h.

The cubic(β)-to-tetragonal(α) phase transformation in polycrystalline β-cristobalite was induced at ≈180 °C on cooling. Like other materials exhibiting transformation toughening, a critical size effect controlled the β-to-α transformation. The grain size was controlled by varying the annealing time at 1300 °C. Pellets, both densified under hot pressing or under pressureless sintering conditions, had some cracks in the internal texture after annealing. The cracks occurred spontaneously during the cooling process, and were observed in samples with an average grain size of 5 μm or above. In the case of the hot-pressed sample, extensive cracking was observed after annealing times of 30 h or more. During annealing, a higher initial grain growth rate was observed in the case of hot-pressed samples than in the case of pressureless-sintered samples. Shear stress-induced transformation was also observed on grinding the specimens. An increase of about 13 vol% α-cristobalite by stress-induced transformation was measured in hot-pressed specimens after 12 h annealing.

* Members, The American Ceramic Society.

I. Introduction

In the search for ceramic composite materials which are tough or exhibit "graceful failure," it is now well established that toughening results from debonding at an interface between a matrix and a reinforcing phase.[1,2] The latter can take the form of fibers and weaves, second phase particulates or platelets, or the composite may have a laminated structure with a weak interphase.[3-7] Interfacial debonding is a crucial step leading to crack energy dissipation, such as frictional sliding at the interface with a resulting load transfer to the reinforcing fibers.

A new concept of "phase transformation weakening" of an interfacial interphase has recently been introduced.[8-10] It proposes that debonding between a matrix and reinforcement can be achieved by inducing a displacive, crystallographic phase transformation, which is accompanied by a negative volume and/or unit cell shape change, and which can cause tensile or shear stresses and possibly microcracking in the interphase. The associated energy dissipative mechanisms and debonding result in an overall increase in the toughness of the bulk composite. β-cristobalite (SiO_2) has been chosen as a low temperature model system in which to study the transformation weakening effect.

β-cristobalite is a high temperature, low pressure polymorph of silica (SiO_2) in which the SiO_4 tetrahedra are arranged in a diamond-like lattice with shared corners.[11] The β-cristobalite has cubic symmetry while α is tetragonal. The fully expanded, high temperature, β structure undergoes a reversible displacive transformation to a collapsed α structure on cooling at 265 °C. This is accompanied by a volume decrease of approximately 3.2%.[12,13] The temperature of the α ⇔ β inversion in cristobalite is variable and depends on the crystal structure of the starting material.[13,14] In order to stabilize the β-cristobalite down to room temperature, it can be chemically doped with "stuffing" cations.[15,16] In particular, in the CaO-Al_2O_3-SiO_2 system, the molar ratio of calcium oxide to alumina is one in which aluminum occupies a silicon tetrahedral site, while the calcium ion occupies all the interstitial non-framework sites.[17-19] The presence of foreign ions in the interstices presumably inhibits the contraction of the structure, which would normally occur during the α ⇔ β cristobalite transformation. The chemically stabilized cristobalite containing CaO and Al_2O_3 as dopants has cubic rather than tetragonal symmetry.

A critical particle size effect is believed to control the β to α transformation in the metastable β-cristobalite, by analogy with the onset of nucleation in zirconia (ZrO_2)[20] and in some other silicates.[21-23] In general a large particle size favors the spontaneous formation of low temperature phase on cooling, whereas a small particle size stabilizes the high temperature phase even at ambient temperatures. Thus, a critical particle size exists for a

given transformation, which depends on densification temperature and annealing time. In practice it is an important factor in controlling the transformation weakening behavior.

In this work it was proposed to synthesize the chemically stabilized cristobalite powder by a solution-polymerization technique developed in our laboratory.[24-27] Nitrate salts of cations are dissolved in aqueous solutions containing an organic stearic entrapping agent such as polyvinyl alcohol (-$[CH_2CHOH]_n$- or PVA). Subsequent polymerization and organic burnout yields a high purity, chemically homogeneous oxide powder without the use of expensive and unstable alkoxides. The extremely high specific surface area and sometimes nano size crystallites result in a highly reactive and readily sinterable, stoichiometric powder. The non-chelating PVA polymer consists of large chain molecules containing hydroxyl functional groups.[28] By using a molar ratio of cations to functional groups of approximately 4 : 1, homogeneous stearic entrapment of metal ions is achieved in these powders.

The aim of this study was to prepare a fine β-cristobalite powder of precisely doped composition by the PVA solution-polymerization route. It was desired to determine the critical grain size for the β to α phase transformation in cristobalite, by studying the effect of densification temperature during sintering or hot pressing, as well as annealing time. The transformation behavior would be evaluated by X-ray diffractometry (XRD) as well as scanning and transmission electron microscopy (SEM/TEM).

II. Experimental Procedure

1) Powder Preparation and Sintering Process

A clear sol was prepared from Ludox AS-40 colloidal silica (40 wt% suspension in water, Du Pont Chemicals, Wilmington, DE); $Al(NO_3)_3 \cdot 9H_2O$ (reagent grade, Aldrich Chemical Co., Milwaukee, WI) and $Ca(NO_3)_2 \cdot 4H_2O$ (reagent grade, Aldrich Chemical Co., Milwaukee, WI) in proportions to form a final composition of CaO : 2 Al_2O_3 : 80 SiO_2.[18,19] After dissolving these reagents in DI water, the organic carrier, PVA solution, was added and the mixture was heated. The PVA solution was prepared from 5 wt% PVA (degree of polymerization-1700, Air Products and Chemicals, Inc., Allentown, PA) dissolved in water. The proportions of the PVA to cation sources in the solution were adjusted in such a way that there were 4 times more positively charged valences from the cations than the negatively charged functional ends of the organics.[24] As the viscosity increased by evaporation of water, the mixture was vigorously stirred. The remaining water was then dried, converting the gel into a solid. Finally, the precursor was finely ground and calcined at 750 °C for 1h. The calcined powder was ball milled with zirconia media for

12 h. Iso-propyl alcohol was used as a solvent for milling. The ball-milled powder was uniaxially pressed at 20 MPa followed by iso-static pressing at 170 MPa for 10 min. The pellet-shaped green compacts were either pressureless sintered in an air atmosphere at 1350 °C for 1 h, or hot pressed at 1200 °C for 1 h under 28 MPa pressure in an Ar atmosphere. In both cases the furnace was cooled down to room temperature. After sintering, each sample was subjected to annealing at 1300 °C for various times. Some stress-induced transformation was achieved by grinding the annealed specimens on a #800 mesh SiC paper.

2) Characterization

(A) Thermal Analysis : The pyrolysis and decomposition behavior of crushed precursor were monitored by simultaneous differential scanning calorimetry and thermogravimetric analysis (DSC/TGA) (Model STA 409, Netzsch GmbH, Selb, Germany) up to 1200 °C at a heating rate of 10 °C/ min, in an air atmosphere.

(B) Particle Size Distribution Analyses : The particle size distribution of calcined or ball-milled powders were examined by X-ray absorption spectrometry (Sedigraph Model 5000E, Micromeritics). The powders were suspended in a calibrated dispersion liquid. The suspensions were ultrasonicated for 3 min before analysis.

(C) Specific Surface Area Measurement : The specific surface area between the calcined powder and ball-milled powder was compared by nitrogen gas absorption (Model ASAP 2400, Micromeritics, Norcross, GA).

(D) Average Grain Size Measurement : The average grain size of sintered cristobalite after annealing was analyzed according to the Jeffries-Saltykov method.

(E) X-ray Diffraction Analysis : The phase change between α and β-cristobalite was studied as a function of heating temperature and annealing time using a Rigaku spectrometer (DMax automated powder diffractometer, Rigaku/USA, Danvers, MA) with CuKα radiation (40 kV, 40 mA). The relative ratios of α and β-cristobalite phases were determined by integrating the X-ray peak areas of (102) of α-cristobalite and (222) of β-cristobalite by the equation:

$$V_\alpha = I(102)_\alpha / I(222)_\beta + I(102)_\alpha$$

in which, V_α was volume fraction of α-cristobalite, $I(102)_\alpha$ and $I(222)_\beta$ were peak intensity of $(102)_\alpha$ and $(222)_\beta$ respectively.

(F) Relative Density Measurement : The density for the sintered specimens was estimated by the Archimedes method using distilled water as a displacement liquid. The relative density of each specimen was calculated from density of the α and β-cristobalite (2.33 g/cm^3 and 2.26 g/cm^3, respectively) as a theoretical density at a given volume ratio.

(G) Thermal Expansion Behavior : The thermal expansion behavior of sintered polycrystalline cristobalite samples was determined with a recording dilatometer (Netzsch Dilatometer, 402E, Germany) up to 1100 °C at a heating rate of 5 °C/min.

(H) Electron Microscopy : The powder morphology and microstructure of sintered cristobalite were examined by scanning electron microscopy (SEM) (ISI DS-130, International Scientific Instruments, Santa Clara, CA). To observe grain size and cracking, polished and annealed samples were chemically etched in boiling phosphoric acid for 30 sec. The grain morphology and selected area diffraction patterns were examined by transmission electron microscopy (TEM) (Philips EM-420, Philips instruments, Inc., Mahwah, NJ). The TEM specimens were prepared by standard ceramic polishing, dimpling and ion-milling techniques.

III. Results

Fig. 1 shows the DSC and TGA results for a chemically stabilized cristobalite precursor. The thermal analysis revealed that the precursor underwent a three step weight loss process. The first weight loss was observed in the temperature range up to 170 °C, which may be associated with loss of water and NO_X compounds. A corresponding exotherm was observed in the DSC curve. The second major weight loss in TGA with a corresponding exotherm in the DSC curve occurred between 300 °C and 450 °C. The weight loss above 300 °C was due to the removal of the carbon formed during decomposition and pyrolysis process. After two exothermic peaks, the weight loss diminished gradually until 650 °C. There was no further weight loss after 700 °C. A small exothermic peak, which was associated with crystallization, was detected at around 1050 °C. The ball-milling process for producing a fine and homogeneous particle size was performed after calcination.[26] The calcination temperature of 750 °C was determined to lie between 600 °C, the highest temperature required for polymer burnout, and 1050 °C, the crystallization onset temperature. Fig. 2 displays the particle size distributions and SEM powder morphologies for the powders calcined at 750 °C for 1 h or ball milled for 12 h after calcination. The calcined powder had a wide particle size distribution in the range from 80 μm to 5 μm and were of soft and irregular shape with sharp corners and edges. However, the ball-milled powder had a quite narrow particle size distribution with porous agglomerates and small particles of approximately 0.1-0.4 μm in size. The calcined powder had a BET specific surface area of 25 m^2/g. The high specific surface area from the large particle size meant that the calcined powder was very porous. The ball-milled powder had a specific surface area of 80 m^2/g.

Room temperature XRD spectra following the development of crystalline phases of the calcined powders at various heating temperatures are shown in Fig. 3. An amorphous phase was observed at 1000 °C. Above 1100 °C, the β-cristobalite crystalline phase was detected and β-cristobalite peaks were developed almost completely at 1200 °C. With increasing temperature the amount of α-cristobalite phase increased gradually, while the amount of β-cristobalite decreased. At 1450 °C, β-cristobalite still remained as a minor phase in the α-cristobalite matrix. Dilatometry curves for the stabilized cristobalite are shown in Fig. 4. The α ⇔ β transformation occurred at 180 °C on heating and at 170 °C on cooling. The transformation temperature was lower than that of pure cristobalite because of the dopant effect.[13] As the graphs show, the thermal expansion coefficient of β-cristobalite was approximately 1.5×10^{-6}/°C and tended to decrease on heating. A change in thermal expansion coefficient was observed at the α ⇔ β transformation temperature. This change was much less for the polycrystalline cristobalite sintered at 1350 °C than the one at 1450 °C. The difference in the change of thermal expansion coefficient was attributed to the α-cristobalite content. In the case of the polycrystalline cristobalite sintered at 1350 °C, α-cristobalite was present in the β-cristobalite matrix whereas, for the polycrystalline cristobalite sintered at 1450 °C, the α-cristobalite was the matrix phase (Fig. 3).

The formation of α-cristobalite on cooling was affected by varying the grain size. Spontaneous transformation from β phase to α phase occurred at larger grain sizes. In contrast, a small β-cristobalite grain size stabilized the β phase. The grain size of the stabilized β-cristobalite was controlled by annealing time. Fig. 5 shows the plot of integrated X-ray peak intensity ratios of $I(102)_\alpha / I(222)_\beta + I(102)_\alpha$ and average grain sizes for hot-pressed or pressureless-sintered samples as a function of annealing time. It was impossible to compare the intensity of the (111) and (220) peaks from β-cristobalite with the (101) and (200) peaks from α-cristobalite, which are the high intensity peaks of the cristobalite system, because the peaks were located at the almost the same 2θ value. Therefore, the relative amount of α and β-cristobalite phase was compared from the relative intensity of $(102)_\alpha$ and $(222)_\beta$ peaks.

In general, ratios of α/β-cristobalite phases and the average grain size showed an increase with increasing annealing time. The ratio of α/β XRD peak intensity and average grain size for the pressureless-sintered sample, which had a sintered density of 2.15 g/cm^3 (94% relative density) at 0 annealing time, increased very gradually for annealing times over 30 h. The average grain sizes and the ratios of α/β XRD peak intensity at 30 h and 50 h anealing times were about 5 μm, 60 vol%, and 5.6 μm, 63 vol %, respectively. In the case of the hot-pressed sample, which had a sintered density of 2.24 g/cm^3 (98% relative

density) at 0 annealing time, grain growth occurred at a faster rate than the pressureless-sintered sample during the first 12 h of annealing time. The rate of grain growth decreased gradually from 12 h annealing time onwards. In contrast to the pressureless-sintered sample, the ratio of α/β XRD peak intensity and grain growth increased till the annealing time of 50 h. Large grain sizes of about 8.5 μm at an annealing time of 50 h resulted in fragile samples having extensive cracks. This was because the thermally-induced transformation occurred spontaneously primarily due to the critical size effect. The sample annealed for 50 h showed almost 80 vol% α-cristobalite. Fig. 6 is an SEM micrograph of a shattered cristobalite sample which was hot-pressed and annealed for 50 h. Thick and extensive cracks rather than fine microcracks were observed.

The polished surface micrographs of cristobalite annealed at various times are shown in Figs. 7, and 8. The microstructure of the pressureless-sintered sample annealed for 12 h (Fig. 7(b)) was not dense, with an average particle size of 3 μm. Longer annealing times (30 h) increased the average grain size to about 5 μm. However, the grain growth occurred inhomogeneously. Some small grains coexisted with large grains of over 5 μm size even after long annealing times of 30 h. The coarse microstructure having numerous micropores showed a very gradual increase in the ratio of α/β XRD peak intensity. This was because the large grains increased in size with increasing annealing time, while the small-size grains, in contrast, did not grow despite long annealing times. About 40 vol% β-cristobalite was found in the matrix after annealing for 30 h (Fig. 5(a)). As seen in Fig. 7(c) some cracking was induced by the thermally-induced transformation which occurred spontaneously in the large-grain sized sample.

The hot-pressed and un-annealed sample had a smaller grain size and denser microstructure than did the pressureless-sintered sample. Hence, the grain growth occurred at a faster rate and was more homogeneous than in the pressureless-sintered sample. It is attributed to easier mass transportation through the dense microstructure during the annealing process. This resulted in an increase in the ratio of α/β XRD peak intensity up to a 50 h annealing time, in contrast to the pressureless-sintered sample (Fig. 5(b)). Some cracks were detected in the microstructure having an average grain size of 5 μm, at annealing times of 12 h. The hot-pressed cristobalite annealed for 30 h consisted of about 72 % α-cristobalite as shown in Fig. 5(b). It also exhibited cracks in the microstructure having an average grain size of 7 μm.

The transformation of β to α cristobalite was susceptible to the influence of stress. Shear stress-induced β→α-cristobalite conversion for annealed and ground specimens are compared with the un-ground specimens at various annealing times. Fig. 9 displays the result. The amount of stress-induced α phase increased with increasing annealing time. In

case of pressureless-sintered cristobalite, the ratio of α/β XRD peak intensity for ground specimens was slightly higher than for un-ground specimens. About 7 vol% α-cristobalite was increased by the stress-induced transformation after annealing for 20 h. In comparison, the hot-pressed specimens were more sensitive to shear stress. An increase of about 13 vol% α-cristobalite was calculated after 12 h of annealing time. In contrast to pressureless-sintered specimens, the increase in the amount of α-cristobalite in the ground specimens over that in the only annealed specimens, decreased with increasing annealing time above 12 h. This may be attributed to the fact that the amount of β-cristobalite, which can be transformed by stress, was decreased by the thermally-induced transformation which occurred in the over-sized grains.

Transmission electron microscopy studies examined the critical size effect on the phase transformation of cristobalite. Fig. 10 (a) and (b) are TEM bright-field micrographs of α and β-cristobalite grains and corresponding SAD patterns for the hot-pressed and annealed samples. A cubic β-cristobalite pattern was found in the un-annealed specimen.[29] The specimen annealed for 12 h showed a tetragonal α-cristobalite pattern in the grain which had a size of 5 μm and above.

IV. Discussion

For extensive phase transformation it is necessary to have uniform grain growth for a homogeneous microstructure. Therefore, a starting powder should have a small particle size and have a narrow particle size distribution. The solution-polymerization route employing PVA solution was quite effective in achieving a fine powder for chemically stabilized cristobalite. The soft and porous powder obtained after calcination at 750 °C made it easier to get a fine powder on further ball-milling of the powder. The powder calcined above 900 °C started becoming harder and denser. This was because the powder after polymer burnout was active enough to be densified at that temperature. If during the calcination process, powder densification was initiated, then the powder could not be ball milled to a fine particle size. The particle size distribution was also quite narrow in this method. However, in the case of the pressureless-sintered specimen, uniform grain growth did not occur because of the presence of pores between grains. The non-uniform grain growth resulted in only localized phase transformation. This fact was demonstrated in Fig. 5(a) and Fig. 7(c) where about 40 vol% pressureless-sintered β-cristobalite was retained even after 30 h of annealing. This was because the smaller grains were not affected by thermally-induced transformation. X-ray analysis of the calcined powder heated at 1450 °C (Fig. 3) still showed β phase, despite the high enough temperatures

needed to cause thermally-induced transformation. This is also attributed to the presence of particles which were too small to be transformed. Hot-pressing was very effective in controlling the porosity and a relatively uniform grain growth was possible during the annealing process.

Internal cracks were formed due to thermally-induced transformation, which spontaneously occurred on cooling, and were developed from an average grain size of 5 μm. Shear stress-induced transformation during grinding also depended upon the grain size. However, the pressureless-sintered cristobalite displayed less dependence on the grain size because of non-uniform grain growth resulting in a coarse microstructure. In order to use the chemically stabilized β-cristobalite as a transformation weakening mechanism, more extensive shear stress-induced transformation is desirable. For that, a homogeneous microstructure having an average grain size of 4-5 μm is required. The critical size of 4 μm is a little smaller than the grain size of 5 μm at which cracks due to thermally-induced transformation occurred spontaneously.

V. Conclusions

The solution-polymerization method employing PVA solution as a polymeric carrier was a suitable process for synthesizing chemically stabilized β-cristobalite. The amorphous-type cristobalite powder, which was very fine and had a relatively narrow particle size, was fabricated by ball-milling the soft and porous calcined powder.

The α/β-cristobalite ratio and average grain size of annealed β-cristobalite increased with increasing annealing time. The pressureless-sintered polycrystalline cristobalite experienced non-uniform grain growth during the annealing process. This resulted in inhomogeneous microstructure and localized phase transformation. The hot-pressed cristobalite had a denser microstructure and more extensive phase transformation than did the pressureless-sintered cristobalite. The intra-granular cracks were produced by thermally-induced transformation at a grain size of 5 μm and above.

It was more easy to shear stress induce the β→α-cristobalite conversion in the hot-pressed specimens than in the pressureless-sintered specimens. About 13 vol% stress-induced α-cristobalite was obtained on grinding the cristobalite, which had been hot-pressed followed by annealing for 12 h. A critical grain size of 4-5 μm can be considered to be suitable for phase transformation weakening behavior of chemically stabilized β-cristobalite.

Acknowledgment: This work was supported by the US Air Force Office of Scientific Research, through Dr. Alexander Pechenik, under grant number AFOSR-F49620-93-1-0227.

References

[1]A. G. Evans, "Perspectives on the Development of High Toughness Ceramics," *J. Am. Ceram. Soc.*, **73** [2] 187-206 (1990).

[2]R. J. Kerans, R. S. Hay, N. J. Pagano, and T. A. Parthasarathy, "The Role of the Fiber-Matrix Interface in Ceramic Composites," *Am. Ceram. Soc. Bull.*, **68** [2] 429-42 (1989).

[3]W. J. Clegg, K. Kendall, N. M. Alford, D. Birchall, and T. W. Button, "A Simple Way to Make Tough Ceramics," *Nature*, **347**, 455-57 (1990).

[4]W. J. Clegg, "The Fabrication and Failure of Laminar Ceramic Composites," *Acta Metall.*, **40** [11] 3085-93 (1992).

[5]P. E. D. Morgan and D. B. Marshall, "Ceramic Composites of Monazite and Alumina," *J. Am. Ceram. Soc.*, **78** [6] 1553-63 (1995).

[6]D. H. Kuo, W. M. Kriven, and T. J. Mackin, "Control of Interfacial Properties through Fiber Coating Monazite Coatings in Oxide/Oxide Composites," *J. Am. Ceram, Soc.*, (1997), in press.

[7]D. H. Kuo and W. M. Kriven, "Fracture of Multilayer Oxide Composites," *J. Mater. Sci. and Eng.*, (1997), in press.

[8]W. M. Kriven, "Possible Alternative Transformation Toughened to Zirconia: Crystallographic Aspects," *J. Am. Ceram. Soc.*, **71** [12] 1022-30 (1988).

[9]W. M. Kriven, "Displacive Phase Transformation and Their Applications in Structural Ceramics," *J. de Physique IV, Colloque* **C8**, 101-110 (1995).

[10]W. M. Kriven and S. J. Lee, "Toughening of Ceramic Composites by Transformation Weakening of Interphases (Part II. Mullite/Cordierite Laminate with β-cristobalite Interphase)," *J. Am. Ceram. Soc.*, submitted.

[11]A. F. Wright and A. J. Leadbetter, "The Structures of the β-cristobalite Phase of SiO_2 and $AlPO_4$," *Philos. Mag.*, **31**, 1391-401 (1975).

[12]D. A. Peacor, "High-Temperature Single-Crystal Study of the Cristobalite Inversion," *Z. Kristallogr.*, **138**, 274-98 (1973).

[13]V. G. Hill and R. Roy, "Silica Structure Studies: V, The Variable Inversion in Cristobalite," *J. Am. Ceram. Soc.*, **41** [12] 532-37 (1958).

[14]C. N Fenner, "Stability Relations of the Silica Minerals," *Am. J. Sci. [4th Series]*, **36** [214] 331-84 (1913).

[15]W. Eitel, "Structural Anomalies in Tridymite and Cristobalite," *Am. Ceram. Soc. Bull.*, **36** [4] 142-48 (1957).

[16]M. J. Buerger, "Stuffed Derivatives of the Silica Structures," *Am. Mineral.*, **39** [7-8] 600-14 (1954).

[17]A. J. Perrotta, D. K. Grubbs, E. S. Martin, and N. R. Dando, "Chemical Stabilization of β-cristobalite." *J. Am. Ceram. Soc.*, **72** [3] 441-47 (1989).

[18]E. S. Thomas, J. G. Thompson, R. L. Withers, M. Sterns, Y. Xiao, and R. J. Kirkpatrick, "Further Investigation of the Stabilization of β-cristobalite." *J. Am. Ceram. Soc.*, **77** [1] 49-56 (1994).

[19]J. B. Parise, D. J. Weidner, J. D. Jorgensen, and M. A. Saltzberg, "Pressure-Induced Phase Transition and Pressure Dependence of Crystal Structure in Low (α) and Ca/Al-Doped Cristobalite." *J. Appl. Phys.*, **75** [3] 1361-66 (1994).

[20]A. H. Heuer, N. Claussen, W. M. Kriven, and M. Rühle, "Stability of Tetragonal ZrO_2 Particles in Ceramic Matrices," *J. Am. Ceram. Soc.*, **65** [12] 642-50 (1982).

[21]W. M. Kriven, C. J. Chan, and E. A. Barinek, "The Particle-Size Effect of Dicalcium Silicate in a Calcium Zirconate Matrix"; pp. 145-55 in Advances in Ceramics, Vol. 24, *Science and Technology of Zirconia III*. Edited by S. Somiya, N. Yamamoto, and H. Yanagida. American Ceramic Society, Westerville, OH, 1988.

[22]C. J. Chan, W. M. Kriven, and J. F. Young, "Physical Stabilization of the $\beta \rightarrow \gamma$ Transformation in Dicalcium Silicate." *J. Am. Ceram. Soc.*, **75** [6] 1621-27 (1992).

[23]C. M. Huang, D. H. Kuo, Y. J. Kim, and W. M. Kriven, "Phase Stability of Chemically Derived Enstatite ($MgSiO_3$) Powders." *J. Am. Ceram. Soc.*, **77** [10] 2625-31 (1994).

[24]M. A. Gulgun and W. M. Kriven, "A Simple Solution-Polymerization Route for Oxide Powder Synthesis"; pp. 57-66 in Ceramic Transactions, Vol. 62, *Science, Technology, and Commercialization of Powder Synthesis and Shape Forming Processes*. Edited by J.J Kingsley, C.H. Schilling, and J.H. Adair. American Ceramic Society, Westerville, OH, 1996.

[25]M. A. Gulgun, M. H. Nguyen, and W. M. Kriven, "Polymeric Organic-Inorganic Synthesis of Mixed Oxides," *J. Am. Ceram. Soc.*, (1996), submitted.

[26]S. J. Lee and W. M. Kriven, "Nano-size Amorphous Cordierite Powder Prepared by a Solution-Polymerization Route," *J. Am. Ceram. Soc.*, (1997), submitted.

[27]M. H. Nguyen and W. M. Kriven, "Chemical Synthesis of Dysprosium Titanate via Stearic Entrapment," *J. Am. Ceram. Soc.*, (1997), to be published.

[28]K. Toyoshima, "General Properties of Polyvinyl Alcohol in Relation to its Applications"; pp. 22-42 in *Polyvinyl Alcohol Properties and Applications*. Edited by C. A. Finch. John Wiley &Sons, New York, 1973.

[29]R. L. Withers, J. G. Thompson, and T. R. Welberry, "The Structure and Microstructure of α-cristobalite and Its Relationship to β-cristobalite," *Phys. Chem. Minerals*, **16**, 517-523 (1989).

Figure captions

Figure 1. Simultaneous DSC/TGA analysis of the chemically stabilized β-cristobalite precusor containing PVA solution as a organic carrier.

Figure 2. Particle size distribution of the amorphous-type cristobalite powders and SEM micrographs of the powders (a) calcined at 750 °C for 1 h and (b) ball milled for 12 h after calcination.

Figure 3. X-ray diffraction spectra of calcined powders heated at various temperatures with a holding time of 1 h.

Figure 4. Dilatometry curves for chemically stabilized cristobalite samples sintered at (a) 1350 °C for 1 h and (b) 1450 °C for 1 h.

Figure 5. Integrated X-ray peak intensity ratios of α(102) / [β(222) + α(102)] and average grain sizes of (a) sample pressureless sintered at 1350 °C for 1 h and (b) sample hot pressed at 1200 °C for 1 h under 28 MPa as a function of annealing time.

Figure 6. SEM photograph of shattered cristobalite sample hot-pressed at 1200 °C and annealed at 1300 °C for 50 h.

Figure 7. SEM micrographs of the polished and etched surfaces of cristobalite pressureless sintered at 1350 °C for 1 h according to different annealing times of (a) 0 h (b) 12 h and (c) 30 h (arrows indicate intra-granular cracks).

Figure 8. SEM micrographs of the polished and etched surfaces of cristobalite hot pressed at 1200 °C for 1 h under 28 MPa according to different annealing times of (a) 0 h (b) 12 h and (c) 30 h (arrows indicate intra-granular cracks).

Figure 9. Grinding effect on the ratio of α/β XRD peak intensity of (a) pressureless-sintered cristobalite and (b) hot-pressed cristobalite at various annealing times.

Figure 10. Bright-field TEM micrographs and corresponding SAD patterns of the hot-pressed specimens of (a) [111] zone axis diffraction pattern from un-annealed β-cristobalite and (b) [022] zone axis diffraction pattern from transformation-induced α-cristobalite after annealing for 12 h.

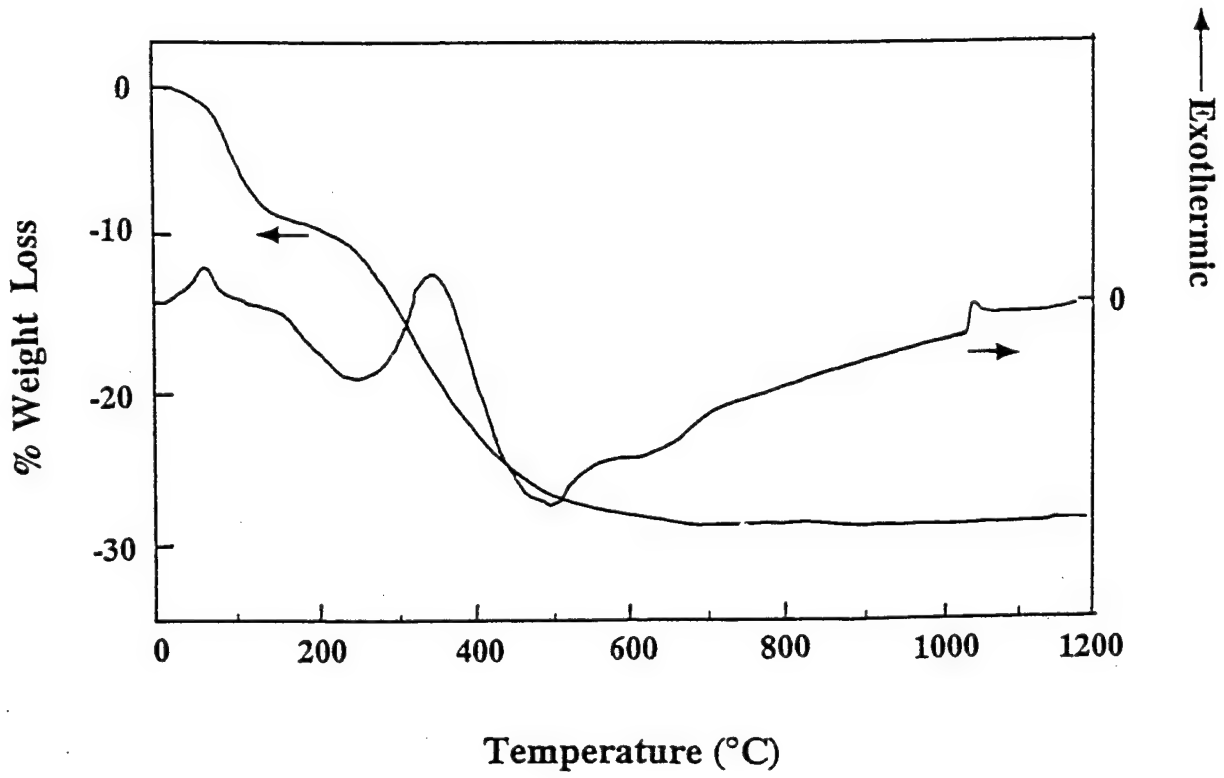
0
-10
-20
-30
% Weight Loss
0
200
400
600
800
1000
1200
Temperature (°C)
0
Exothermic

Figure 1

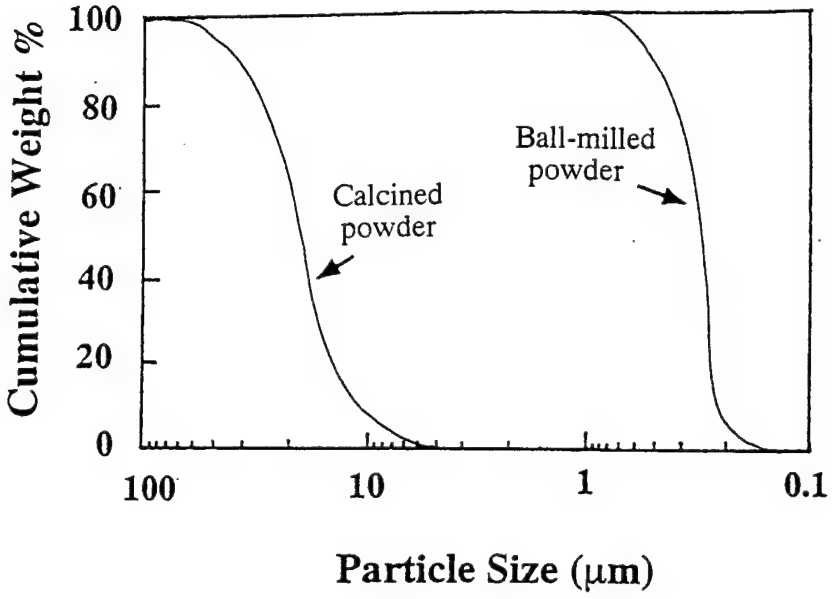
Cumulative Weight %
100
80
60
40
20
0
100
10
1
0.1
Calcined powder
Ball-milled powder
Particle Size (μm)

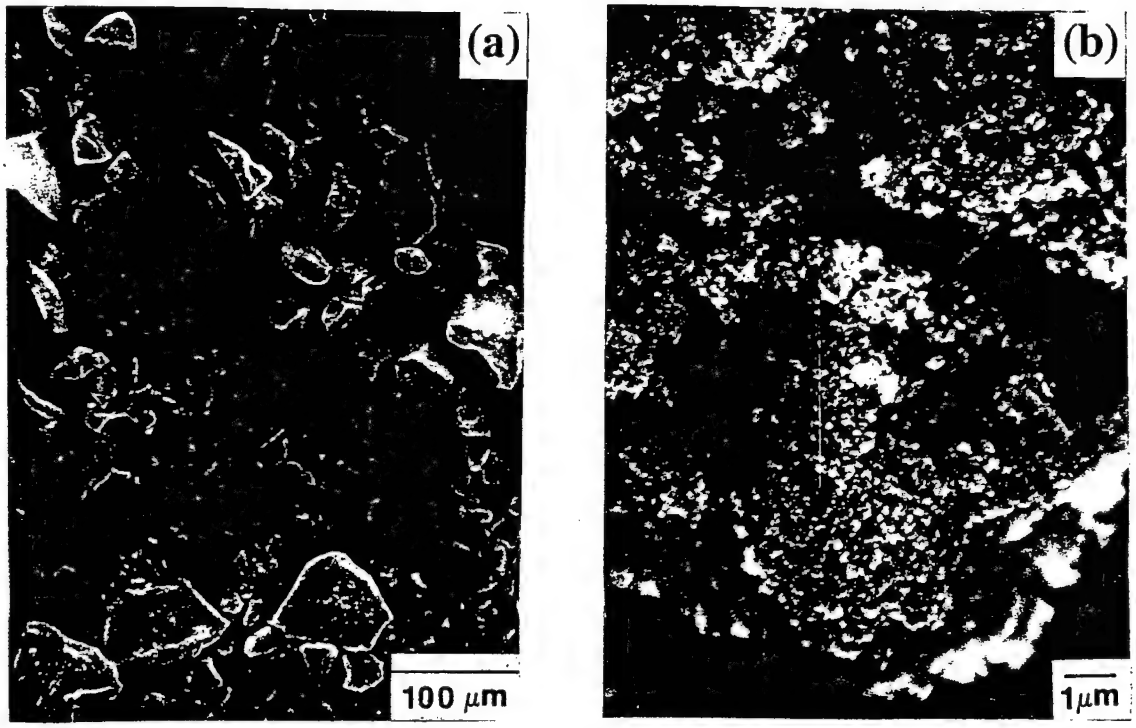
(a)
100 μm
(b)
1μm

Figure 2

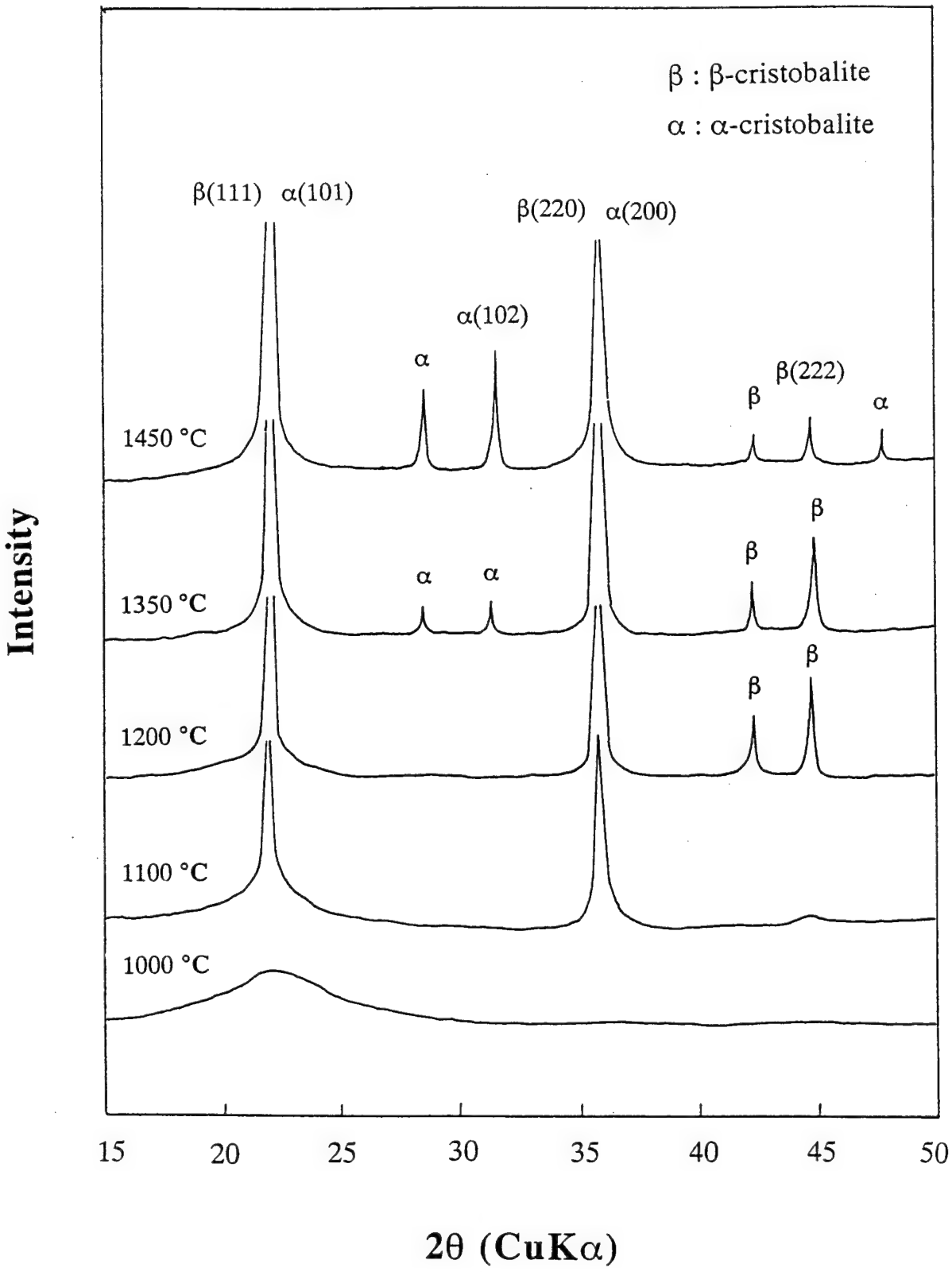
β : β-cristobalite
α : α-cristobalite
β(111)
α(101)
β(220)
α(200)
α(102)
α
β(222)
β
α
1450 °C
1350 °C
1200 °C
1100 °C
1000 °C
Intensity
15
20
25
30
35
40
45
50
2θ (CuKα)

Figure 3

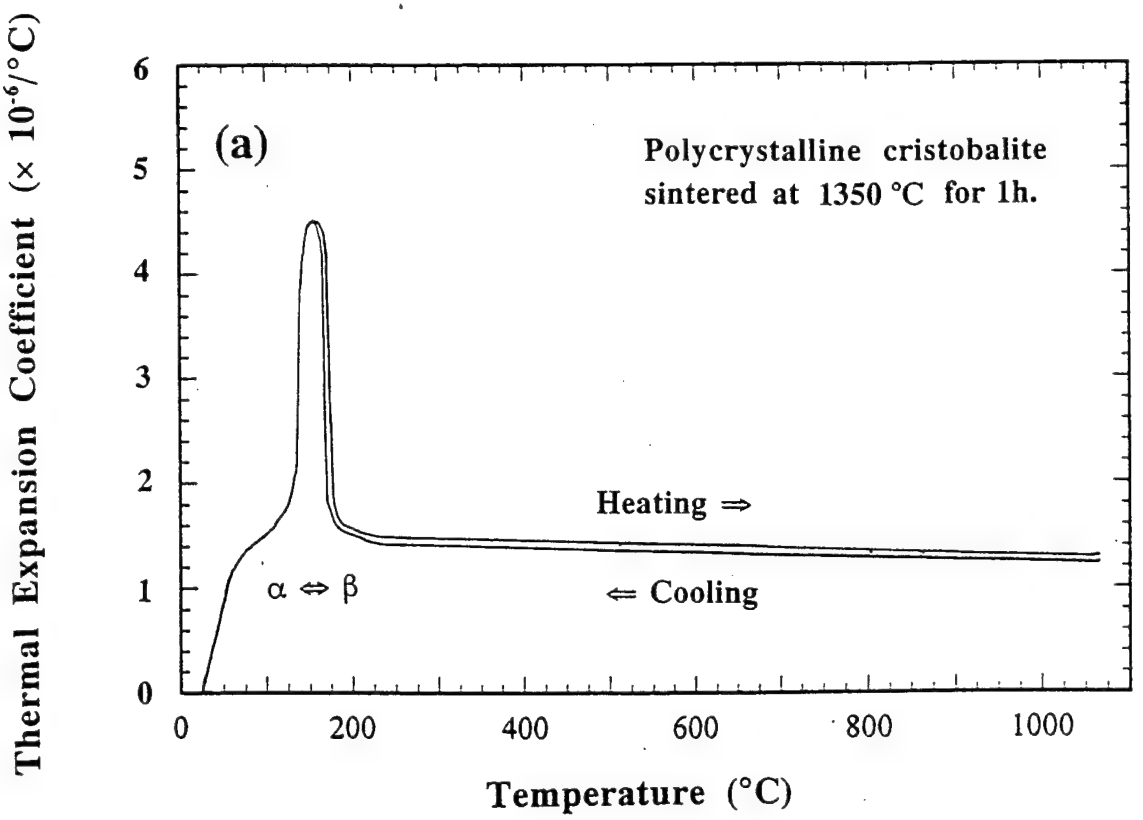
(a)
Polycrystalline cristobalite
sintered at 1350 °C for 1h.
Heating ⇒
⇐ Cooling
α ⇔ β
Thermal Expansion Coefficient (× 10⁻⁶/°C)
Temperature (°C)
0
1
2
3
4
5
6
0
200
400
600
800
1000

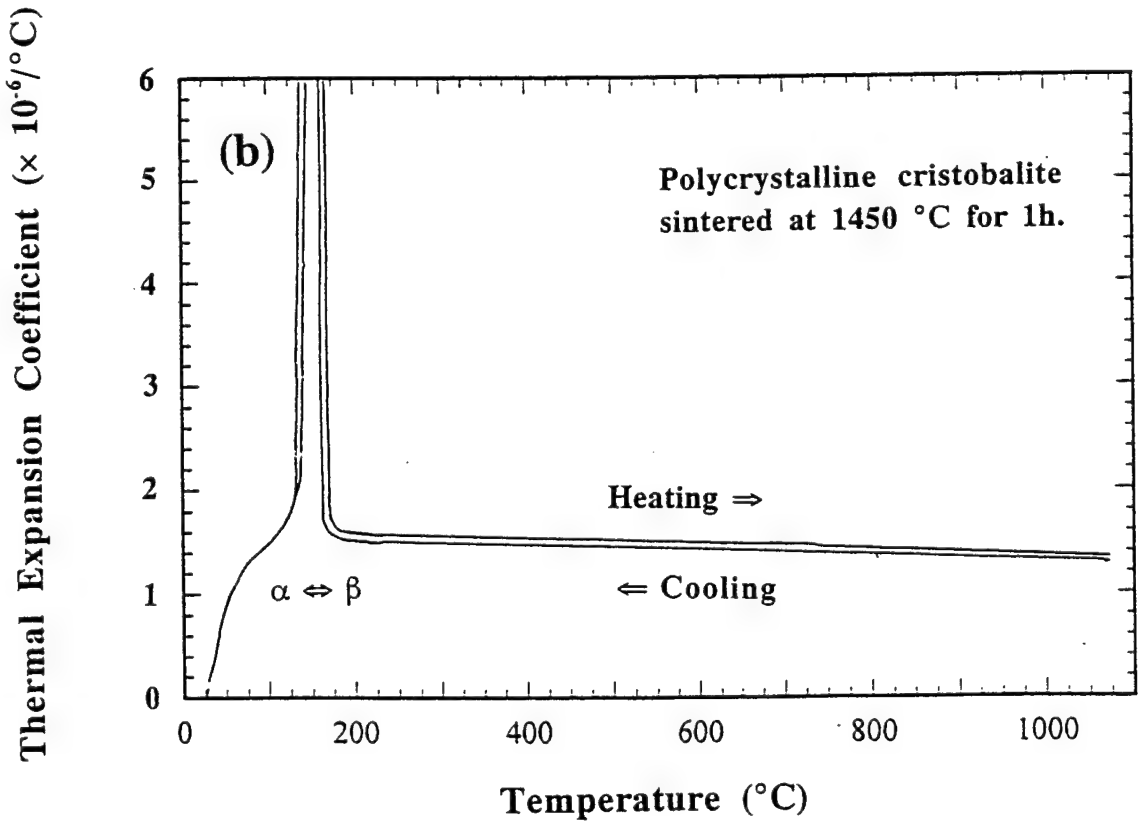
(b)
Polycrystalline cristobalite
sintered at 1450 °C for 1h.
Heating ⇒
⇐ Cooling
α ⇔ β
Thermal Expansion Coefficient (× 10⁻⁶/°C)
Temperature (°C)
0
1
2
3
4
5
6
0
200
400
600
800
1000

Figure 4

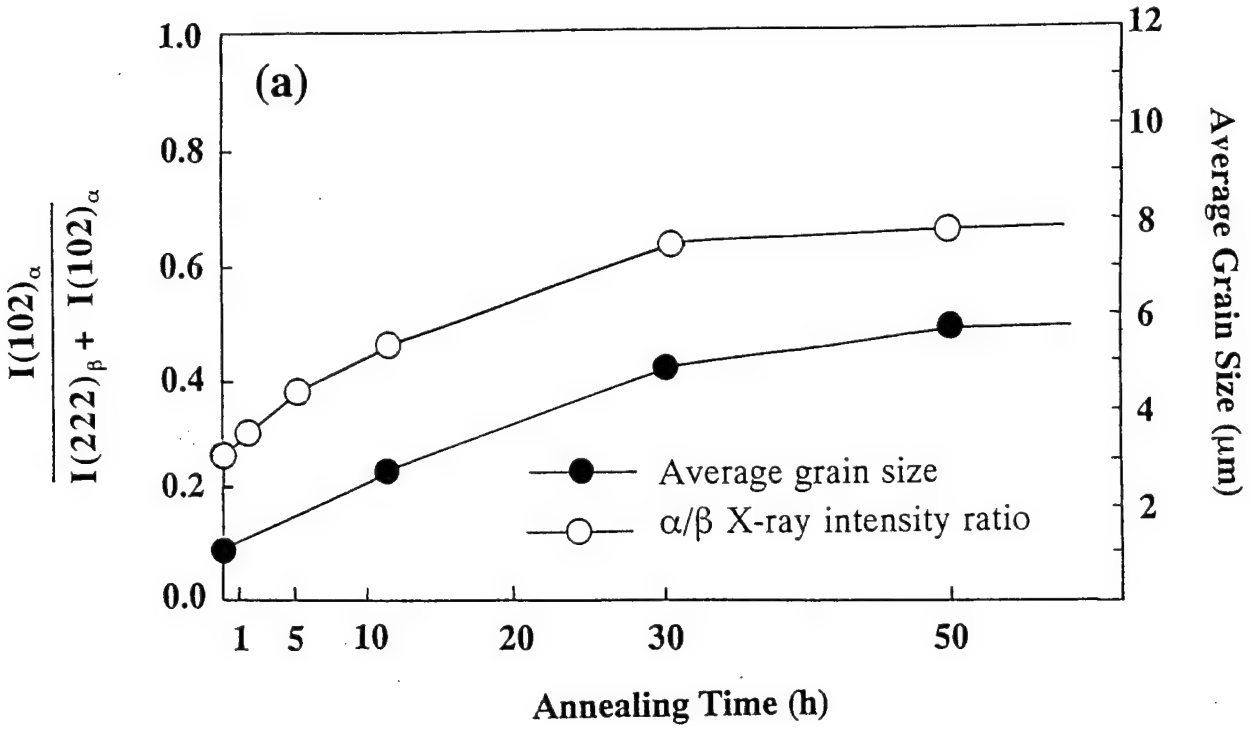
(a)
1.0
0.8
0.6
0.4
0.2
0.0
12
10
8
6
4
2
1 5 10 20 30 50
Annealing Time (h)
Average Grain Size (μm)
I(102)α / I(222)β + I(102)α
Average grain size
α/β X-ray intensity ratio

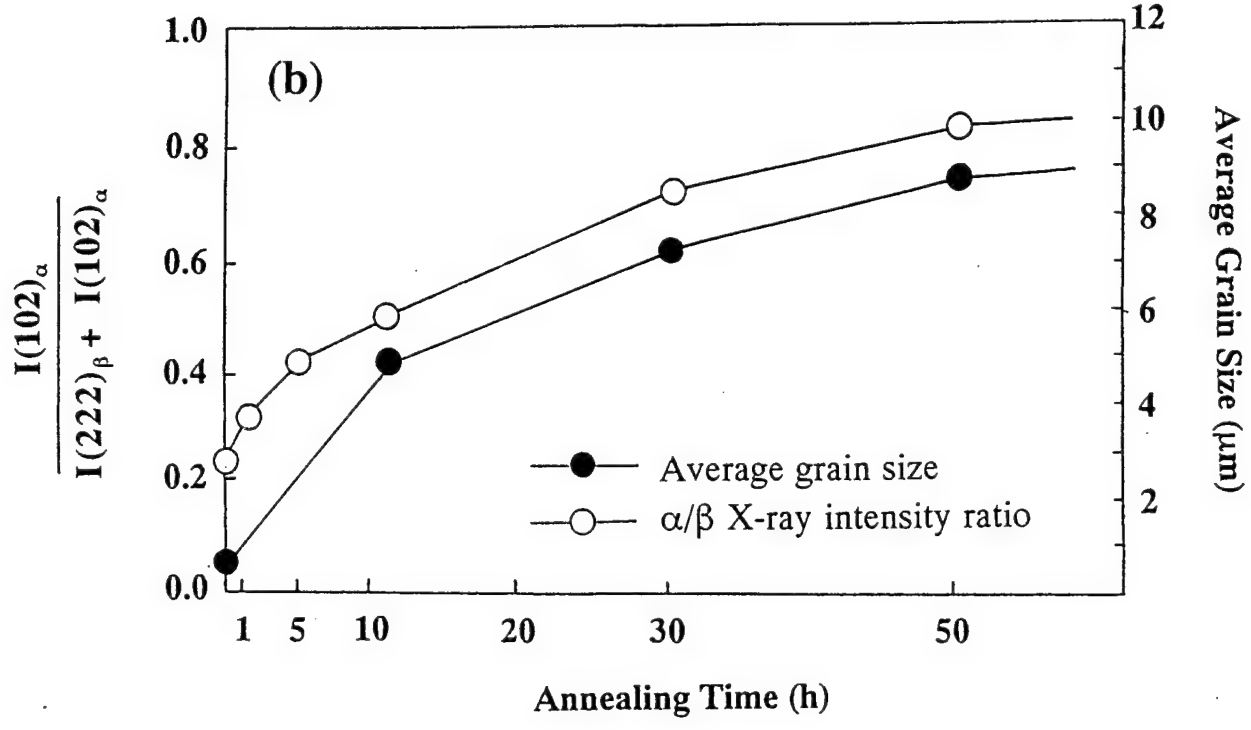
(b)
1.0
0.8
0.6
0.4
0.2
0.0
12
10
8
6
4
2
1 5 10 20 30 50
Annealing Time (h)
Average Grain Size (μm)
I(102)α / I(222)β + I(102)α
Average grain size
α/β X-ray intensity ratio

Figure 5

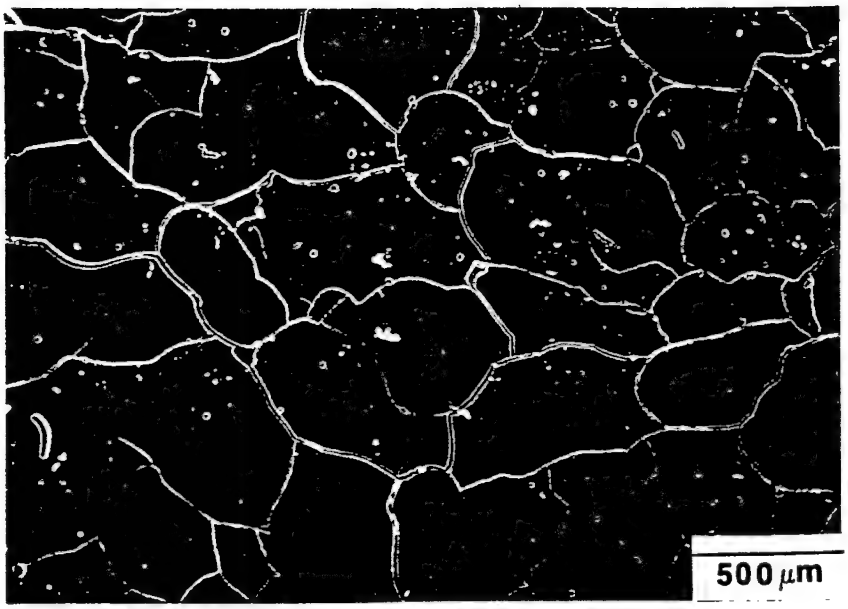

Figure 6

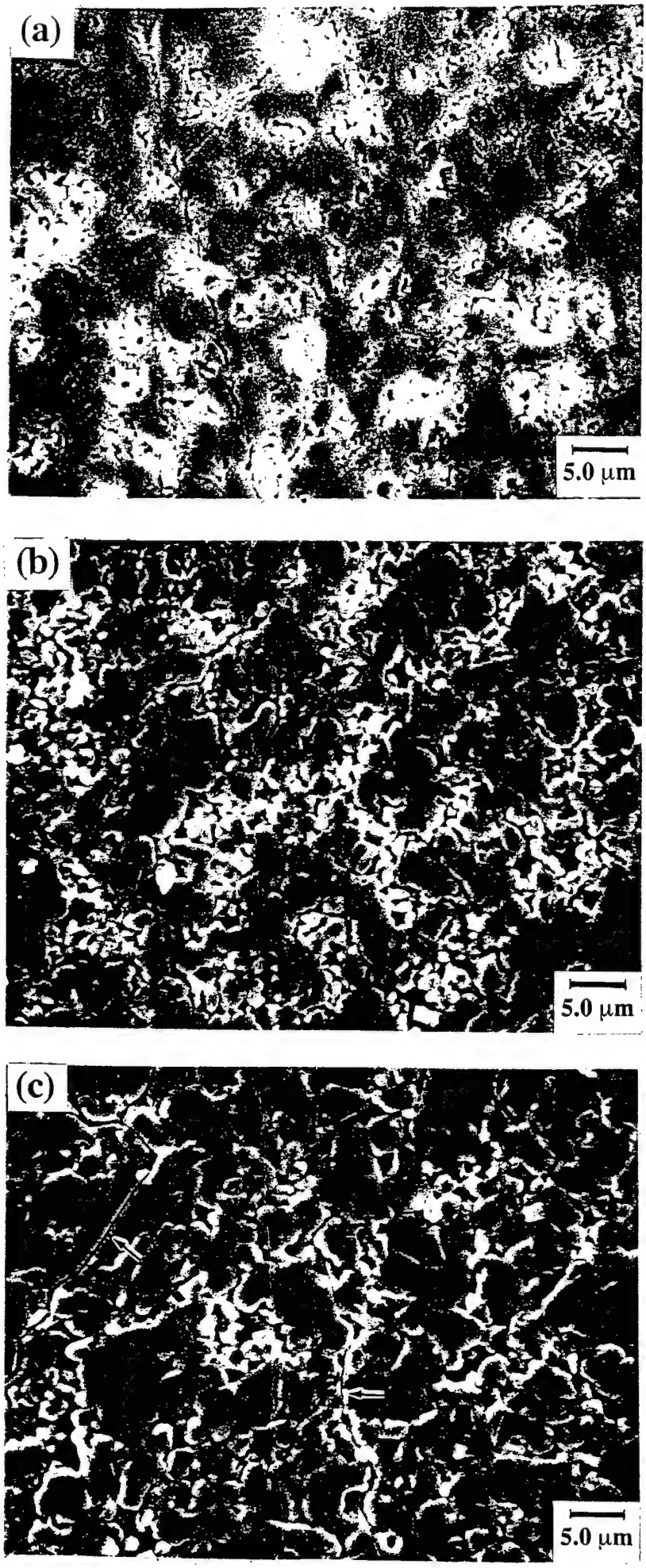

Figure 7

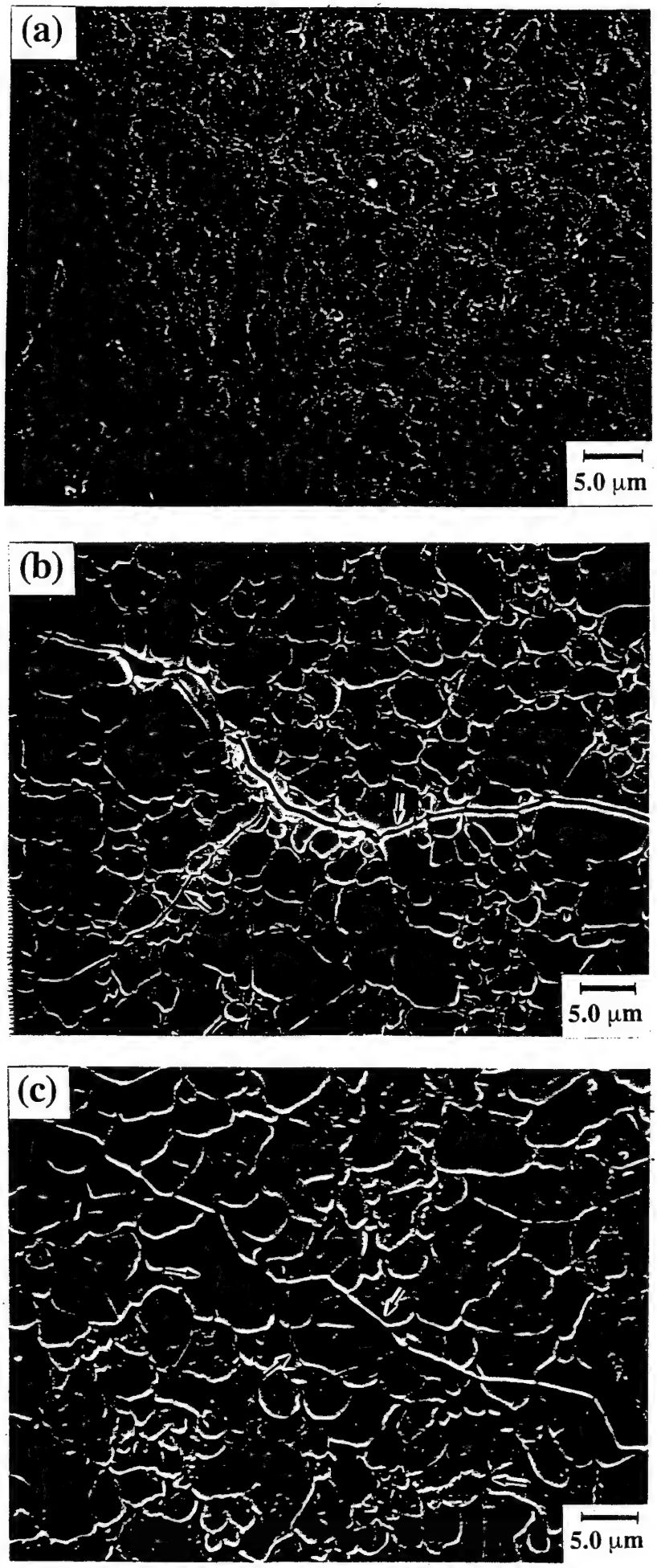

Figure 8

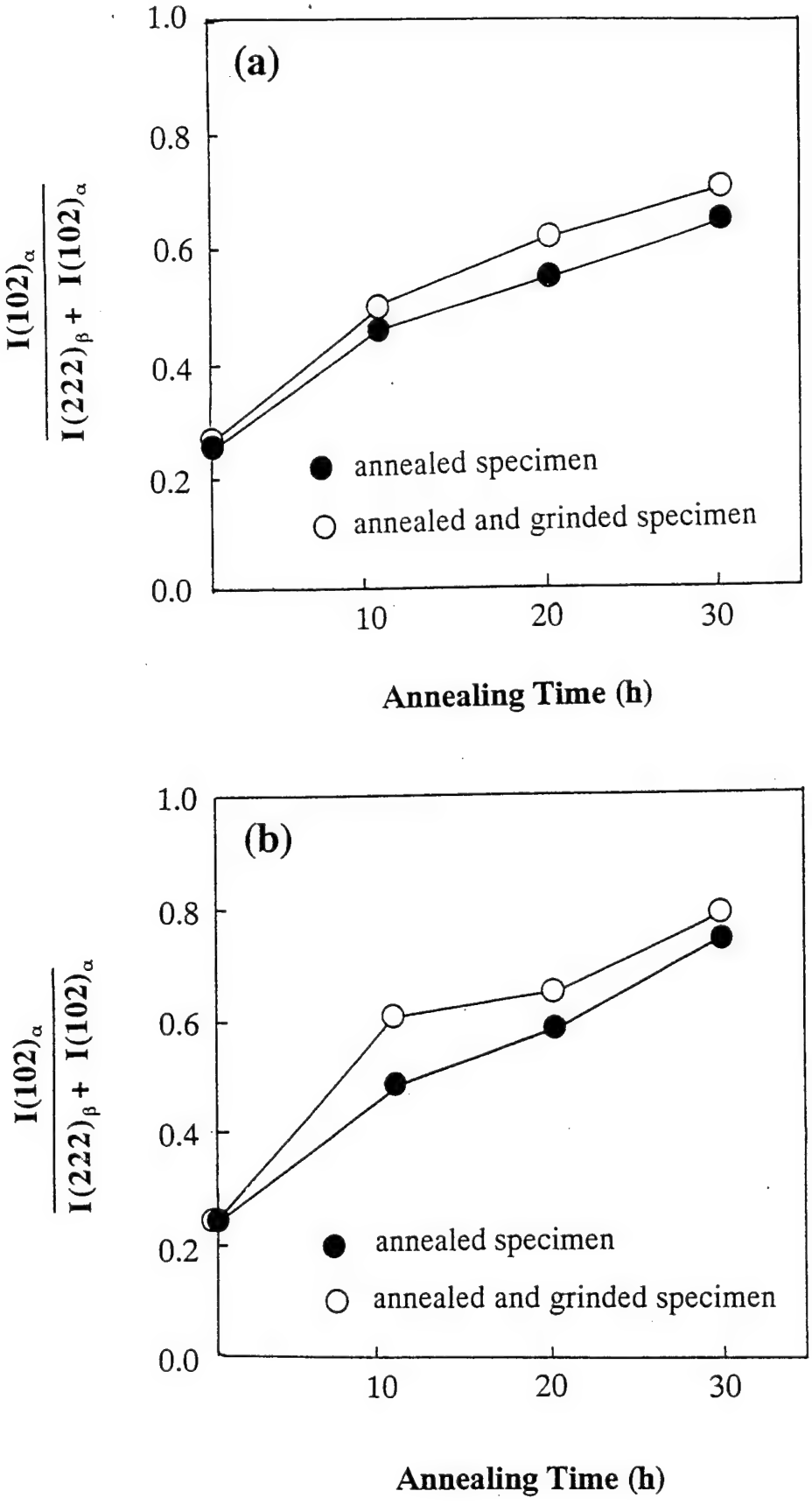
(a)
1.0
0.8
0.6
0.4
0.2
0.0
10
20
30
annealed specimen
annealed and grinded specimen
$\frac{I(102)_\alpha}{I(222)_\beta + I(102)_\alpha}$
Annealing Time (h)
(b)
1.0
0.8
0.6
0.4
0.2
0.0
10
20
30
annealed specimen
annealed and grinded specimen
$\frac{I(102)_\alpha}{I(222)_\beta + I(102)_\alpha}$
Annealing Time (h)

Figure 9

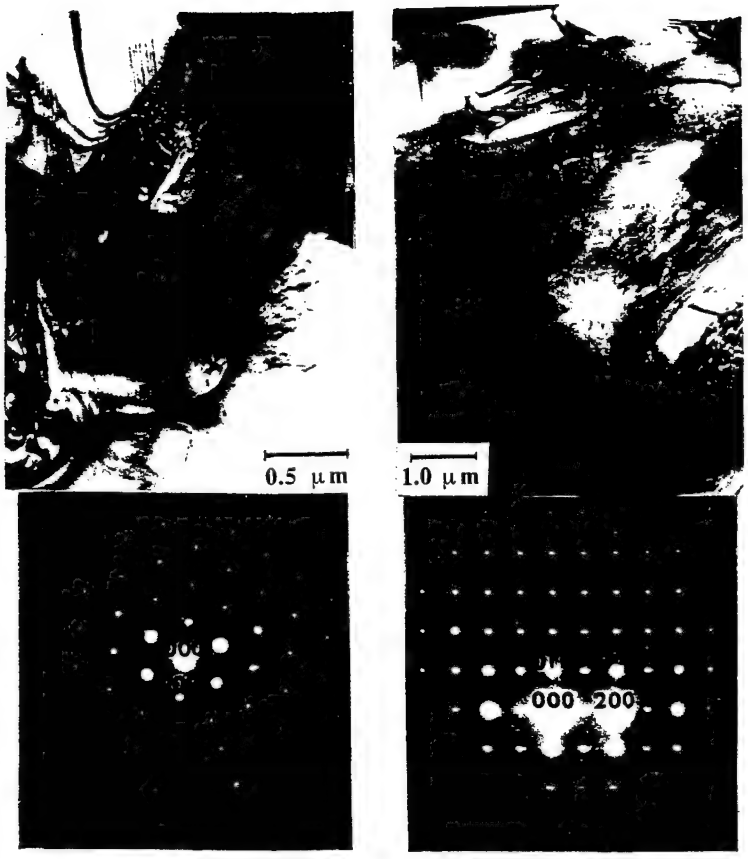

(a) (b)

Figure 10

Toughening of Ceramic Composites by Transformation Weakening of Interphases (Part II. Mullite/Cordierite Laminate with β-cristobalite Interphase)

Waltraud M. Kriven* and Sang-Jin Lee*

Department of Materials Science and Engineering, University of Illinois at Urbana-Champaign, Urbana, Illinois 61801, USA

Abstract

A new concept for achieving graceful failure in oxide composites is introduced. It is based on debonding of a weak interphase between a matrix and reinforcement (e.g. fiber), or in a laminated composite. The interphase can be thermally or shear stress induced by transformation weakening, which results from an accompanying significant volume contraction and/or unit cell shape change, on cooling from a high temperature to low temperature crystal structure.

Mullite/cordierite laminates with a β→α-cristobalite transformation weakened interphase were investigated in order to demonstrate interphase debonding behavior. The laminates were fabricated by stacking alternate tape-cast green sheets of chemically stabilized β-cristobalite and a mullite/cordierite matrix mixture. The laminate showed fracture behavior dependent on a critical size effect. The grain size of polycrystalline β-cristobalite was controlled by annealing time at 1300 °C. With increasing annealing time, the strength decreased due to the formation of internal microcracks in the cristobalite layer which occurred spontaneously during thermally-induced transformation. The hot-pressed laminate, annealed for 10 h at 1300 °C, had an average grain size of 4.2 μm and a strength of 131 MPa. Its work of fracture was 2.38 kJ/m^2 with a non-catastrophic fracture behavior. The indentation response indicated crack deflection along the cristobalite debonding interphase.

* Members, The American Ceramic Society.

I. Introduction

The brittleness and unreliability of ceramics in oxidizing environments remain difficult and unsolved problems. Attempts to impart "graceful failure" analogous to ductility in metals have been partially successful with the use of composites. These are ceramic matrices reinforced with fibers, particulates, platelets or whisker-shaped second phases.[1] It is now well established that toughening results from debonding at the interface between matrix and reinforcement phase[2-7] This is a crucial step leading to crack energy dissipation such as frictional sliding at the interface, while transferring load bearing forces on to fibers,[7-13] or causing crack deflection mechanisms to operate in laminates.[14-19]

For long term retention of high temperature properties in oxidizing environments, chemically stable oxide fibers, coatings and matrices are highly desirable components in ceramic composites. At present single crystal saphire (Al_2O_3) and yttrium aluminum garnet ($Y_3Al_5O_{12}$ or YAG) fibers are available at an extremely high price from Saphicon Inc. (33 Powers St. Milford, NH, USA). While fine grained, polycrystallize alumina-mullite fibers (Nextel 720) can be obtained at a lower cost from the 3M company (3M Center, St. Paul, MN, USA), they are unable to withstand temperatures above 1300 °C due to microstructural rearrangment. More recently, however, research into more economical techniques for producing mullite ($3Al_2O_3 \cdot 2SiO_2$) and YAG fibers is underway.[20-22] Amorphous fibers can be produced by a laser melting, containerless technique (Containerless Research Inc., Evanston, IL, USA) involving rapid pulling of deeply undercooled melts and subsequent crystallization. Depending on the phase diagrams, this may be a general method for the production of any oxide as a fiber.

While the interfacial debonding mechanism has clearly been demonstrated in SiC materials reinforced with SiC fibers that were previously coated with a thin layer of compliant graphite (C) or boron nitride (BN), they only operate at ambient temperatures or under vacuum at high temperatures. In air at high temperatures both SiC and graphite decompose, leaving the ceramic body porous and friable. In the past few years, different types of oxide interfacial layers have been proposed to replace C or BN coatings around oxide fibers (e.g. saphire). One such coating is based on micaeous cleavage materials such as fluorophlogopite or hibonite ($CaO \cdot 6Al_2O_3$).[23] Alternatively, lanthanide phosphates such as monazite ($LaPO_4$) or zenotime (yttrium phosphate, YPO_4) have been introduced as oxidation resistant interfaces capable of operating up to 2000 °C in air.[23-27,13] While at first sight the monazite-type interfaces appear to be viable, bulk mechanical data for strength, toughness and stress-strain curves are still lacking. However, fiber push-out measurements of debonding shear strength (τ_d) have been made for monazite ($LaPO_4$)

coatings of various thickness, around saphire, embedded in Al_2O_3 or in YAG.[28] The debonding shear strength (τ_d) varied from 140 MPa to 110 MPa, where the latter corresponded to a minimum monazite thickness of 2 μm around YAG fibers.[28] Measurements of the analogous zenotime coating on YAG fibers yielded a τ_d of 95 MPa.[13] In comparison, τ_d's for graphite coatings are generally reported to be 10-15 MPa.[11] It is fair to say that optimum debonding shear strengths for oxides are not yet known, but at first glance they appear to be still too high for monazite-type interfaces, although there may be an optimum value such that higher values may promote more crack energy dissipation.

Another perceived problem with the monazite system is its sensitivity to decomposition under conditions of slight deviations from stoichiometry.[28] In the presence of Al_2O_3 it tends to form a magnetoplumbite ($Al_2O_3 \cdot 11La_2O_3$) and porosity, with some volatilization of phosphorus. Zenotime (YPO_4) appears to be more stable, eg. with YAG, due to its lack of 4f electrons.[26,27] However, YPO_4 is not necessarily compatible with many compounds (e.g. Al_2O_3). A further shortcoming of the interface slippage mechanism operating in the lanthanide phosphate-type systems is that it relies on the fiber preserving a smooth and clean interface. This places a stringent requirement on the manufacture and handling of fibers, and hard-to-control restrictions on subsequent changes in surface microstructure during prolonged service at high temperatures. The fibers tend to take on a corrugated surface mimicing the grain shapes in the polycrystalline matrix, as they attempt to achieve equilibrium dihedral angles with the matrix grains. The theories for smooth fiber/matrix pullout then no longer apply.

Since copious quantities of oxide fibers or weaves are not yet available, systematic investigation can still be carried out with model laminar ceramic composites.[14,15] Recently a strong and damage tolerant laminate system has successfully been fabricated based on a zenotime (yttrium phosphate, YPO_4) interphase.[16-19] A high flexural strength (e.g. 392 MPa) was derived from the choice of matrix to be a triple layer of yttria stabilized zirconia (3Y-TZP), zirconia toughened alumina (30 vol% 3Y-TZP – 70 vol% Al_2O_3), and 3Y-TZP again. The high interfacial debonding strength of YPO_4 was thus also offset by optimization of thermal expansion coefficient of the triple layered matrix with the interphase. The high temperature thermal properties of this oxide laminate system depend on the relative thermal expansion coefficients of the components, however, and still remain to be evaluated.

The aim of this work was to introduce a new mechanism of interfacial debonding which is less dependant upon mismatch of thermal expansion coefficients. It is postulated that an overall increase in toughness can be achieved by inducing a phase transformation in an oxide coating which is accompanied but a large, but negative volume change on cooling,

or significant unit cell shape change. The proposed mechanism is schematically illustrated in Fig. 1,[29] and is based on the analogy with transformation toughening in zirconia (ZrO_2) which is accompanied by a volume increase of (+) 3.0 % at 950 °C or (+) 4.9 % at room temperature. The terminology of "transformation weakening" was first introduced[30] to describe the deleterious effect of the -5.5 % volume contraction in enstatite ($MgO{\cdot}SiO_2$ or $MgSiO_3$) as it transforms from orthorhombic protoenstatite to monoclinic clinoenstatite at 865 °C on quenching. Elastic tensor calculations of the enstatite transformation strain[30,31] indicated an anisotropic volume contraction with a maximum of -16.5 % in the [c] axis of the product phase with respect to parent crystal lattice. This gives rise to oriented intragranular microcracks perpendicular to the [c] monoclinic axis.[29,31] Intragranular microcracks due to thermally induced transformation have been previously observed[32] in clinoenstatite grains which were overaged beyond a critical particle size of 7 μm.[33]

A distiction can be drawn between thermal versus stress-induced transformation. Displacive transformations can be associated with a critical particle size effect in dense ceramics.[33-37] Overaged grains exceeding their critical particle size transform spontaneously on cooling through their transformation temperature. Optimally aged grains can be metastably retained down to room temperature, but can be induced to transform through the action of shear or tensile stresses.[34,38-40] Fig. 1 illustrates overall toughening by a localized shear-induced mechanism. In a composite, the difference between a shear versus thermal induced mechanism is that in the latter, almost all of the interphase coating grains have already transformed at room temperature, while in the former, most of the grains are ideally at their optimum critical particle size ready to be stress induced by a propagating crack or by the critical resolved shear stress needed for transformation.[40-45]

The potential advantages of interphase debonding by a transformation weakening mechanism are suggested in Fig. 1, where a variety of synergistic toughening mechanisms may be activated. These include; (i) energy dissipation by creation of new surfaces as microcracks; (ii) in the shear-induced case, crack energy is used to overcome activation energy barrier and nucleate the transformation; (iii) frictional work is done by the crack as it debonds from the reinforcement and passes through the weakened interphase; (iv) load bearing by the fiber, with subsequent crack closure forces exerted on the main matrix crack, grain bridging e.g. in the case of an interphase coated reinforcement (fiber particulate, platelet or whisker).

The shear stress-induced transformation may be an extremely powerful toughening mechanism in fully dense bodies. In the as-fabricated state, the composite has maximum bulk strength, and specifically, transverse strength in directions perpendicular to fiber lengths. Should a matrix crack approach the fiber, however, it induces transformation

weakening in the interphase, but only in the immediate environment of the crack, rather than in all the interphases throughout the bulk of the material, as occurs in thermally-induced transformation.

During long term use, the fatigue properties are not expected to deteriorate catastrophically, since the transformational damage is localized to the interphase and is beneficial for toughening. Essentialy, in the long term, the stress-induced toughening reverts to thermally induced toughening. If crack healing in the transformed interphase did occur during prolonged use at high temperature, a useful feature would be to recycle the interphase. Heating above the transformation temperature to the high temperature volume expanded, parent phase should induce crack healing and restore an essentially dense and untransformed interphase in almost pristine condition.

For high temperature applications in an oxidative environment, oxide interphases are required, together with oxide reinforcement and matrix phases. Tables of currently known or suspected phase transformations in oxide ceramics have been published elsewhere,[29] and are a topic of ongoing research. For comparison and scientific completeness, transformations involving positive volume changes on cooling (e.g. zirconia (ZrO_2) where T_0=950 °C or the lanthanide sesquioxides (Ln_2O_3) where T_0=1850 °C on cooling) are also listed,[29,30,46-49] since it remains yet to be determined whether or not the generation of microcracking or stress intensity sites (also generated with volume increases) are beneficial for crack deflection along the interphase and resulting interphase debonding.

Again, for high temperature applications, the maximum use temperature is set by the transformation temperature (T_0), which, in the case of displacive or martensitic transformations, is known to vary by hysterisis for a given system. The transformation weakening effect is expected to operate over a range of temperatures up to T_0, provided that the microstructure of the interphase is appropriately designed. Factors such as interphase thickness, grain size and composition need to be controlled and maintained during prolonged annealing at elevated temperatures. The interphase needs to have stable phase equilibria with adjacent matrix and reinforcement compositions. For a shear stress-induced transformation, the critical particle size of an interphase will need to be preserved, e.g. by the addition of chemically compatible, non-transformable, second phases to inhibit grain growth. Thus a variety of metallurgical techniques such as chemical additions to produce second phase precipitates and grain boundary pining may be explored to inhibit grain growth above the critical grain size. In the case of a transformable second phase, its T_0 may cover an even higher temperature range. Multiple coatings with different T_0's may also be applied to cover a wider range of temperatures.

In this paper we describe work to demonstrate the feasibility of transformation weakening as a viable debonding mechanism in ceramic matrix composites. A model system was chosen based on the cubic (β) to tetragonal (α) transformation in cristobalite (SiO_2). The high temperature β structure transforms displacively to α at 265 °C on cooling, and is accompanied by ~3.2 % volume decrease. The critical particle size range for shear-induced transformation in chemically modified cristobalite was established in Part I of this work.[37] In the absence of commercially available mullite fibers, a model laminate configuration was chosen. In order to optimize the match of thermal expansion coefficients of mullite and cristobalite, to improve the sinterability of mullite, and to maximize the strength of the mullite matrix layers, a 60 vol% mullite/40 vol% cordierite mixture was used as the matrix phase.[37] A tape casting technique was used to engineer a series of laminated composites in various sequences of stacked and hot pressed tapes. The phase transformation and fracture behavior were investigated in laminated composites of mullite/cordierite matrix mixtures separated by a cristobalite interphase. The grain size of the polycrystalline β-cristobalite was controlled by varying the annealing time at 1300 °C, and examined by SEM. In addition, the effects of the laminate design and heating condition on the strength and toughness of the laminated composite were studied both qualitatively by optical microscopy and indentation techniques, as well as quantitatively by measuring flexure strengths.

II. Experimental Procedure

(1) Preparation of Powder and Laminate

Amorphous-type β-cristobalite powder was prepared by the solution-polymerization technique employing PVA solution as a polymeric carrier.[50,51] The details of the preparation method were described in a previous paper (Part I).[37] Amorphous-type cordierite powder was also prepared by the same method.[52] The cordierite powder was synthesized from $Mg(NO_3)_2 \cdot 6H_2O$ (reagent grade, Aldrich Chemical Co., Milwaukee, WI); $Al(NO_3)_3 \cdot 9H_2O$ (reagent grade, Aldrich Chemical Co., Milwaukee, WI) and Ludox AS-40 colloidal silica (40 wt% suspension in water, Du Pont Chemicals, Wilmington, DE). The average particle size of the amorphous-type cordierite powder, after calcination at 750 °C for 1 h and ball-milling for 12 h, was about 0.3 μm with a specific surface area of 80 m^2/g. Commercial mullite powder (KM Mullite-101 Kyotitsu, Nagoya, Japan), which had an average particle size of 0.8 μm and a specific surface area of 26 m^2/g, was used in the mullite/cordierite mixture.

The monolithic starting powders and the mullite/cordierite mixtures having different cordierite content were characterized for relevant properties such as thermal expansion coefficient, flexural strength, linear shrinkage behavior, and the phases formed after sintering. Specimens for the above tests were fabricated in the form of pressureless-sintered pellets which were prepared by uniaxial pressing at 20 MPa followed by cold isostatic pressing at 170 MPa for 10 min.

Laminates were fabricated by the tape casting process according to the procedure summarized in Fig. 2. The slurries consisted of ~25 vol% oxide powders, ~63 vol% solvent and 12 vol% organics. The 0.5 wt% (dry weight basis of oxide powder) polyvinyl butyral (PVB, Monsanto, St. Louis, MO) was added to the slurries as a dispersant. The solvent was composed of a mixture of trichloroethylene ($ClCH=CCl_2$, Aldrich Chemical Co., Milwaukee, WI) and ethanol (CH_3CH_2OH, Aldrich Chemical Co., Milwaukee, WI) while the organics included a binder (polyvinyl butyral (PVB), Monsanto, St. Louis, MO) and plasticizers (polyethylene glycol (PEG) 2000 and dioctyl phthalate (DP), Aldrich Chemical Co., Milwaukee, WI). After pulverization, dispersion and mixing by ball-milling two times, the slurries were stirred in vacuum. This helped in removing bubbles and adjusting the working viscosity. After ageing for 2 days, the slurries were tape cast using a doctor blade opening of 150-300 μm to obtain tape cast green sheets of 60-150 μm thickness. Drying of the cast tapes was carried out under a saturated solvent atmosphere for a day.

The green laminate composites had area dimensions of 25 mm × 51 mm after stacking green sheets. Thermocompression was performed at 10 MPa load for 30 min at 80 °C, which was the softening point of the organics. The organic additives were removed by heating to 550 °C in an air atmosphere, using a two step heating process. After these additives were burned out, the green laminates were iso-statically cold pressed at 170 MPa for 10 min. The laminated green bodies were pressureless sintered at 1350 °C for 1 h, in an air atmosphere. The laminates were also hot pressed by loading them in a graphite die and surrounding them with compatible oxides. Hot pressing was done under an argon atmosphere at 28 MPa, at a temperature of 1200 °C for 1 h.

All laminate composites after densification had a 30 layer repetitive sequence of matrix and interphase. These were made in different thickness ratios of matrix to interphase by stacking each green sheet in proportion to the respective thickness ratio after densification. After sintering, the laminates were cut into bend-bars, the cutting direction being parallel to the area length. The bend-bars with dimensions of 30 mm × 3.0 mm × 2.5-3.0 mm were polished to a 15 μm finish with diamond paste. The specimens were then annealed at 1300 °C for different times.

(2) Characterization

(A) Thermal Expansion Coefficient Measurement : The experiments for examining the variation of thermal expansion coefficient for different mixing ratios of mullite and cordierite were performed in a dilatometer (Netzsch Dilatometer, 402E, Germany). To obtain a relative density above 95% in each specimen they had to be sintered at different temperatures.

(B) Linear Shrinkage Behavior : The linear shrinkage of each specimen was measured in the temperature range of 900 °C - 1600 °C by determining the dimensions with Vernier callipers.

(C) X-ray Diffraction Analysis : To examine the phases formed after sintering of each starting powder/mixture, a Rigaku spectrometry (Dmax automated powder diffractometer, Rigaku/USA, Danvers, MA) with CuK_α radiation (40 kV, 40 mA) was used.

(D) Relative Density Measurement : The density for the sintered specimens was estimated by the Archimedes' method using distilled water as a displacement liquid. The relative density of each specimen was calculated from density of the mullite (3.18 g/cm^3), cordierite (2.52 g/cm^3) and cristobalite (α phase: 2.33 g/cm^3 and β phase: 2.26 g/cm^3) as a theoretical density at a given volume ratio.

(E) Flexural Test : 4-point flexural testing was performed using a 10 mm inner span and a 20 mm outer span, at a crosshead speed of 0.01 mm/min on a universal testing machine (model 4502, Instron Corp., Canton, MA). A minimum of five bars were tested for each composition. The apparent work of fracture was obtained by dividing the area under the load-displacement curve by the cross-sectional area of the sample.

(F) Indentation Test : A Vicker's hardness test was carried out with a micro-hardness tester (Zwick 3212, Mark V Lab. Inc.) under a 6 kg indentation load in order to study crack propagation profiles and interaction with the microstructure.

(G) Microstructure Characterization : The crack propagation behavior in the laminates after bend testing was observed by optical microscopy (Nikon SMZ-2T, Japan) and scanning electron microscopy (SEM, Model DS-130, International Scientific Instruments, Santa Clara, CA).

III. Results

(A) Composition of Laminate

Fig. 3 shows the variation of thermal expansion coefficient and flexural strength for the mullite/cordierite mixtures as a function of cordierite content. As expected, the thermal expansion coefficient and flexural strength decreased as cordierite content was increasesd.

To match the thermal expansion coefficient to the chemically stabilized β-cristobalite (1.5×10^{-6}/°C),[37] the mullite/cordierite layer should also have a low thermal expansion coefficient. The thermal expansion compatibility is an important factor in fabricating a stable laminate structure without thermal stresses at the interface. However, in order to design a high flexural strength laminate, a low cordierite content is important in this case.

The trends in variation of shrinkage of the compacts for each powder at various sintering temperatures are shown in Fig. 4. An amorphous-type β-cristobalite powder compact reached almost full densification at 1300 °C. The commercial mullite powder compact could not be densified below 1600 °C. In the case of the synthetic, amorphous-type cordierite powder compact, densification occurred earlier than that in cristobalite. As 10 wt% amorphous-type cordierite was added to the mullite, the sintering shrinkage increased largely in comparison with the shrinkage of monolithic mullite. In the mullite/cordierite mixture, the sintering temperature was limited to below 1470 °C because of the melting of cordierite (m.p : 1475 °C).

Fig. 5 displays X-ray diffraction patterns for each compact after sintering at 1300 °C. β-cristobalite phase was observed to have crystallized from the amorphous-type cristobalite powder compact (Fig. 5 (a)). Crystalline α-cordierite phase was detected from the amorphous-type cordierite (Fig. 5 (b)). The 60 wt% mullite and 40 wt% amorphous-type cordierite powder compact showed mullite and α-cordierite phases without any chemical reaction. To design a laminate composite with matching thermal expansion coefficients and sintering shrinkages between laminated materials and still have reasonable strength, the 40 wt% cordierite content was selected for the mullite/cordierite matrix layers.

(B) Sintering and Annealing Effects on Fracture Behavior

To study the fracture behavior of the laminates, three kinds of laminates with the same matrix to interphase thickness ratio were studied for different laminate compositions and heating conditions. The detailed conditions are listed in Table I. The sintering temperature was determined from the densification temperature of each component as indicated by the observations of Fig. 4. For pressureless sintering and hot pressing, the sintering temperatures were selected to be 1350 °C and 1200 °C, respectively.[37] After densification, annealing was done at 1300 °C. Table II displays a relative density of each component at each densification condition. Hot pressing improved densification.

The relative ratios of α, β-cristobalite phases, average grain size, strength, and work of fracture obtained for each experiment at different annealing times are listed in Table III. For experiment 2, the sintered laminate was denser than the laminate in experiment 1 due to the higher sinterability of the cordierite powder. Morever, good compatibility of

thermal expansion can be expected between the cordierite and cristobalite laminate. However, in spite of the low thermal stress between the laminate and dense microstructure, the strength of the experiment 2 at each annealing time was lower than that of experiment 1. This could be attributed to the low strength of cordierite. In all cases, the strength decreased when the annealing time was increased. The work of fracture showed maximum values at different annealing times for each experiment. The maximum work of fracture of 1.93 kJ/m^2 in experiment 1 was observed at annealing times of 30 h. In contrast, the highest work of fracture of 2.38 kJ/m^2 was observed in the more dense hot-pressed laminate with a strength of 131 MPa at annealing times of just 10 h. This indicated that the hot-pressed laminate was more appropriate for phase transformation weakening when it had a dense microstructure.

Fig. 6 presents load-deflection curves for experiment 3, under un-notched, 4-point flexural testing, as a function of annealing time. For the un-annealed bend bar, the curve showed brittle fracture behavior. For the 10 h annealing case, the curve showed non-catastrophic fracture behavior. The step-wise load drops were characteristic of non-brittle fracture. This implied that the matrix crack was notably deflected by the interphase, giving a significant work of fracture. The optical micrographs confirming crack deflection in the laminate samples are seen in Fig. 7. In comparison with the un-annealed laminate, the crack was notably deflected, especially in the central shear region of the cristobalite layer in the laminate annealed for 10 h. Pronounced delaminations between the mullite/cordierite mixture layer and cristobalite layer were also detected after flexural testing of the same sample. The relation between the work of fracture, strength, and average grain size is shown in Fig. 8. The result showed a parabolic curve form. The curves had a maximum work of fracture in the range from 100 to 150 MPa strength except in experiment 2. At the maximum point of work of fracture for each case, the laminates had an average grain size of 4-5 μm, as shown in Table III. The strength decreased with increasing average grain size. This meant that microcracks[37] in the cristobalite layer, which increased when annealing time was increased, decreased the frexural strength in the laminate structure. Cracks occurred due to thermally-induced transformation during the cooling process.[37]

The thermally-induced cracks in the hot-pressed laminated cristobalite layer before conducting flexural strength tests are shown in Fig. 9. In a laminate annealed for 10 h, no severe crack existed in the cristobalite layer (Fig. 9 (a)). In contrast, a 36 h annealed sample, with an average grain size of about 7.3 μm, had a severe crack inside the cristobalite layer. The laminate, which had the severe microcrack, showed a low strength even though matrix crack deflection was observed in the flexural-tested laminate as shown in Fig. 6. The thermally-induced microcracks in the cristobalite layer played the role of a

crack deflecting source. However, this kind of deflection did not decrease crack energy significantly in this laminate system. The excessive work of fracture in the laminate annealed for 10 h indicated that here, the crack deflection occurred mainly by shear stress-induced phase transformation, and not just by the microcracks caused by thermally-induced phase transformation.

To examine the interaction between crack propagation and the laminated microstructure, Vickers indentation cracks were introduced and the SEM micrograph is shown in Fig. 10. Indent-induced cracks, in the laminate hot-pressed and annealed for 10 h, displayed a preferred propagation path through the mullite/cordierite layer. However, the crack did not cross the cristobalite layer. This indicated that the indentation produced cracks along the cristobalite layer by the phenomenon of transformation induced weakening.

(C) Thickness Ratio Effect on Fracture Behavior

Laminates experienced a large thickness change after densification because of the complicated processing variables. The thickness ratio of the green body was not consistent with the thickness ratio of the densified body. Table IV summarizes the variation of strength and work of fracture as a function of thickness ratio between cristobalite and the mullite/cordierite matrix. The laminates were hot-pressed and annealed for 10 h. The given thickness ratios in Table IV were determined by optical microscopy, by measuring the thickness of each layer in a densified laminate.

When the thickness ratio of cristobalite to the mullite/cordierite layer increased, the strength decreased. The strength was as low as 48 MPa at a thickness ratio of 5 : 1. Work of fracture was also quite low in the laminate having a thicker cristobalite layer than the mullite/cordierite layer. On the other hand, the laminate having the thickness ratio of 1 : 5 showed a high work of fracture of 2.38 kJ/m^2. Figs. 11 and 12 are load-deflection curves and optical stereo micrographs for the laminates having different thickness ratios. At the thickness ratio of 3 : 1, the fracture curve followed similar behavior to the brittle material with a low strength of 52 MPa. Crack deflection occurred for the thickness ratio of 1 : 1 and for the cases where there was a thicker mullite/cordierite composite layer than cristobalite layer. For the thickness ratio of 1 : 7, a notable crack deflection was observed. However, the work of fracture was lower than the laminate having a thickness ratio of 1 : 5. This may have been due to some part of the thin cristobalite interphase in the laminate having thickness ratio of 1 : 7 which did not work as a phase transformation weakening layer, because there was not enough interphase thickness to provide an easier propagation

path for the deflection of the matrix crack. The arrows in the Fig. 12 (e) indicate the matrix crack passing the thin cristobalite interphase without deflection.

IV. Discussion

The cordierite prepared by the PVA solution-polymerization route was highly sinterable. Thus, it was very effective in improving the densification of the cordierite/mullite mixture despite the poor sinterability of mullite (Fig. 4). During hot pressing, this improvement in sinterability resulted in a more densified microstructure at a relatively low temperature of 1200 °C under 23 MPa pressure. The high work of fracture in the hot-pressed laminate was attributed to the high strength of the dense microstructure as well as the better response of the cristobalite interphase to shear stress-induced transformation. The hot-pressed laminate had a more uniform grain size of cristobalite than did the pressureless-sintered laminate.[37] The laminate annealed for a long time possessed a low strength. However, the work of fracture was higher than for the un-annealed laminate (Table III and Fig. 6). This was attributed to the notable crack deflection by thermally-induced cracks in the cristobalite interphase. In this case, crack propagation did not consume as much energy, resulting in lower work of fracture than the laminate having crack deflection by shear stress-induced transformation. Crack deflection by the thermally-induced microcracks showed a long displacement without pronounced step-wise load drops (Fig. 6). The superior mechanical behavior exhibited by the optimally aged interphase (10 h at 1300 °C) was consistent with a shear stress-induced transformation mechanism.

The laminate having a thickness ratio of 1 : 7 yielded a lower work of fracture than did the laminate having thickness ratio of 1 : 5. This was attributed to the probability of a crack tip meeting a grain to be acted upon as a crack energy consuming source by a phase transformation being quite low in the laminate with the thin cristobalite layer. As seen in Fig 11, a low frequency of step-wise load drop in the laminate of 1 : 7 thickness ratio, in comparison with the laminate of 1 : 5 thickness ratio, explains the passing of the matrix crack through the thin cristobalite layer.

A new laminate design can be considered for higher strength and work of fracture from the results of this study. As shown in the comparison of fracture behavior between the cordierite laminate with cristobalite interphase and the cordierite/mullite laminate with cristobalite interphase (Table III), the strengh of the laminate was affected more by the strength of the interphase material than by the compatibility of thermal expansion and sintering shrinkage in the laminate structure. Thus a very low cordierite content mullite mixture could be substituted for monolithic mullite. In the latter case, for densification, hot

pressing at higher temperature would be suggested. At the same time, a cristobalite and mullite combination could be used as another type of transformable interphase. The cristobalite/mullite combination can be expected for inhibition of severe thermally-induced microcracks by excessive grain growth of cristobalite during the high temperature sintering process. Further work on this design is in progress.

V. Conclusions

Matrix-crack deflection by shear stress-induced phase transformation was observed at the critical grain size of 4-5 μm, resulting in a comparatively high work of fracture. A hot-pressed laminate sample, annealed at 1300 °C for 10 h with an interphase to matrix thickness ratio of 1 : 5, showed the highest work of fracture of 2.38 kJ/m^2 with a strength of 131 MPa. A comparatively low strength in spite of high work of fracture at longer annealing time was attributed to severe microcracking in the cristobalite interphase. The severe microcracking, which was caused by spontaneous thermally-induced phase transformation during the cooling process, provided an easier propagation path for crack deflection without as much reduction in crack energy. The pronounced crack deflection by induced phase transformation was observed in laminates with thickness ratios lesser than 1 : 1. The laminate having a 1 : 7 thickness ratio revealed a lower frequency of step-wise load drops than did the 1 : 5 ratio in the load-deflection curve. This meant that a matrix crack in the laminate having a 1 : 7 thickness ratio passed through a few thin cristobalite layers without crack deflection.

Thus, the design of an oxide laminate composite consisting of a mullite/cordierite matrix separated by a transformation weakened cristobalite interphase has successfully been engineered. The mechanical behavior exhibited by the optimally aged interphase (10 h at 1300 °C) is consistent with a shear stress-induced transformation mechanism. Conventional ceramic processing techniques of tape casting and hot pressing were used, but the concept of transformation weakening of interphases leading to overall graceful failure has essentially been demonstrated. Although the absolute values of strength are modest due to the weak matrix layers, this work lays down the foundation for the development of high strength and toughness composites based on strong, load bearing fibers such as mullite or YAG, as soon as they become commercially available. There is wide scope for theoretical mechanics design, together with improved coating and processing techniques. However, this mechanism for inducing interphase debonding is still applicable with other choices of higher temperature transformable coatings in combination with chemically compatible oxide fibers and matrices.

Acknowledgment: This work was supported by the US Air Force Office of Scientific Research, through Dr. Alexander Pechenik, under grant number AFOSR-F49620-93-1-0227.

References

[1]A. G. Evans, "Perspectives on the Development of High Toughness Ceramics," *J. Am. Ceram. Soc.*, **73** [2] 187-206 (1990).

[2]D. B. Marshall, B. N. Cox, and A. G. Evans, "The Mechanics of Matrix Cracking in Brittle Matrix Fiber Composites," *Acta Metall. et Materialia*, **33** [11] 2013-21 (1985).

[3]B. Budiansky, J. W. Hutchinson, and A. G. Evans, "Matrix Fracture in Fiber Reinforced Ceramics," *J. Mechanics and Physics of Solids*, **34** [2] 167-89 (1986).

[4]M. Y. He and J. W. Hutchinson, "Crack Deflection at an Interphase between Dissimilar Elastic Materials," *Int. J. Solids and Structures*, **25**, 1053-67 (1989).

[5]A. G. Evans and D. B. Marshall, Overview No. 85, "The Mechanical Behavior of Ceramic Matrix Composites," *Acta Metall. et Materialia*, **37** [10] 2567-83 (1989).

[6]R. J. Kerans, R. S. Hay, N. J. Pagano, and T. A. Parthasarathy, "The Role of Fiber-Matrix Interface in Ceramic Composites," *Am. Ceram. Soc. Bull.*, **68** [2] 429-42 (1993).

[7]K. M. Prevo and J. J. Brennan, "High-Strength Silicon Carbide Fiber-Reinforced Glass-Matrix Composites," *J. Mater. Sci.*, **15** [2] 463-468 (1980).

[8]J. J. Brennan, "Interfacial Characterization of Glass and Glass-Ceramic Matrix/Nicalon SiC Fiber Composites," pp. 549-60 in *Tailing Multiphase and Composite Ceramics*. Edited by R. T. Tressler, G. L. Messing, C. G. Pantano, and R. E. Newnham. Plenum Press, New York, 1986.

[9]H. C. Cao, E. Bischoff, O. Sbaizero, M. Rühle, A. G. Evans, D. B. Marshall, and J. J. Brennan, "Effect of Inferfaces on the Properties of Fiber-Reinforced Ceramics," *J. Am. Ceram. Soc.*, **73** [6] 1691-99 (1990).

[10]C. M. Huang, Y. Xu, D. Zhu, and W. M. Kriven, "Combustion Synthesized β'-SiAlON Composites Reinforced with SiC Monofilaments," *J. Mater. Sci. and Eng.*, **A, 188**, 341-51 (1994).

[11]C. M. Huang, D. Zhu, Y. Xu, T. Mackin, and W. M. Kriven , "Interfacial Properties of SiC Monofilament Reinforced β'-SiAlON Composites," J. *Mater. Sci. and Eng.*, **A, 201**, 159-68 (1995).

[12]C. M. Huang, D. Zhu, Y. Xu, W. M. Kriven, and C. Y. Yuh, "SiC_f/O'-SiAlON Composites: Properties and Oxidation Retained Properties," *J. Mater. Sci.*, **A, 220** [1-2] 174-84 (1996).

[13]D. H. Kuo, W. M. Kriven, and T. J. Mackin, "Control of Interfacial Properties Through Fiber Coatings: Monazite Coatings in Oxide/Oxide Composites," *J. Am. Ceram. Soc.*, **80** (1997), in press.

[14]W. J. Clegg, K. Kendall, N. M. Alford, D. Birchall, and T. W. Button, "A Simple Way to Make Tough Ceramics," *Nature*, **347**, 455-57 (1990).

[15]W. J. Clegg, "The Fabrication and Failure of Laminar Ceramic Composites," *Acta Metall.*, **40** [11] 3085-93 (1992).

[16]D. H. Kuo and W. M. Kriven, "A Strong and Damage Tolerant Oxide Laminate, " *J. Am. Ceram. Soc.*, **80** (1997), in press.

[17]D. H. Kuo and W. M. Kriven, "Oxide Laminates with High Strength and Work-of-Fracture," *Mater. Res. Soc. Symp.*, (1997), in press.

[18]D. H. Kuo and W. M. Kriven, "Fracture of Multilayer Oxide Composites," *J. Mater. Sci. and Eng.*, **A** (1997), in press.

[19]D. H. Kuo and W. M Kriven, "Microstructure and Mechanical Evaluation of Yttrium Phosphate-Containing and Lanthanum Phosphate-Containing Zirconia Laminates," *Ceram. Sci. and Eng. Proc.*, (1997), in press.

[20]W. M. Kriven, D. Zhu, M. H. Jilavi, J. K. R. Weber, B. Cho, J, Felten, and P. C. Nordine, "Synthesis and Microstructure of Mullite Fibers Grown from Deeply Undercooled Melts," in *Ceramic Microstructures'96*. Edited by A. P. Tomsia and A. M. Glaeser, Plenum Press, New York, (1997), in press.

[21]J. J. Felten, J. K. R. Weber, P. C. Nordine, B. Cho, N. Lockwood, W. M. Kriven, M. H. Jilavi, and D. Zhu, "A Novel Technique for Producing Ceramic Fibers," *Ceram. Sci. and Eng. Proc.*, (1997), in press.

[22]D. Zhu, M. H. Jilavi, and W. M. Kriven, "Synthesis and Characterization of Mullite and YAG fibers Grown from Deeply Undercooled Melts," *Ceram. Sci. and Eng. Proc.*, (1997), in press.

[23]P. E. D. Morgan and D. B. Marshall, "Functional Interfaces for Oxide/Oxide Composites," *Mater. Sci. and Eng.*, **A, 162**, 15-25 (1993).

[24]P. E. D. Morgan and D. B. Marshall, "Ceramic Composites of Monazite and Alumina," *J. Am. Ceram. Soc.*, **78** [6] 1553-63 (1995).

[25]P. E. D. Morgan and D. B. Marshall, "Ceramic Composites Having a Weak Bond Material Selected from Monazites and Zenotimes," US Patent No. 5,514,474 May 7th, (1996).

[26]D. H. Kuo and W. M. Kriven, "Characterization of Yttrium Phosphate and a Yttrium Phosphate/Yttrium Aluminate Laminate," *J. Am. Ceram. Soc.*, **78** [11] 3121-24 (1995).

[27]D. H. Kuo and W. M. Kriven, "Microstructure and Mechanical Response of Lanthanium Phosphate/Yttrium Aluminate and Yttrium Phosphate/Yttrium Aluminate Systems," *Ceram. Sci. and Eng. Proc.*, **17 B,** 233-40 (1996).

[28]D. H. Kuo and W. M. Kriven, "Chemical Stability, Microstructure and Mechanical Behavior of $LaPO_4$-Containing Ceramics," *J. Mater. Sci. and Eng.*, **A, 210** [1-2] 123-34 (1996).

[29]W. M. Kriven, "Displacive Phase Transformations and Their Applications in Structural Ceramics," *J. de Physique IV, Colloque* **C8**, 101-110 (1995).

[30]W. M. Kriven, "Possible Alternative Transformation Tougheners to Zirconia: Crystallographic Aspects," *J. Am. Ceram. Soc.*, **71** [12] 1021-30 (1988).

[31]W. M. Kriven, C. M. Huang, D. Zhu, Y. Xu, and S. C. Mirek, "Transformation Toughening of Titania Composites by Transformation Weakening of Enstatite Interphases," *J. Am. Ceram. Soc.*, to be published.

[32]W. E. Lee and A. H. Heuer, "On the Polymorphism of Enstatite," *J. Am. Ceram. Soc.*, **70** [5] 349-60 (1987).

[33]E. C. Bloor, "Conversion in Steatite Ceramics," *J. Br. Ceram. Soc.*, **2**, 309-16 (1964).

[34]A. H. Heuer, N. Claussen, W. M. Kriven, and M. Rühle, "Stability of Tetragonal ZrO_2 Particles in Ceramic Matrices," *J. Am. Ceram. Soc.*, **65** [12] 642-50 (1982).

[35]W. M. Kriven, C. J. Chan, and E. A. Barinek, "The Particle-Size Effect of Dicalcium Silicate in a Calcium Zirconate Matrix"; pp. 145-55 in Advances in Ceramics, Vol. 24, *Science and Technology of Zirconia III*. Edited by S. Somiya, N. Yamamoto, and H. Yanagida. American Ceramic Society, Westerville, OH, 1988.

[36]C. J. Chan, W. M. Kriven, and J. F. Young, "Physical Stabilization of the $\beta \rightarrow \gamma$ Transformation in Dicalcium Silicate." *J. Am. Ceram. Soc.*, **75** [6] 1621-27 (1992).

[37]S. J. Lee and W. M. Kriven, "Toughening of Ceramic Composites by Transformation Weakening of Interphases (Part I. Powder Preparation and Critical Size Effect of Chemically Stabilized β-cristobalite)," *J. Am. Ceram . Soc.*, (1997), submitted.

[38]D. Zhu and W. M. Kriven, "Shear Induced Transformation and Plasticity in Enstatite," *J. Am. Ceram. Soc.*, submitted.

[39]D. Zhu and W. M. Kriven, "Shear Induced Transformation in Enstatite," *Ceram. Sci. and Eng. Proc.*, **17 A**, 383-90 (1996).

[40]M. Rühle and W. M. Kriven, "Stress-Induced Transformations in Composite Zirconia Ceramics," *Ber. der Bunsengesellschaft für Physikalische Chemic.*, **87,** 222-28 (1983).

[41]A. H. Heuer and M. Rühle, "Phase Transformations in ZrO_2-Containing Ceramics: II, The Martensitic Reaction t-ZrO_2"; pp. 14-32 in Advances in Ceramics, Vol 12, *Science and*

Technology of Zirconia II. Edited by N. Claussen, M. Rühle, and A. H. Heuer. American Ceramic Society, Westerville, OH, 1984.

[42]W. M. Kriven, "Displacive Transformation Mechanism in Zirconia Ceramics and Other Non-metals"; pp. 223-37 in *Tailoring Multiphase and Composite Ceramics*. Edited by R. T. Tressler, G. L. Messing, C. G. Pantano, and E. Newnham. Plenum, New York, 1986.

[43]W. M. Kriven, "The Transformation Mechanism of Spherical Zirconia Particles in Alumina"; pp. 64-77 in Advances in Ceramics, Vol 12, *Science and Technology of Zirconia II*. Edited by N. Claussen, M. Rühle, and A. H. Heuer. American Ceramic Society, Westerville, OH, 1984.

[44]A. H. Heuer and M. Rühle, "On the Nucleation of the Martensitic Transformation in Zirconia," *Acta Metall. et Mater.*, **33**, 2101-12 (1985).

[45]W. M. Kriven, "Martensitic Toughening of Ceramics," *Mater. Sci. and Eng.*, **A 127**, 249-55 (1990).

[46]Y. Fu, A. G. Evans, and W. M. Kriven, "Microcrack Nucleation in Ceramics Subject to a Phase Transformation," *J. Am. Ceram. Soc.*, **67** [9] 626-30 (1984).

[47]P. D. Jero and W. M. Kriven, "High Temperature Transformation Toughening of Magnesia by Terbia"; pp. 190-97 in *Science and Technology of Zirconia V*. Edited by S. P. S. Badwal, M. J. Bannister, and R. H. J. Hannink. Technomic Publishing Company, Pennsylvania, 1993.

[48]O. Sudre, K. R. Venkatachari, and W. M. Kriven, "Kinetics and Crystallography of the Monoclinic (B) to Cubic (C) Transformation in Dysprosia"; pp. 180-89 in *Science and Technology of Zirconia V*. Edited by S. P. S. Badwal, M. J. Bannister, and R. H. J. Hannink. Technomic Publishing Company, Pennsylvania, 1993.

[49]Y. J. Kim and W. M Kriven, "Crystallography and Microstructural Studies of Phase Transformations in Dysprosia (Dy_2O_3)," *J. Mater. Res.*, submitted.

[50]M. A. Gulgun and W. M. Kriven, "A Simple Solution-Polymerization Route for Oxide Powder Synthesis"; pp. 57-66 in Ceramic Transactions, Vol. 62, *Science, Technology, and Commercialization of Powder Synthesis and Shape Forming Processes*. Edited by J. J Kingsley, C. H. Schilling, and J. H. Adair. American Ceramic Society, Westerville, OH, 1996.

[51]M. A. Gulgun, M. H. Nguyen, and W. M. Kriven, "Polymeric Organic-Inorganic Synthesis of Mixed Oxides," *J. Am. Ceram. Soc.*, (1997), submitted.

[52]S. J. Lee and W. M. Kriven, "Nano-size Amorphous Cordierite Powder Prepared by a Solution-Polymerization Route," *J. Am. Ceram. Soc.*, (1997), submitted.

Figure Captions

Figure 1. Schematic diagram illustrating "transformation weakening of ceramic interphases" leading to overall toughening of a ceramic matrix composite. In thermally induced transformations, all interphases are pre-transformed before the approach of a crack, with some consequent loss of overall strength of the material. In the ideal shear-stress induced case, an on coming crack induces a transformation in its immediate environment, with strength only minimally reduced throught the bulk. Maximum toughening is achieved, since the propagating crack needs to do work to overcome the nucleation barrier and cause transformation, and onset of the other synergistic toughening mechanisms occurs.

Figure 2. Flow chart of tape casting procedure for fabrication of laminated composites.

Figure 3. Variation of thermal expansion coefficient and flexural strength for mullite/cordierite mixture as a function of cordierite content.

Figure 4. Shrinkage behavior for the powder compacts of amorphous-type cristobalite, cordierite, commercial mullite, and their mixture at various sintering temperatures.

Figure 5. X-ray diffraction patterns of (a) amorphous-type cristobalite, (b) amorphous-type cordierite, and (c) 60 wt% mullite and 40 wt% amorphous-type cordierite mixture after sintering at 1300 °C for 1 h.

Figure 6. Load-deflection curves (from experiment 3) for laminates of 15 mullite/cordierite matrix layers separated by cristobalite interphases under 4-point flexural testing, as a function of annealing time at 1300 °C.

Figure 7. Optical micrographs (from experiment 3) of crack propagation in laminated samples annealed at 1300 °C for (a) 0 h and (b) 10 h after 4-point flexural testing.

Figure 8. Relation between strength, work of fracture, and average grain size in laminates of mullite/cordierite separated by cristobalite interphases.

Figure 9. SEM micrographs of hot-pressed laminates annealed at 1300 °C for (a) 10 h and (b) 36 h. A pronounced thermally-induced microcrack was observed propagating in the cristobalite interphase in the laminate annealed for 36 h.

Figure 10. SEM micrograph of indentation crack pattern in hot-pressed laminate annealed for 10 h.

Figure 11. Load-deflection curves for hot-pressed laminates having different densified thickness ratios (annealing time : 10 h).

Figure 12. Optical micrographs of crack propagation in hot-pressed laminates having different densified thickness ratios of (a) 5 : 1, (b) 3 : 1, (c) 1 : 1, (d) 1 : 5, and (e) 1 : 7 after annealing for 10 h.

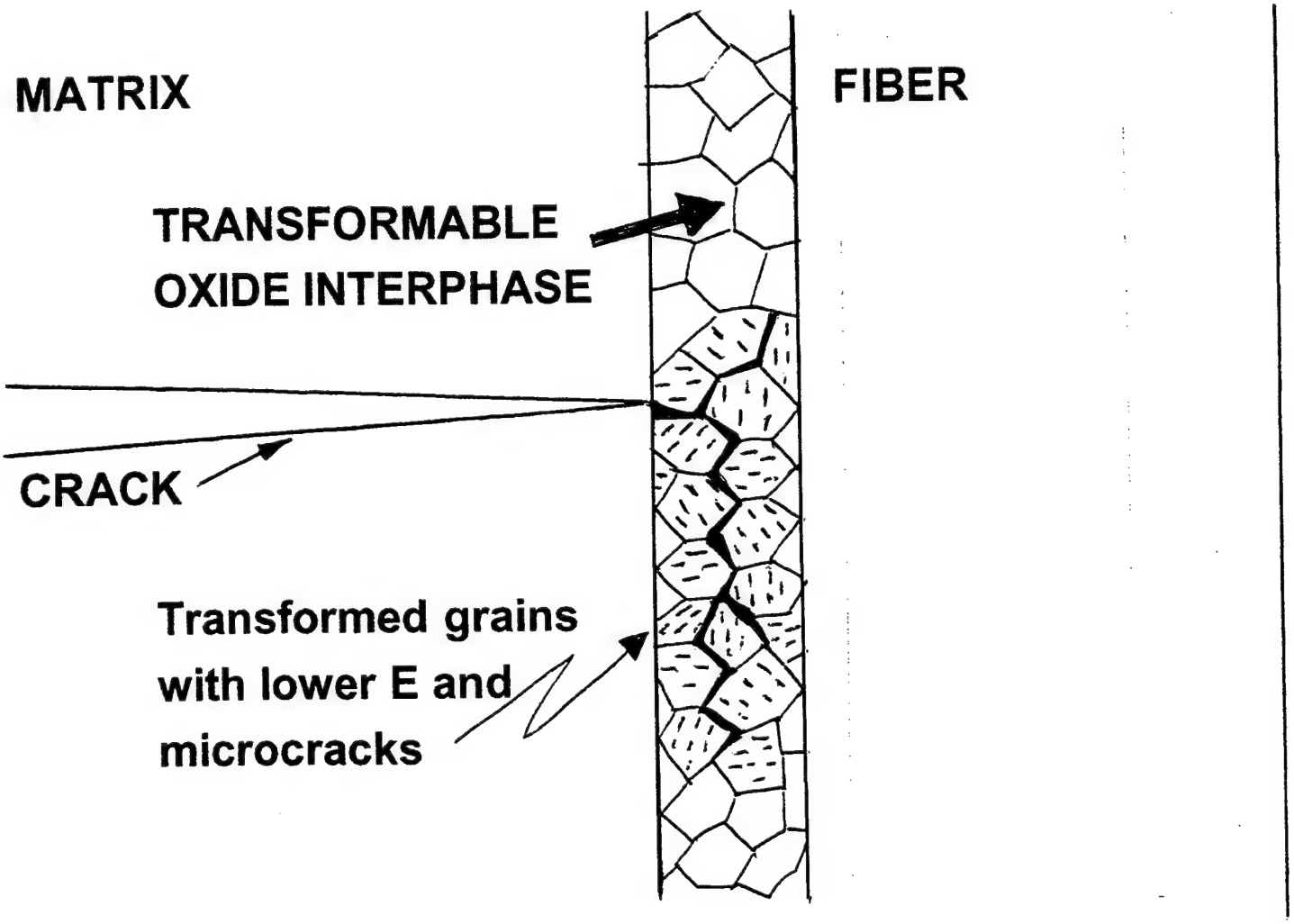
MATRIX
FIBER
TRANSFORMABLE
OXIDE INTERPHASE
CRACK
Transformed grains
with lower E and
microcracks

Fig 1.

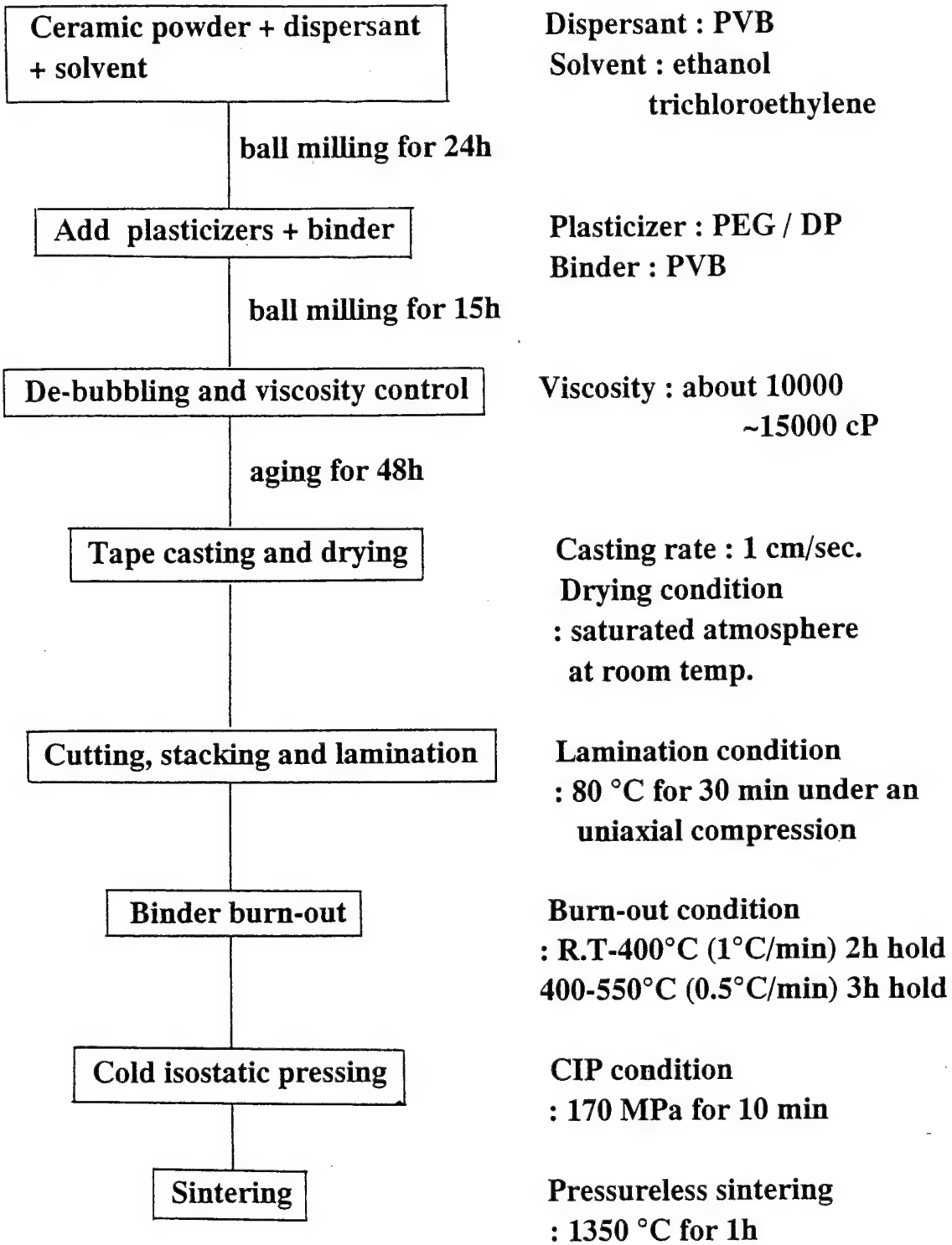
Ceramic powder + dispersant + solvent
Dispersant : PVB
Solvent : ethanol
trichloroethylene
ball milling for 24h
Add plasticizers + binder
Plasticizer : PEG / DP
Binder : PVB
ball milling for 15h
De-bubbling and viscosity control
Viscosity : about 10000 ~15000 cP
aging for 48h
Tape casting and drying
Casting rate : 1 cm/sec.
Drying condition
: saturated atmosphere at room temp.
Cutting, stacking and lamination
Lamination condition
: 80 °C for 30 min under an uniaxial compression
Binder burn-out
Burn-out condition
: R.T-400°C (1°C/min) 2h hold
400-550°C (0.5°C/min) 3h hold
Cold isostatic pressing
CIP condition
: 170 MPa for 10 min
Sintering
Pressureless sintering
: 1350 °C for 1h
Hot pressing
: 1200 °C for 1h at 28 MPa under an Ar atmosphere

Figure 2

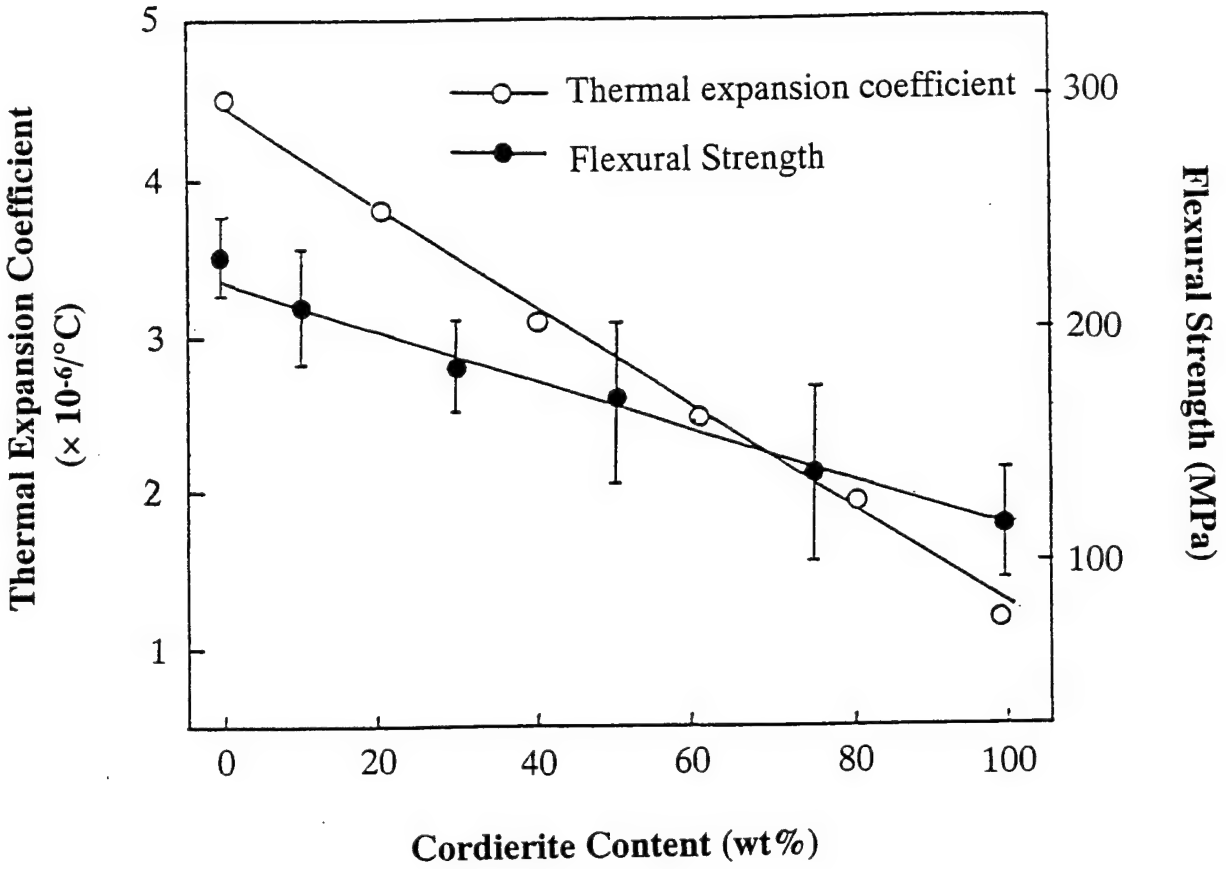
Thermal Expansion Coefficient
(× 10-6/°C)
Thermal expansion coefficient
Flexural Strength
Flexural Strength (MPa)
Cordierite Content (wt%)
5
4
3
2
1
300
200
100
0
20
40
60
80
100

Figure 3

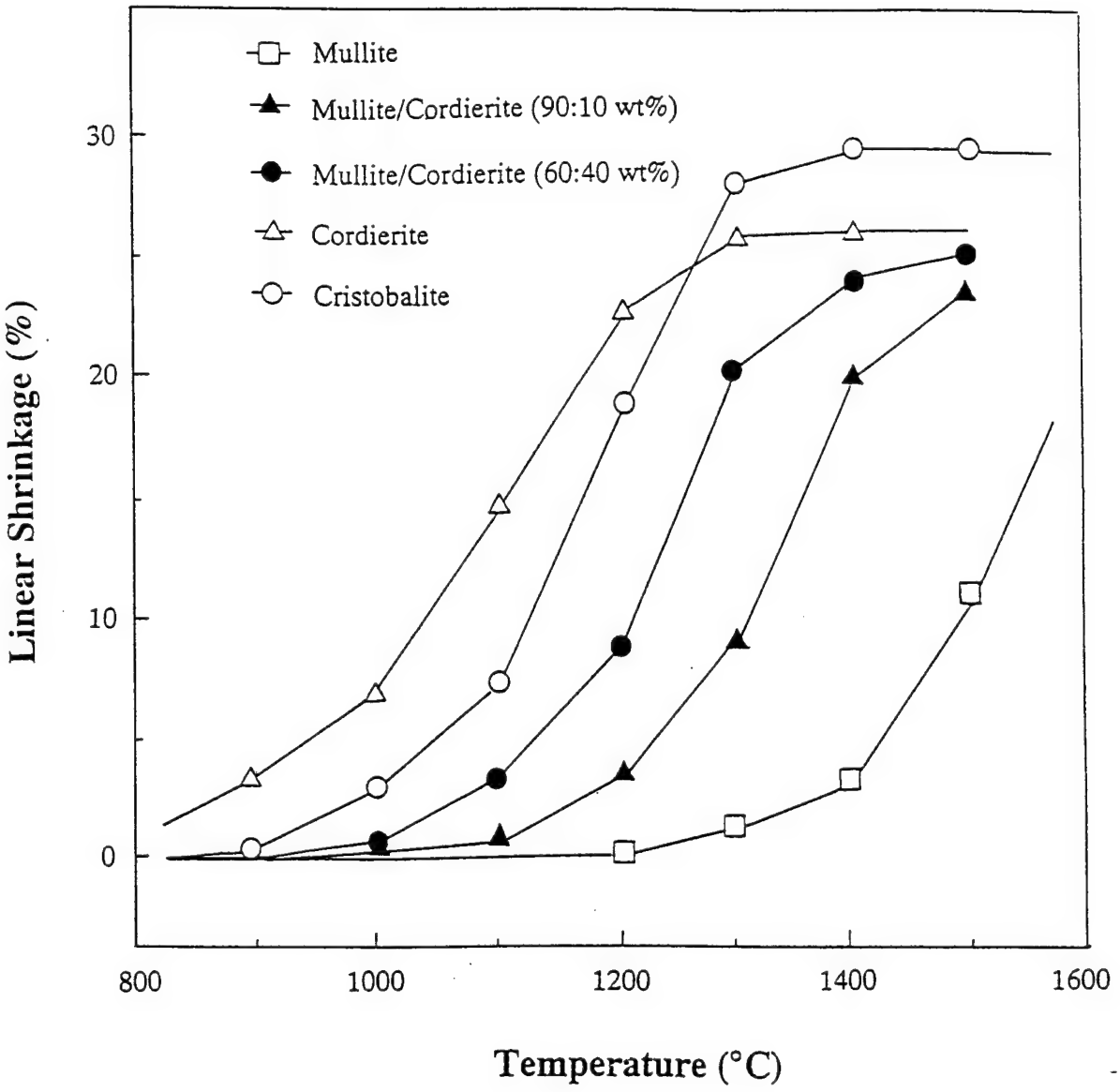
Mullite
Mullite/Cordierite (90:10 wt%)
Mullite/Cordierite (60:40 wt%)
Cordierite
Cristobalite
Linear Shrinkage (%)
0
10
20
30
800
1000
1200
1400
1600
Temperature (°C)

Figure 14

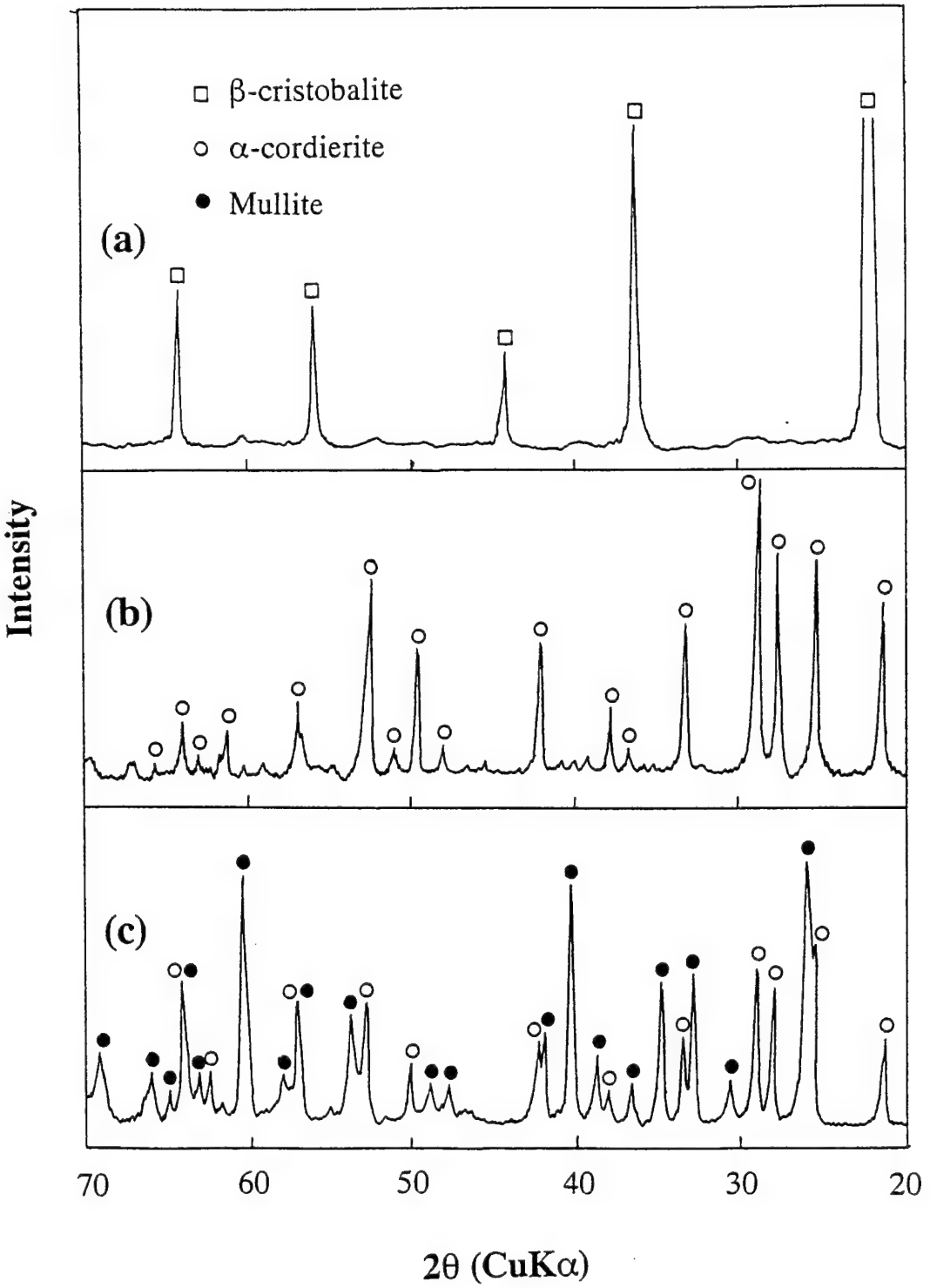
□ β-cristobalite
○ α-cordierite
● Mullite
(a)
(b)
(c)
Intensity
70
60
50
40
30
20
2θ (CuKα)

Figure 4/5

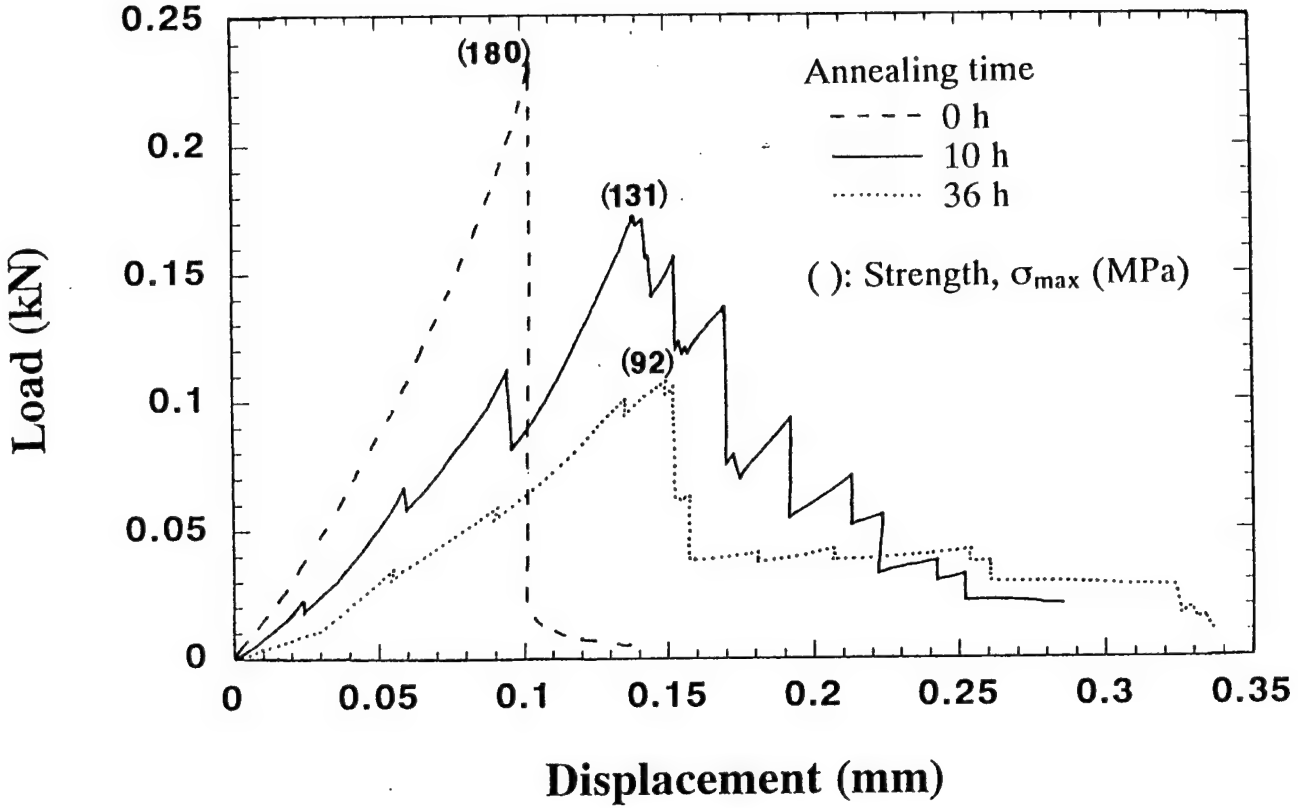
0.25
0.2
0.15
0.1
0.05
0
Load (kN)
(180)
(131)
(92)
Annealing time
0 h
10 h
36 h
( ): Strength, σmax (MPa)
0
0.05
0.1
0.15
0.2
0.25
0.3
0.35
Displacement (mm)

Figure 5 6

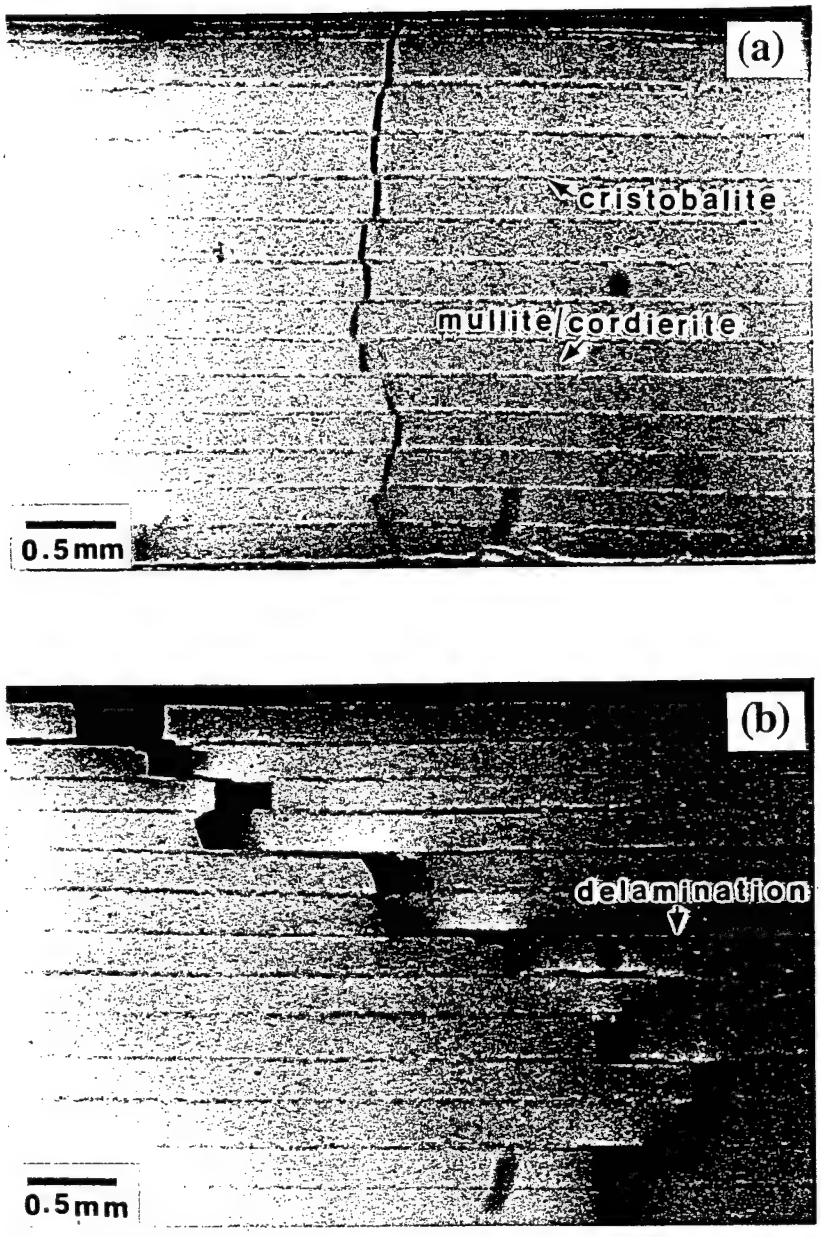
(a)
cristobalite
mullite/cordierite
0.5mm
(b)
delamination
0.5mm
crack propagation

Figure 67

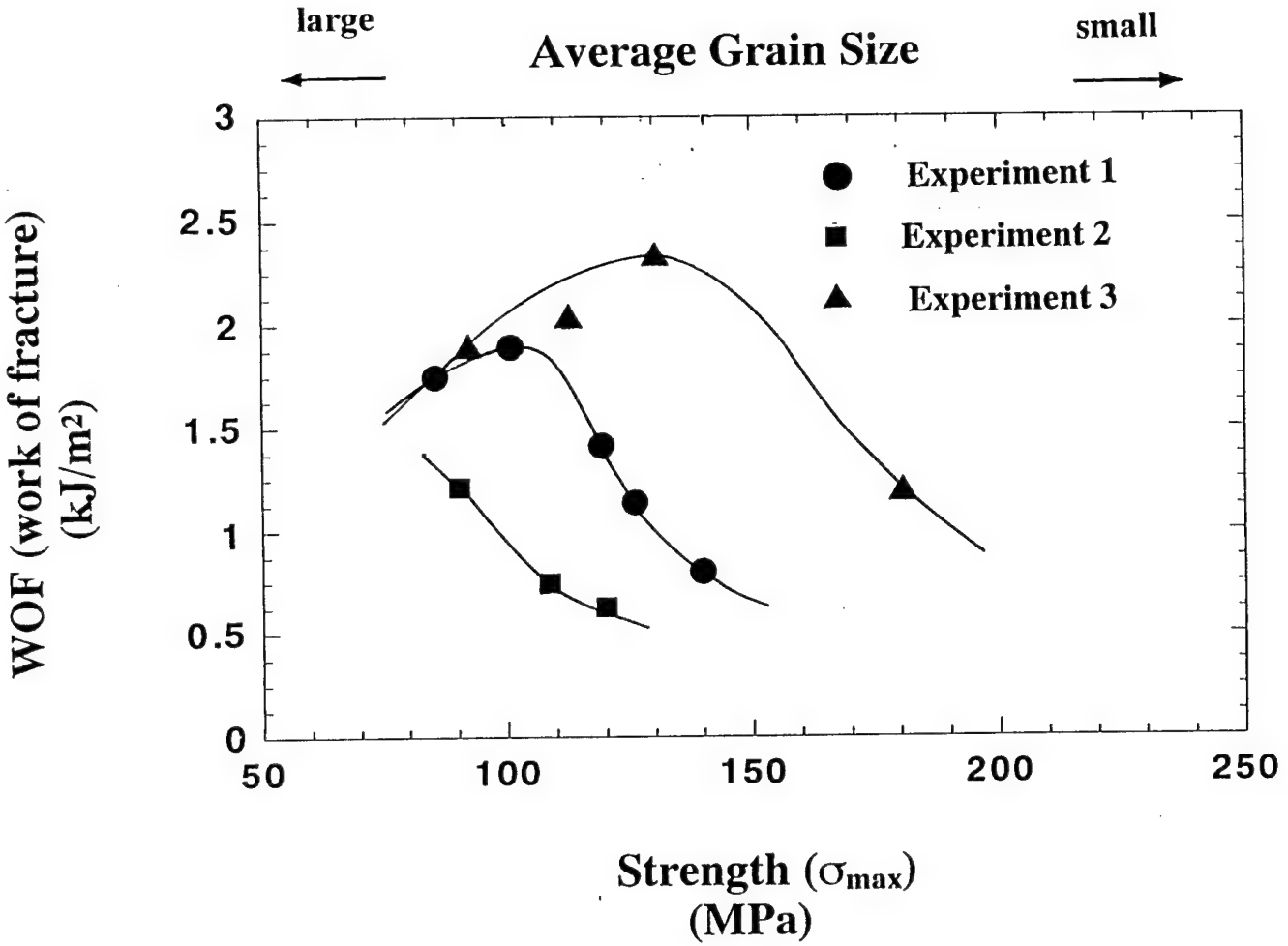
large
Average Grain Size
small
WOF (work of fracture)
(kJ/m²)
3
2.5
2
1.5
1
0.5
0
50
100
150
200
250
Experiment 1
Experiment 2
Experiment 3
Strength (σmax)
(MPa)

Figure 8

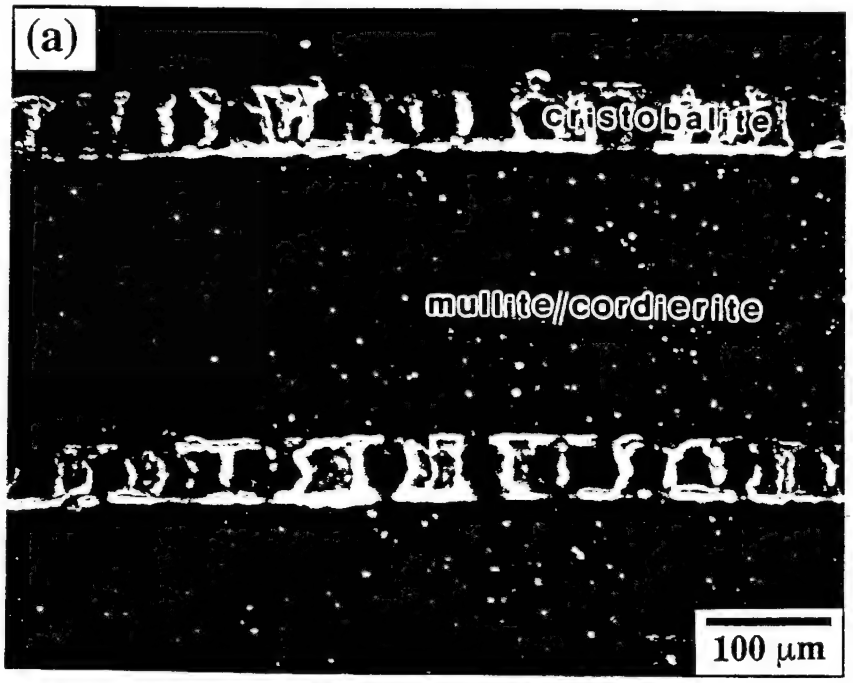

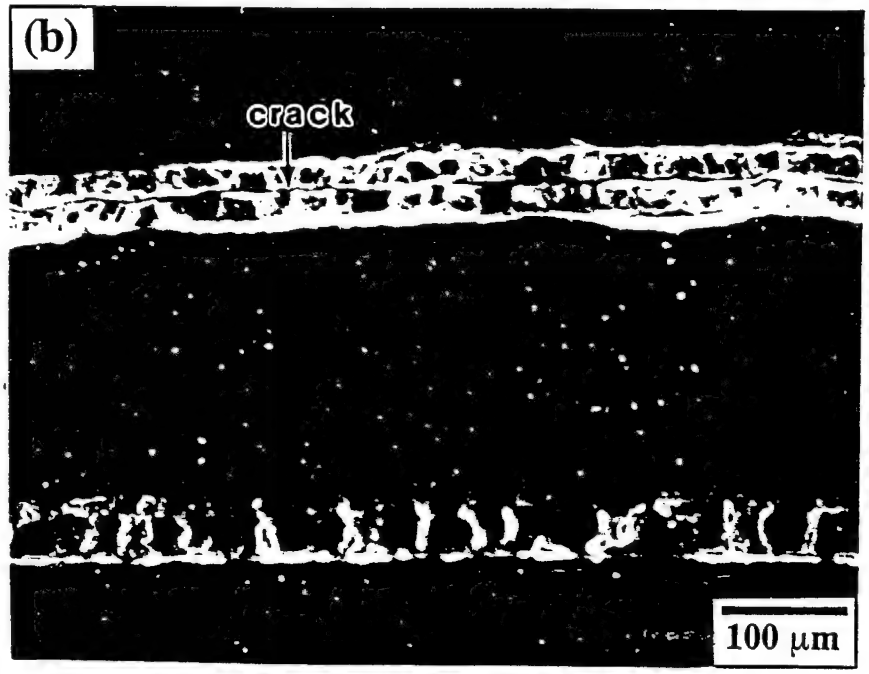

Figure 8a

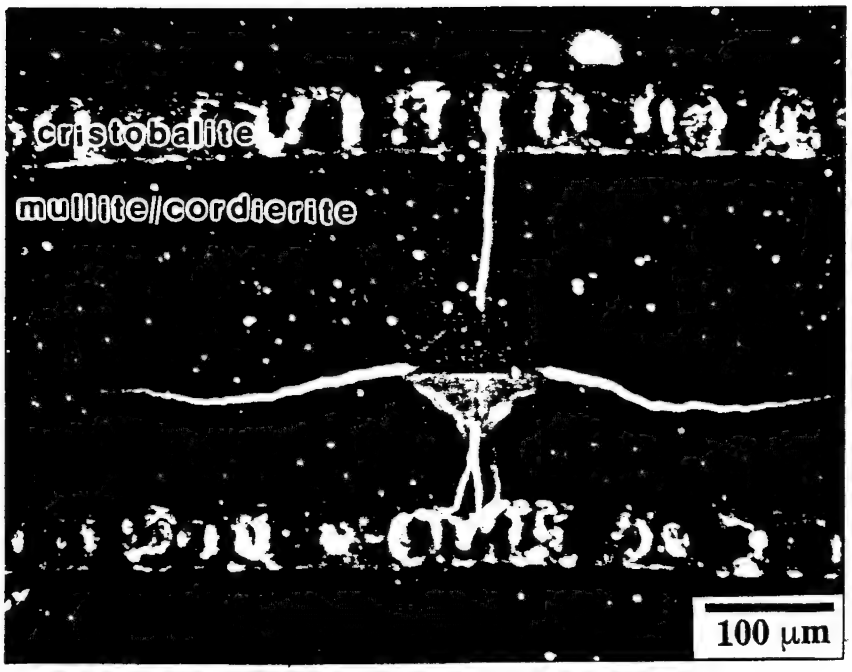

Figure 9/10

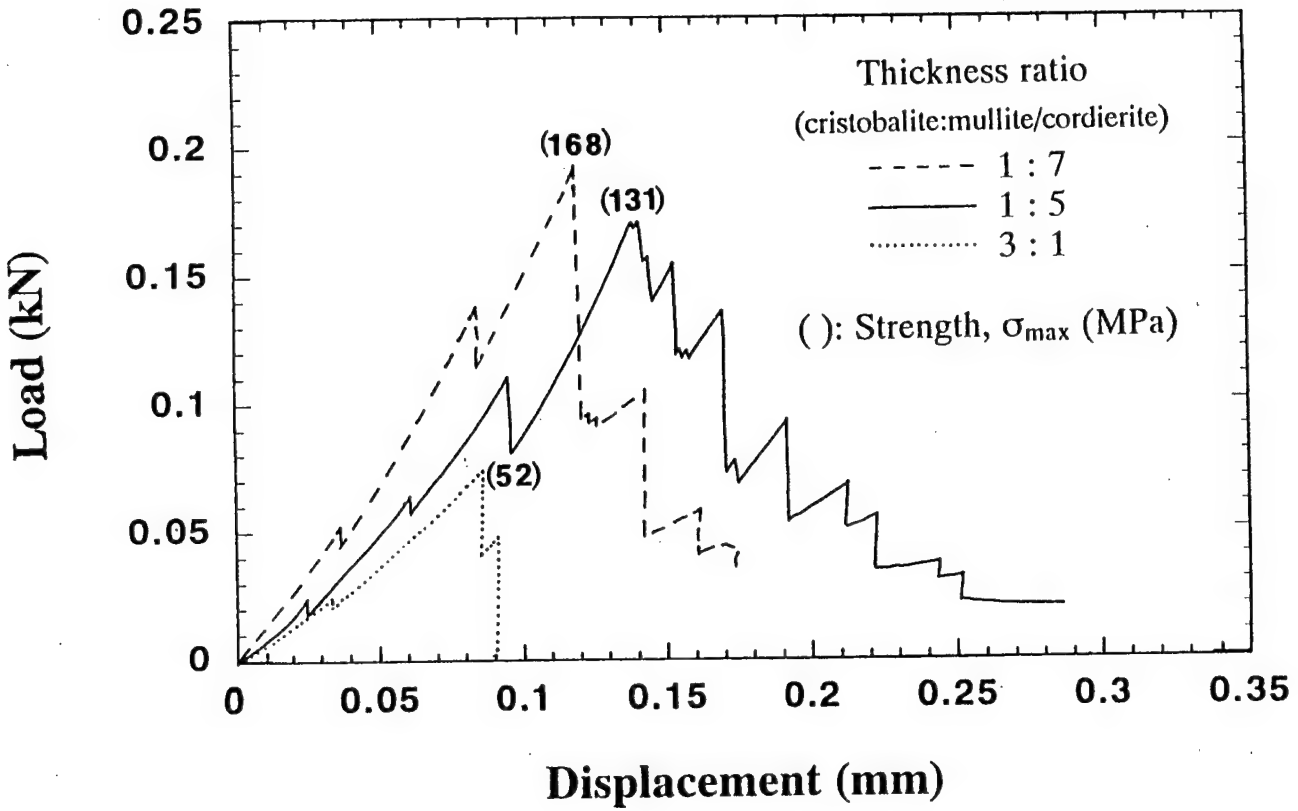
0.25
0.2
0.15
0.1
0.05
0
Load (kN)
0
0.05
0.1
0.15
0.2
0.25
0.3
0.35
Displacement (mm)
Thickness ratio
(cristobalite:mullite/cordierite)
1 : 7
1 : 5
3 : 1
( ): Strength, σmax (MPa)
(168)
(131)
(52)

Figure 10\11

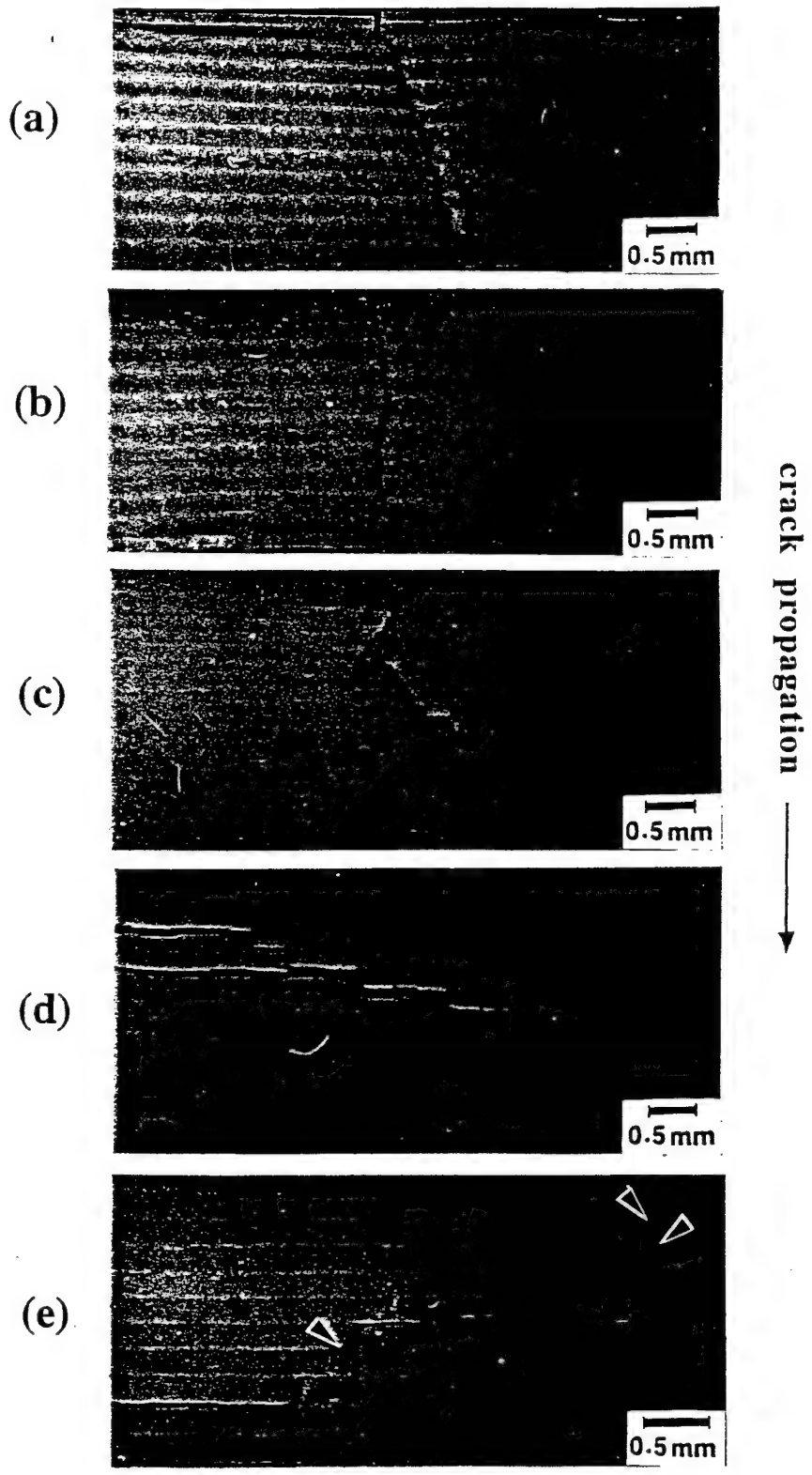

Figure 1/12

Table I. Different Laminate Compositions and Heating Condition for Three Kinds of Mullite/Cordierite Laminates Separated by Cristobalite.

	Experiment 1	Experiment 2	Experiment 3
Composition	60 wt% M/40 wt% C with Ct interphase	C with Ct interphase	60 wt% M/40 wt% C with Ct interphase
Thickness Ratio between †M/§C and ¥Ct	5 : 1	5 : 1	5 : 1
Sintering Condition	Pressureless sintering at 1350 °C for 1 h	Pressureless sintering at 1350 °C for 1 h	Hot pressing at 1200 °C for 1 h
Annealing Temperature	1300 °C	1300 °C	1300 °C

†M : mullite §C : cordierite ¥Ct : β-cristobalite

Table II. Relative Ratio of α/β Cristobalite Phase, Average Grain Size, Strength, and Work of Fracture for Each Experiment at Various Annealing Times.

	Experiment 1				Experiment 2			Experiment 3			
Annealing Time (h)	0	12	30	50	0	12	30	0	10	12	36
† $\frac{I(102)_\alpha}{I(222)_\beta + I(102)_\alpha}$	0.28	0.45	0.60	0.63	0.32	0.49	0.60	0.22	0.47	0.52	0.77
†Average Grain Size (μm)	1.2	3.0	5.0	5.6	1.1	3.0	5.0	0.8	4.2	5.0	7.3
Strength, σ_{max} (MPa)	140	125	100	85	120	108	89	180	131	112	92
Work of Fracture (kJ/m^2)	0.80	1.10	1.93	1.75	0.67	0.75	1.28	1.20	2.38	2.00	1.82

†Reference 15

Table III. Variation of Strength and Work of Fracture as a Function of Thickness Ratio Between Cristobalite and Mullite/Cordierite Layer in Hot-Pressed Laminate Annealed for 10 h.

†Thickness Ratio	1 : 7	1 : 5	1 : 1	3 : 1	5 : 1
Strength, σ_{max} (MPa)	168	131	107	52	48
Work of Fracture(kJ/m^2)	1.90	2.38	1.54	0.41	0.37

†Thickness ratio of cristobalite to mullite/cordierite composite

Polymerized Organic-Inorganic Synthesis of Mixed Oxides

Mehmet A. Gülgün, My H. Nguyen, and Waltraud M. Kriven,
University of Illinois at Urbana-Champaign, 105 S. Goodwin Ave., Urbana, IL 61801, USA

Abstract

A new and simple, chemical route was used to synthesize mixed oxide powders. The method employs long-chain polymers without chelating functional groups as organic "cation carriers". The chemistry of the precursor solution differs from other solution-polymerization techniques. The stabilization of the cations in the precursor is established through the physical entrapment of the metal ions in the network of the dried polymer carrier.

Pure, single phase calcium aluminate ($CaAl_2O_4$), yttrium aluminate ($Y_3Al_5O_{12}$), and yttrium phosphate (YPO_4) powders were produced while maintaining a ratio of 4:1 of positively charged valences of the cations (Me^{n+}) to negatively charged hydroxyl ($-OH^-$) groups. The ceramic yield of the new method is approximately 2, being the weight of the ceramic powders to the weight of the organics used in the preparation.

Introduction

Traditionally, refractory mixed oxide powders are produced by high temperature solid state reactions. However, this route can be very cost ineffective and often leads to a final product with multiple, unwanted phases. Mixed oxide powders thus produced have low surface area and large crystallite size[1].

Various chemical methods have been developed for the synthesis of pure, single phase mixed oxide powders with controlled powder characteristics[2-18]. Even some of these chemical routes tend to result in other phases along with the desired mixed oxide. One of the more successful techniques for single phase mixed oxide

powders is the so-called Pechini process[2], a solution-polymerization route[18]. The basic reactions of this process is schematized in Fig. 1. In general, the process relies on the ability of certain organic acids (alpha pyroxycarboxylic acids to chelate metal ions (step I in Fig. 1)[8,10,11,19]. Then, with the help of polyhydroxyl alcohols, the chelates undergo polyesterification when heated (step II in Fig. 1)[19]. The polyesterification reactions result in a polymerized resin which has the various cations distributed uniformly in stoichiometric proportions. The polymerized resin containing the chelated cations, is the pre-ceramic powder which can then be calcined to obtain the mixed-oxide powder. Since its invention in the 1960's, the Pechini method (and slight variations thereof) has been utilized to produce niobates, titanates, zirconates, chromites, ferrites, manganites, aluminates, cobaltites, and silicates[2-4,11,18]. The synthesis of various calcium aluminate phases by the same method has also been reported earlier[3,4]. For the synthesis of yttrium aluminate garnet phase ($Y_3Al_5O_{12}$, abbreviated as "YAG"), small amounts of dopants need to be used to eliminate discontinuous grain growth[12]. Other methods[13-16] yield the yttrium aluminate perovskite phase ($YAlO_3$) and/or yttrium aluminate monoclinic phase ($Y_4Al_2O_9$, abbreviated as "YAM"), along with YAG.

In general, it is assumed that chelation, or chemical fixation of the cation by the organic molecule is a pre-requisite for a stable, multi-cation precursor. However, in the calcium aluminate system, our previous studies on Pechini precursors with very high metal ion to polymer end group ratios have shown that the precursors were able to support a higher amount of cations than they could chelate[3]. Thus, it is reasonable to suppose that other mechanisms of cation stabilization beside chelation are operative in these organo-metallic precursors. However, there are very few studies on the chemical synthesis of oxide powders via non-chelating organic precursors[20,21].

In order to explore the possibility of synthesizing stable precursors from simpler molecules polyvinyl alcohol (-[CH_2-CHOH]-$_n$, or PVA) and polyethylene glycol (H[O-CH_2-CH_2]-$_n$OH, PEG) were used as polymeric carriers. As seen in Fig. 2 (a), PVA has only hydroxyl (-OH) groups attached to every second C atom in the

carbon backbone of a long-chain molecule. In PEG, (Fig. 2 (b)) there are only two functional groups (also hydroxyl) at the two ends of the polymer. Thus, neither of the organics possesses chemical chelating capabilities. Here, we report on the synthesis of various mixed oxides and phosphates using a relatively simple, long-chain polymer as a carrier for the ceramic precursor. A discussion on a plausible mechanism for cation stabilization by non-chelating polymers is also included.

Experimental procedure:

Throughout this work, nitrate salts (e.g. $Ca(NO_3)_2 \cdot 4H_2O$ (Reagent grade, EM Sci., Gibbstown, NJ), $Al(NO_3)_3 \cdot 9H_2O$ and $Y(NO_3)_3 \cdot 5H_2O$ (Reagent grade Aldrich Chem. Co., Milwaukee, WI)) were used as cation sources. The polymeric precursor for the calcium aluminate was prepared by mixing stoichiometric proportions of the nitrate salts into a 5 wt% aqueous solution of PVA. Solutions were prepared from 100 mol% hydrolized PVA (MW 50000, Aldrich Chem. Co., Milwaukee, WI) and several types of 78 mol% hydrolyzed PVA with different degrees of polymerization (DP), i. e. DP 1700 (KH-17s Gohsenol, from Nippon Gohsel Co., Japan), DP 580 (405-S, from Kuraray Co., Japan) and DP 330 (403-S, from Kuraray Co., Japan). For yttrium aluminates, 78 mol% hydrolized PVA (kH-17s Gohsenol, DP 1700), and nitrate salts of the metals were used. 100 mol% hydrolized PVA solutions were prepared by stirring on a hot plate at 68°C. 78 mol% hydrolized PVA solutions were stirred at room temperature. Phosphoric acid (H_3PO_4, EM Science, Gibbstown, NJ) was used for YPO_4.

The amount of PVA to cation salts (i.e. nitrates) in the solution was adjusted in such a way that there were 4 times more positively charged valences from the cations (Me^{n+}) than negatively charged functional end groups of the organics (in the case of PVA, $-OH^-$ groups). Thus, it was assured that there were more cations in solution than the hydroxyl functional groups of the polymer could chemically bond with. To illustrate the mechanism of stearic entrapment of the cations in the network of entangled polymer in the absence of functional groups, polyethylene glycol (PEG) was used as the polymeric carrier. The concentration of the cations in

the solution, in this case, was adjusted such that for every monomer, there were four positively charged valences in solution. The precursor solutions were then heated on a hot plate until the water of solution evaporated, and a crisp, light brown, aerated gel formed. This gel was ground with an agate mortar and pestle after which it was calcined in air at various temperatures.

The phase formation and precursor to ceramic powder conversion were studied by differential thermal and thermogravimetric analyses (DTA/TGA, (Model STA 409, Netzsch GmbH, Selb, Germany)), and x-ray powder diffractometry (XRD, (DMax Automated Powder diffractometer, Rigaku/USA, Danvers, MA)). Solid state nuclear magnetic resonance (NMR, (home-built spectrometer based on a Nicolet 1280 data-acquisition system)) and Fourier transform infrared (FTIR, (Nicolet)) spectrometries were used to gain information about the structure and chemistry of precursors as well as amorphous and crystalline powders. Raman spectroscopy of YAG powders was performed using a micro-raman spectrometer (Jobin Yvon T64000). Surface area measurements were made by five-point BET analysis (Micromeritics Model ASAP 2400, Micromeritics, Norcross, GA), and the particle size was studied using a LASER absorption spectrometer (Micromeritics Sedigraph Model 5000E, Micromeritics, Norcross, GA). Selected powders were examined by scanning electron (SEM, (ISI DS-130, International Scientific Instruments, Santa Clara, CA)) and transmission electron microscopy (TEM, (CM 12, Philips Instruments, Inc., Mahwah, NJ)). A more detailed description of chemical synthesis and characterization of the powders has been reported earlier[19,22].

III. Results

During precursor processing (<300°C), no precipitation from the solution was observed, although a high ratio of metal ion to hydroxylic end groups in PVA containing solutions, or ether oxygen in the case of PEG containing solutions were used. Stable, crisp precursor powders with cations in the desired stoichiometric proportions were obtained.

TG/DT analysis of the precursors showed that most of the organics and other volatiles (H_2O, NO_x et c.) were burnt off below 650°C in calcium aluminate system

(Fig. 3 a), and below 900°C in yttrium aluminate system. (Fig. 3 b). The strong endotherm below 300°C and the corresponding weight loss indicated evaporation of water from the precursors. Complex decomposition reactions of the organics occurred between 300°C and 800°C in several steps. A slight, additional weight loss (~2 wt%) occurred above 900°C in the calcium aluminate and yttrium aluminate systems.

Pure, fine and amorphous powders were obtained at temperatures as low as 650°C. Corresponding crystalline powders, i.e $CaAl_2O_4$, $Y_3Al_5O_{12}$ or YPO_4, were produced when precursors were calcined at 900°C for about an hour (Fig. 4 (a) and (b)). The powders thus prepared were single phase and pure as determined by XRD. Precursors that used PEG instead of PVA as their polymeric "carrier" exhibited a similar behavior. Crystalline, single phase powders in desired stoichiometries were formed at 900°C.

FTIR and NMR studies of the powders calcined at various temperatures between 500°C and 900°C were performed in order to gain more insight into the structure and composition of the amorphous powders, and to characterize the gel-to-ceramic conversion. Fig. 5 shows a portion of a typical FTIR spectrum from the powders calcined at 600°C and 800°C for an hour. IR study revealed absorption bands at 1421 and 1493 cm^{-1} that are usually associated with carbon-oxygen stretching in inorganic carbonates. A Raman spectrum of the YAG precursors showed a band at 1051 cm^{-1} which is typical of carbonates.

Along with the precursor gels that contained the cations, a "bare" PVA gel and 78 % hydrolized PVA powders were studied by FTIR and NMR spectroscopies before calcination. The "bare" PVA gel solution had been subjected to the same procedures as the precursors with the cations. However, it did not had the cation salts in its composition. Fig. 6 shows the FTIR spectra from pure 78% hydrolyzed PVA powders (a), a "bare" PVA gel (b), and a YAG precursor (c). PVA powder and the gel show more or less the same spectra. Besides the bands associated with CH_2, CH_3, and OH groups, the bands due to the acetate groups are observable in the spectra. The spectrum from YAG precursors appeared rather different than the one from the "bare" gel (Fig. 6(c)). The major discrepancies occurred in regions from

1000 to 1700 cm^{-1} and 2700 to 3700 cm^{-1}. There are strong shifts in the bands associated with the acetate groups (1600 to 1800 cm^{-1}), and in bands corresponding to hydroxyl groups (3000 to 3700 cm^{-1}). An additional peculiar change between the spectra was the disappearance of the absorption bands due to CH_2 and CH_3 stretchings at 2700 to 3000 cm^{-1} (arrowed in Fig. 6 (c)).

The NMR spectra from PVA powders and YAG precursors before calcination revealed similar differences. The spectrum from PVA powders showed strong peaks associated with methyl (12.5 ppm) and methylene (44 ppm) carbons along with the peak for the carbonyl carbon at 170 ppm[23]. On the other hand, the spectrum from YAG precursor had a strong peak at 170 ppm, a broad hump between 100 and 150 ppm, and a small peak at 20 ppm. Peaks due to methylene carbon were very weak.

Fig. 7 presents a series of ^{27}Al-NMR analyses from calcium aluminate powders calcined at temperatures 500 -900°C. Three distinct peaks at 10, 40 and 75 ppm were detected at low temperatures. As the calcination temperature was raised above 550°C the peak at 40 ppm disappeared. However the peak at 10 ppm was detected up to 700°C. The peak at 75 ppm progressively became sharper with increasing calcination temperature and shifted to 80 ppm at 900°C.

When calcined at low temperatures (i.e. 650 to 800°C), the powders prepared via this new method had a BET specific surface area of about 12 m^2/g. Electron microscopic studies (SEM, TEM) of the powders revealed that most of the surface area was due to the interconnected, internal porosity. (Fig. 8 (a) and (b)). The particles were agglomerates of smaller primary particles approximately 50 to 100 nm in size. The morphology of the agglomerates was closely related to the chain length of the polymeric carrier, i.e. PVA[19,22]. Smaller molecular weight PVA resulted in round hollow agglomerates, whereas longer PVA chains yielded star-shaped, dendritic agglomerates.

IV. Discussion

A polymerized organic-inorganic route employing simple, long-chain polymers as the carrier organic phase is a viable, inexpensive technique for producing mixed oxide powders. These simple polymer chains have no special chelating end groups, in contrast to the alpha pyroxycarboxylic acids of the so-called Pechini precursor. The technique has a ceramic to polymer yield of close to or above 2.0, being the weight ratio of the ceramic powders to the organics used in the preparation, as compared to 0.15 for the Pechini method[24].

Since there are no chelating organics in the solution, the choice of the cation sources becomes critical for the success of the process, especially as the number of cations in the mixed oxide increases. An important criterion in the selection of the cation sources is the aqueous solubility of the appropriate salts. All salts used in this study have very high solubility in cold water[25]. Nitrates are the most suitable, commercially available sources of cations at the present time. Less soluble salts cause phase inhomogeneities in the final product due to precipitation during precursor formation. Nitrates have an additional advantage of being strong oxidizing agents, and thus, facilitating the pyrolysis of the organics. This, in turn, helps in reducing the amount of carbonates formed. The formation of carbonates may cause disproportionation of the cations in the precursor, and hence, may lead to unwanted phases[22]. In the cases of calcium aluminate, yttrium aluminate and yttrium phosphate no precipitation from aqueous solution was observed during processing. Hence, no disproportionation of the cations from the desired stoichiometry was expected. As the x-ray studies showed, firstly uniform, amorphous powders were obtained at low temperatures. As the temperature was raised to above 900°C crystalline powders of the corresponding stoichiometries were produced.

FTIR analyses of the powders calcined at lower temperatures (e.g. at 600°C and 800°C) revealed a duplet around 1400 to 1500 cm^{-1}. This is the wavenumber region where carbonates usually have their absorption band. However, the existence of a dublet instead of a single band, as well as absence of any crystalline peak in the x-ray spectra were indicative of amorphous compounds. The Raman studies of similar powders detected bands associated with carbonates. ^{27}Al NMR studies conducted with a calcium aluminate precursor calcined at lower temperatures showed that Al

was involved in more than one type of configuration in these powders. The peaks at 10, 40 and 75 ppm could be assigned to six, five and four-fold coordination of the Al atom, respectively[26]. Al is in four-old coordination in Al-O tetrahedra of $CaAl_2O_4$ and $CaAl_4O_7$[27]. Thus, the existence of a small amount of six-fold coordinated aluminum along with the FTIR and Raman results indicated that powders calcined at temperatures lower than 900°C contained amorphous carbonate-like compounds. The amount of this compound decreased as the calcination temperature was raised, as observed in the weakening of the absorption band in the FTIR spectra (Fig. 5).

Vibrational spectroscopy analyses (FTIR and NMR) of "bare" PVA gel and the precursors revealed important clues with respect to the formation of a stable precursor, and the precursor-to-mixed oxide ceramic conversion. The disappearance of the bands due to CH_2 and CH_3 stretchings in 2700 to 3000 cm^{-1} region and the corresponding decrease in the intensity of NMR peaks for methyl and methylene carbon were probably due to the degradation of PVA in the presence of a strong oxidizing agent, i.e. NO_3^- . The shifts in the absorption bands associated with the acetate groups (1600 to 1800 cm^{-1}) indicated that some metal ions were chelated by the carboxylic end groups of the acetates and were chemically bound in the polymer structure. This type of metal ion stabilization mechanism is known to operate in so-called Pechini-resins[18]. There were only a small amount (35%) of acetate groups in 78 % hydrolized PVA, and this mechanism alone cannot accommodate all the cations in precursor solutions.

A second strong change between the spectra of the PVA gel and the ceramic precursor was associated with the hydroxyl groups of PVA. The OH bands (300 to 3700 cm^{-1}) were skewed towards higher wavenumbers indicating interactions with the metal ions, and perhaps a stronger ordering in the precursors. Thus, some of the metal ions in solution were tied up with the hydroxyl groups of the polymer. However, as stated earlier, there were more e cations in the precursor solutions than there were functional groups (i.e. hydroxyl and acetate groups) in the polymer. Since no precipitation during precursor processing was observed the cations had to be stabilized in the structure of the polymer by means other than mere chemical linking.

The following scheme is proposed for physical entrapment of cations in the network structure of polymers with no chelating end groups:

In aqueous solution of PVA many metal can be stabilized at the polymer by the interactions with the hydroxyl groups. However, there are still cations left in solution that do not have a direct link to hydroxyl groups. These „floating" metal ions are localized around the polymer by the bridging action of the water molecules between the metal ions linked to the hydroxyl groups and the free floating metal ions, as depicted in Fig. 9. As most of the water of solution is evaporated during precursor processing, the polymer chains come closer to each other, and the viscosity of the solution increases. The free space between the polymer molecules shrinks and chain entanglement causes a close polymer. At this stage, the mobility of the cations is greatly reduced, and the small amount of water left in the precursor is enough to keep all the cations in the entangled polymer network. Hence, there is no precipitation to cause off-stoichiometry. Thus, stable precursors are obtained.

Experiments with polyethylene glycol as the polymeric carrier in the pre-ceramic gels confirmed the observations made with the PVA based precursors. Chemical synthesis of mixed oxide powders via the system containing PEG as the carrier will be elaborated upon in a further communication[28].

The results of this study indicate that the metal ions in the organic precursor can be physically stabilized within an entangled polymer network. Thus, "cation chelation" by the carboxylic end groups, as in the Pechini resin, is not a necessary route to stable ceramic precursors. Previous results from Pechini precursors with very high metal ion to polymer end group ratios have shown that the resin was able to support a higher amount of cations than it could chelate[3]. The new synthesis method differs from solution polymerization techniques, such as the Pechini process and its many derivatives, in two aspects: (i) The organic phase is a long chain, and so does not require polyhydroxyl alcohols (such as ethylene glycol) to promote polymerization. ii) The polymer does not have a chelating functional group. Therefore, chelation, which is regarded as a prerequisite in the Pechini type processes, is not the main operating mechanism for a stable precursor in this method. In this study, the precursor had a ratio of 4:1 of positively charged valence from cations to negatively charged functional groups. Despite this large charge imbalance, no

precipitation from solution was observed. This was also closely related to the very high aqueous solubility of the nitrate salts of calcium, yttrium, and aluminum. Further investigation on the synthesis of various calcium silicates is underway to study mixed oxide systems whose precursor salts are less soluble in water than the ones reported here.

V. Conclusions

A polymerized organic-inorganic complex route was successfully employed to synthesize various monophase, fine and pure mixed oxide powders. The new technique uses simple long-chain polymers like polyvinyl alcohol (-[CH_2-CHOH]-$_n$, PVA) or polyethylene glycol (H[O-CH_2-CH_2]-$_n$OH, PEG) as the "organic carrier" for the pre-ceramic gel. The results show that "metal ion chelation" of the solution polymerization method is not the only mechanism to obtain molecularly homogeneous, stable precursors for complex mixed oxide powders. The cations of the mixed oxide are stearically entrapped in the entangled network of the organic polymers. An important criterion for the selection of the cation sources is the aqueous solubility of the corresponding metal salts. The more soluble the salts, the higher is the yield of the new process.

VI. Acknowledgments

The authors gratefully acknowledge use of the equipment in the Center for Microanalysis of Materials at the Frederick Seitz Materials Research Laboratory at the University of Illinois in Urbana-Champaign. We are thankful to Professor J. Kirkpatrick of the Department of Geology at UIUC for the use of the NMR facilities, and to Professor M. Yoshimura of the Research Laboratory for Engineering Materials at Tokyo Institute of Technology for the use of the Raman spectroscopy facilities. M.A.G. gratefully acknowledges very useful discussions on interpretation of the FTIR results with Profs. M. Yoshimura, M. Kakihana of the Tokyo Institute of Technology, and Prof. J-H. Choy of the Seoul National University.

VII. References

1 K. Fujii, W. Kondo, and H. Ueno, "Kinetics of Hydration of Monocalcium Aluminate," *J. Am. Ceram. Soc.*, **69** [4] 361-364 (1996).

2 M. P. Pechini, *Method of Preparing Lead and Alkaline Earth Titanates and Niobates and Coating Method Using the Same to Form a Capacitor*, U. S. Patent No. 3,330,697, U.S. Patent Office, 1967.

3 M. A. Gulgun, O. O. Popoola, and W. M. Kriven, "Chemical Synthesis and Characterization of Calcium Aluminate Powders," *J. Am. Ceram. Soc.*, **77** [2] 531-539 (1994).

4 M. A. Gulgun, O. O. Popoola, I. Nettleship, W. M. Kriven, and J. F. Young, "Preparation and Hydration Behavior of Pure $CaAl_2O_4$"; pp. in *Proceedings of the Materials Research Society Symposium*, , Vol. 245. Edited by e. a. F. P. Glasser. Materials Research Society, Pittsburgh, Boston, MA, 1992.

5 L. W. Tai and P. A. Lessing, "Modified Resin-Intermediate Processing of Perovskite Powders: Part I. Optimization of Polymeric Precursors," *J. Mater. Res.*, **7** [2] 502-510 (1992).

6 L. W. Tai and P. A. Lessing, "Modified Resin-Intermediate Processing of Perovskite Powders: Part II. Processing for Fine, Nonagglomerated Sr-Doped Lanthanum Chromite Powders," *J. Mater. Res.*, **7** [2] 511-519 (1992).

7 S. C. Zhang, G. L. Messing, W. Huebner, and M. M. Coleman, "Synthesis of YBa2Cu3O7-x Fibers from an Organic Acid," *J. Mater. Res.*, **5** [9] 1806-1812 (1990).

8 P. A. Lessing, "Mixed-Cation Oxide Powders via Polymeric Precursors," *Am. Ceram. Bull.*, **68** [5] 1002-1007 (1989).

9 L.-W. Tai, H. U. Anderson, and P. A. Lessing, "Mixed-Cation Oxide Powders via Resin Intermediates Derived from a Water Soluble Polymer," *J. Am. Ceram. Soc.*, **75** [12] 3490-3494 (1992).

10 H. U. Anderson, M. J. Pennell, and J. P. Guha, "Polymeric Synthesis of Lead Magnesium Niobate Powders"; pp. in 1987.

11 N. G. Eror and H. U. Anderson, *Polymeric Synthesis of Ceramic Materials*. pp. 571. Vol. 73, Materials Research Society, Pittburgh, PA, 1986.

12 G. De With, "Preparation, Microstructure and Properties of $Y_3Al_5O_{12}$ Ceramics," *Philips J. Res.*, **42** 119-130 (1987).

13 D. R. Messier and G. E. Gazza, "Synthesis of $MgAl_2O_4$ and by Thermal Decomposition of Hydrated Nitrate Mixtures," *Am. Ceram. Soc. Bull.*, **51** [9] 692-697 (1972).

14 L. P. Morozova, E. S. Lukin, T. V. Efimovskaya, A. V. Smolya, and I. F. Panteleeva, "Synthesis of Aluminum Yttrium Garnet," *Glass Ceram.*, **35** 158 (1978).

15 D. J. Sordlet, "Synthesis of Yttrium Aluminum Garnet Precursor Powder by Homogeneous Precipitation," *J. Eur. Ceram. Soc.*, **14** 123-130 (1994).

16 D. M. Roy, R. R. Neurgaonkar, T. P. O'Holleran, and R. Roy, "Preparation of Fine Oxide Powders by Evaporative Decomposition of Solutions," *Am. Ceram. Soc. Bull.*, **56** [11] 1023-1024 (1977).

17 I. Nettleship, J. L. Shull, and W. M. Kriven, "Chemical Preparation and Phase Stabilty of $CaSiO_4$ and $SrSiO_4$ Powders," *J. Eur. Ceram. Soc.*, **11** 291-298 (1993).

18 M. Kakihana, M. Arima, M. Yashima, M. Yoshimura, H. Mazaki, and H. Yasuoka, "Chemical Design for Functional Multi-Component Oxides by Polymerized Complex Method"; pp. in *Advanced Materials '93, I/A: Ceramics, Powders, Corrosion and Advanced Processing*, Vol. 14a. Edited by N. M. e. al. Elsevier Science, 1994.

19 M. A. Gulgun and W. M. Kriven, "A Simple Solution-Polymerization Route for Oxide Powder Synthesis"; pp. 57-66 in *Ceramic Transactions*, Vol. 62. Edited by J. J. Kingsley, C. H. Schilling, and J. H. Adair. American Ceramics Society, Westerville, 1995.

20 P. Pramanik and A. Pathak, "A New Chemical Route for the Preparation of Fine Ferrite Powders," *Mater. Sci. Bull.*, **17** [6] 967-975 (1994).

21 S. K. Saha, S. Pathak, and P. Pramanik, "Low-Temperature Preparation of Fine Particles of Mixed Oxide Systems," *J. Mater. Sci. Lett.*, **14** 35-37 (1995).

22 M. A. Gulgun, Ph. D. Thesis, University of Illinois, Urbana-Champaign, 1996.

23 M. H. Nguyen, Masters Thesis, University of Illinois, Urbana-Champaign, 1997.

24 B. Johnson, Master of Science Thesis, University of Illinois at Urbana-Champaign, 1996.

25 *CRC Handbook of Chemistry and Physics* Edited by R. W. Weast. CRC Press Inc., 1988.

26 X. Cong and R. J. Kirkpatrick, "Hydration of Calcium Aluminate Cements: A solid -State 27Al NMR Study," *J. Am. Ceram. Soc.*, **76** [2] 409-416 (1993).

27 V. I. Yakerson, V. D. Nissenbaum, E. Z. Golosman, and V. M. Mastikhin, "High Resolution NMR study of Calcium Aluminate Catalysts," *Kinetika i Kataliz*, 27 [6] 1419-26 (1986).

28 M. H. Nguyen and W. M. Kriven, "A Stearic Entrapping Polymer Route to Mixed Oxide Ceramics," *in preparation*, (1997).

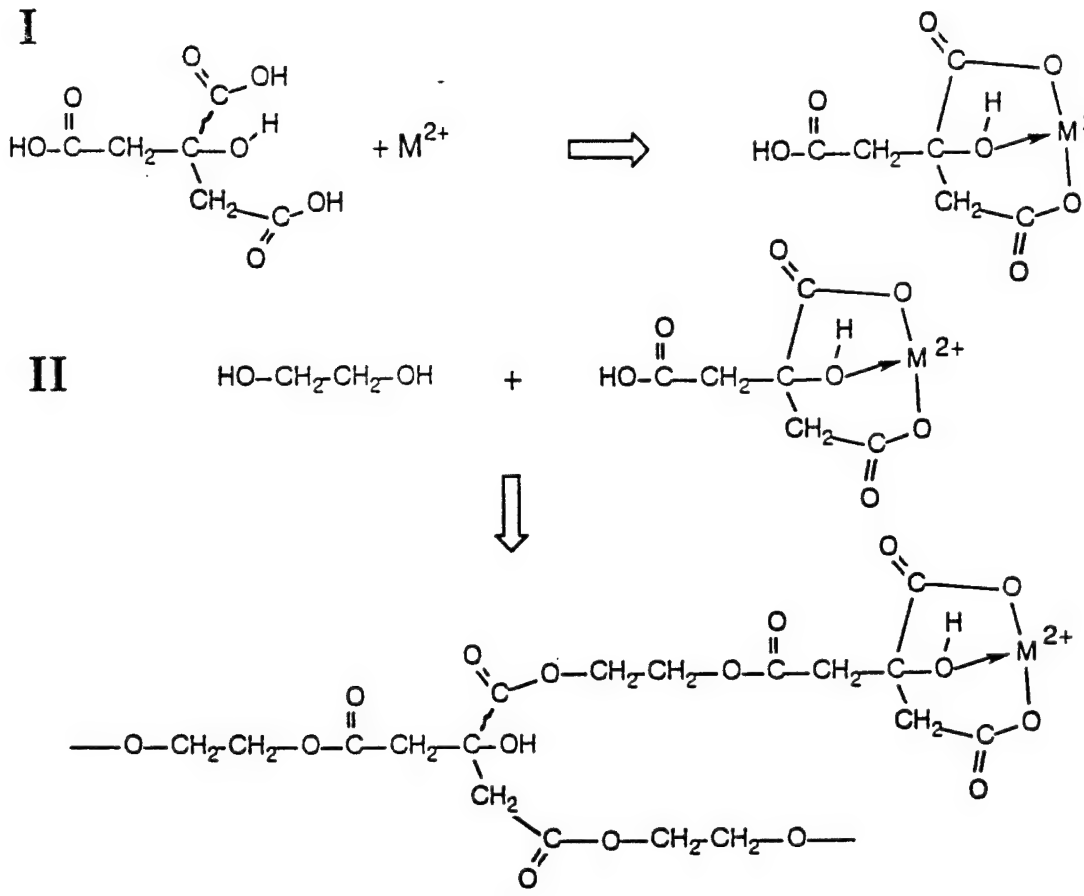

Fig. 1. Schematic illustrating the basic reactions of the Pechini process.

(a)

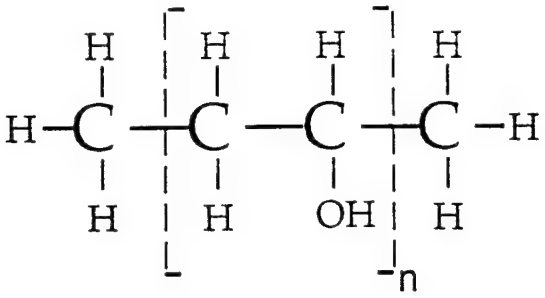

Polyvinyl alcohol, PVA

(b)

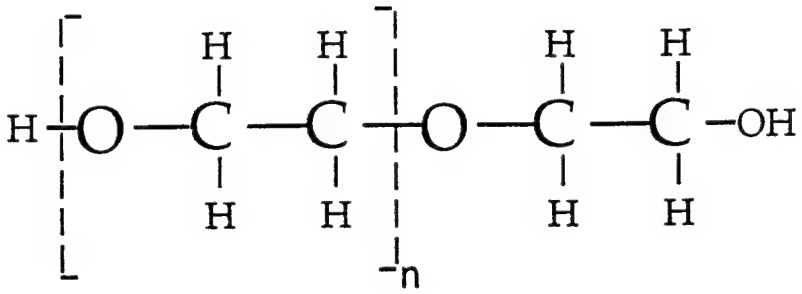

Polyethylene glycol, PEG

Fig. 2. Schematic of the polyvinyl alcohol (PVA) and polyethylene glycol (PEG) molecules.

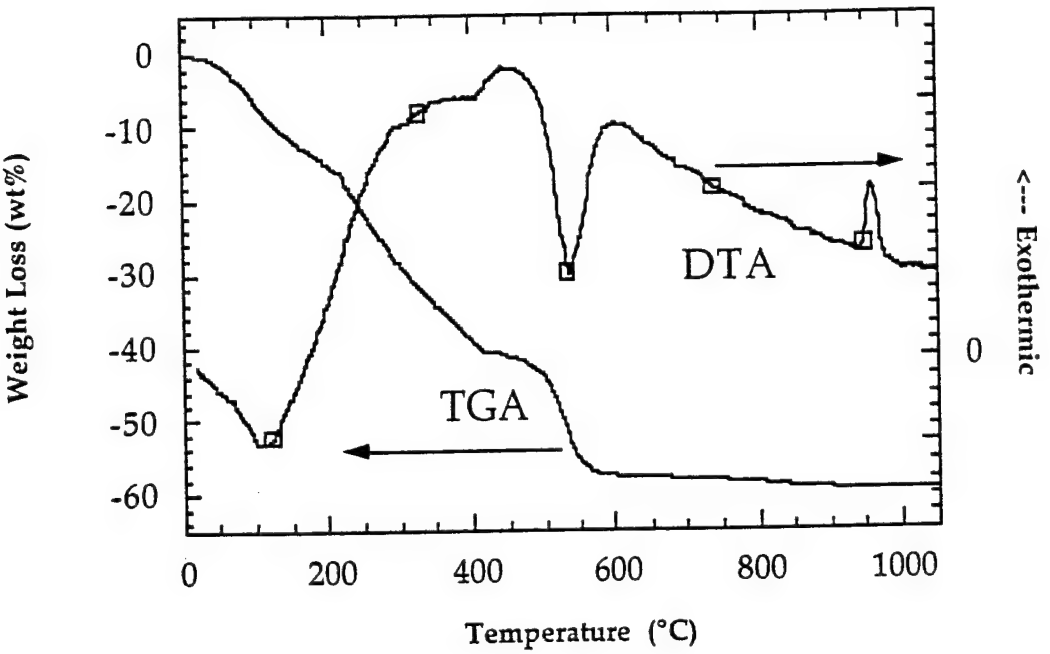

Fig. (a). DTA/TGA plot of the PVA based precursor for calcium aluminate powders.

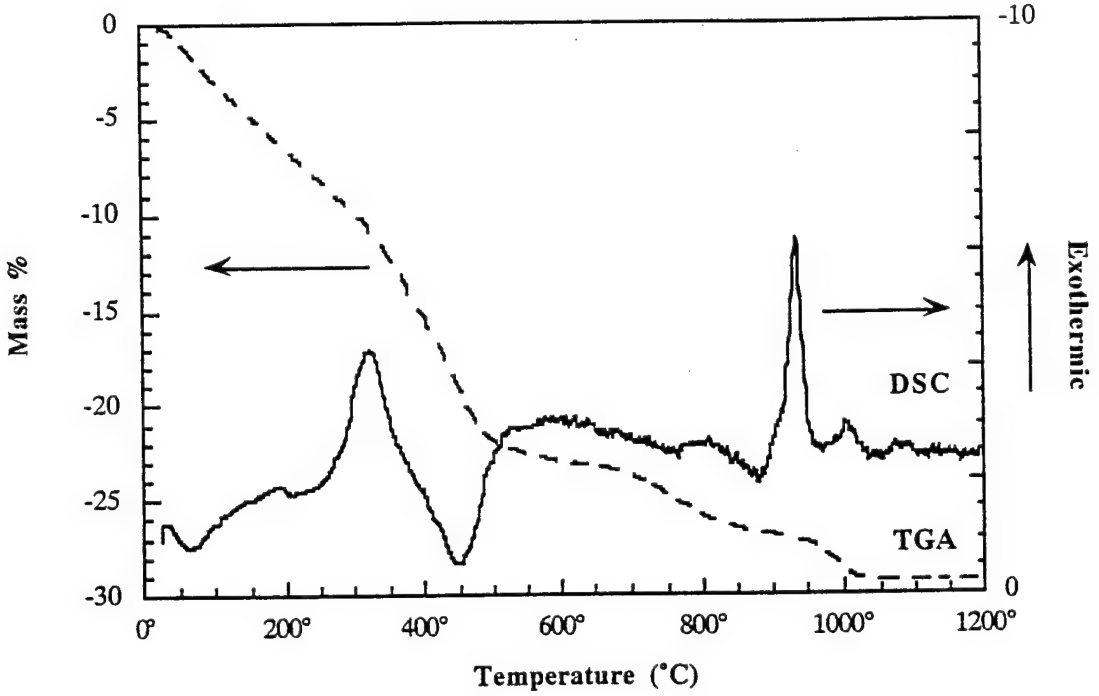

Fig. (b). DSC/TGA plot of PVA based precursor for YAG powders.

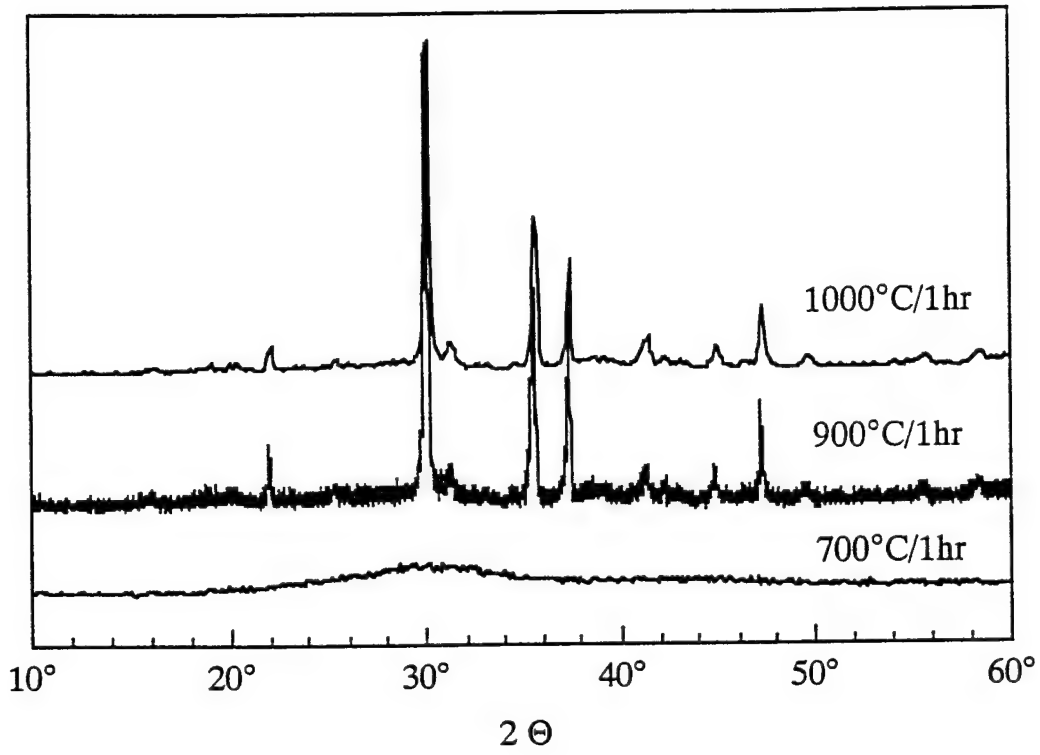

Fig. (a). X-ray spectra of calcium aluminate powders calcined at various temperatures.

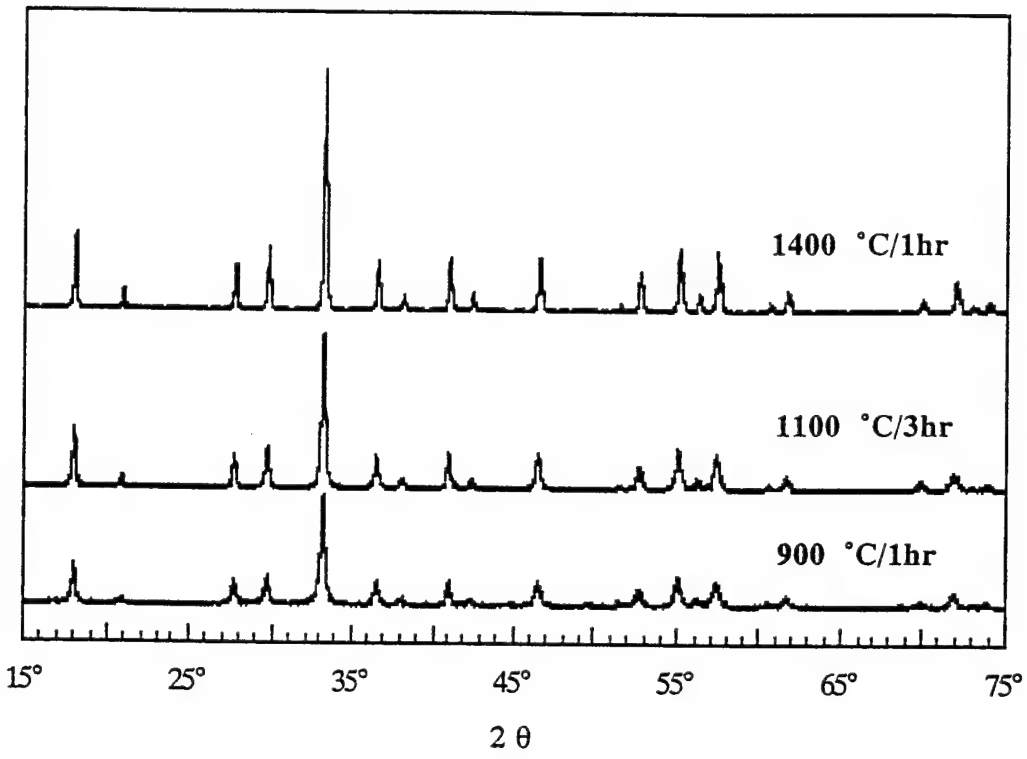

Fig. (b). X-ray spectra for YAG powders calcined at various temperatures.

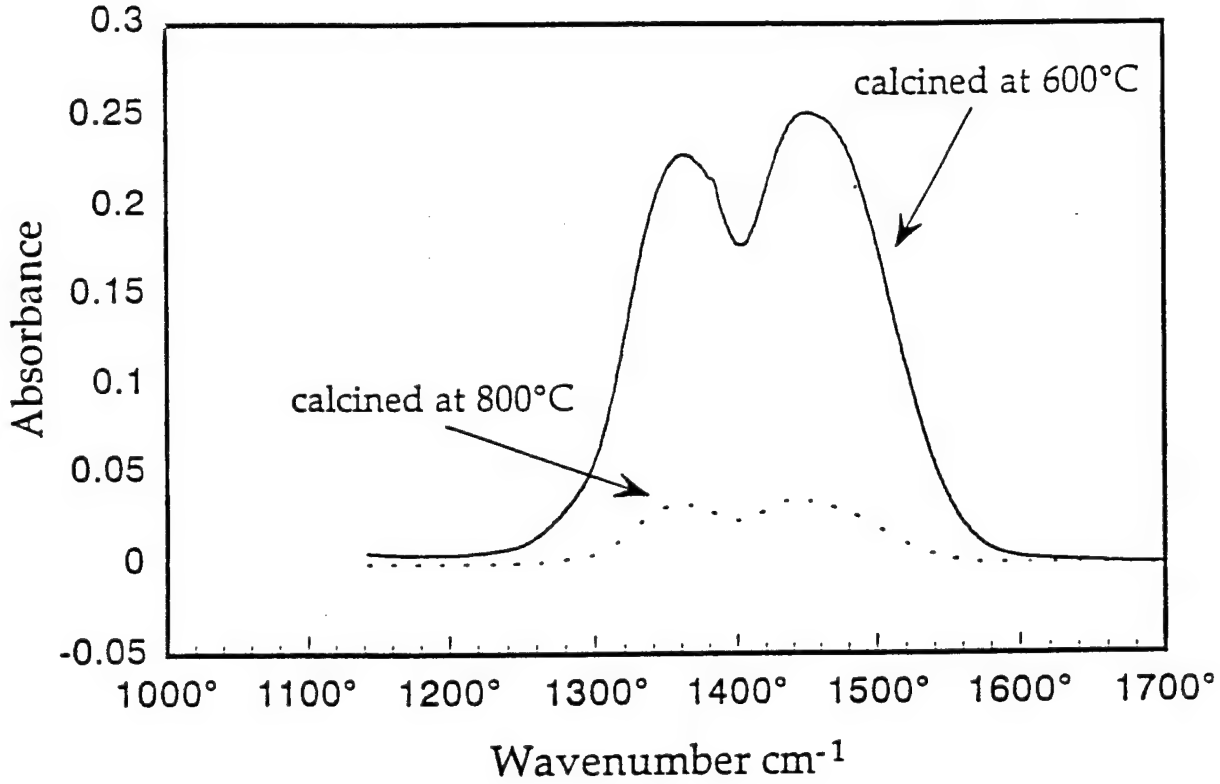

Fig. 5. FTIR spectra of calcium aluminate powders calcines at two different temperatures.

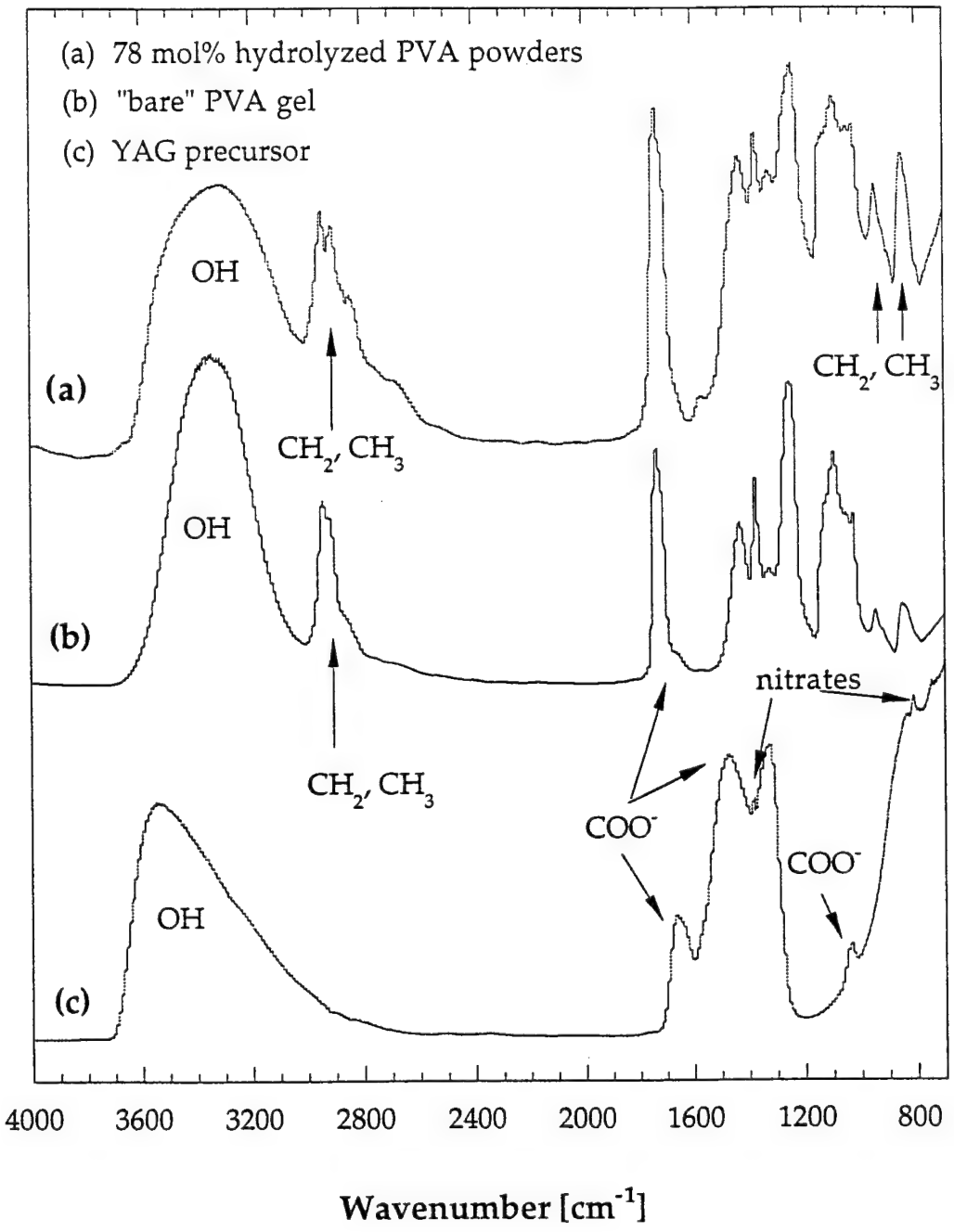

Fig. 6. FTIR spectra from pure 78 mol% hydrolyzed PVA powders (a), "bare" PVA gel (b), and YAG precursor (c).

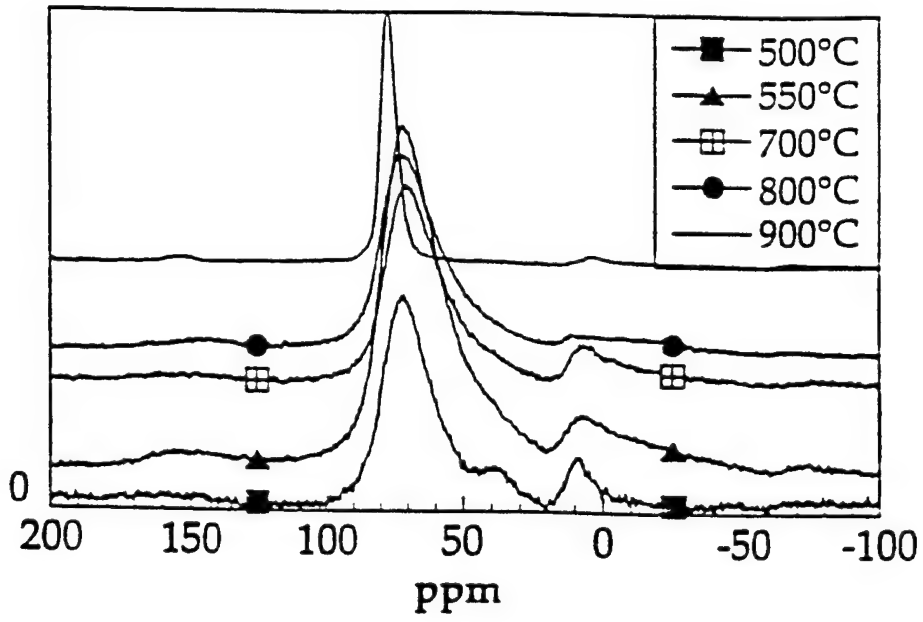

Fig. 7. 27 Al NMR spectra of calcium aluminate powders calcined at temperatures between 500 and 900°C.

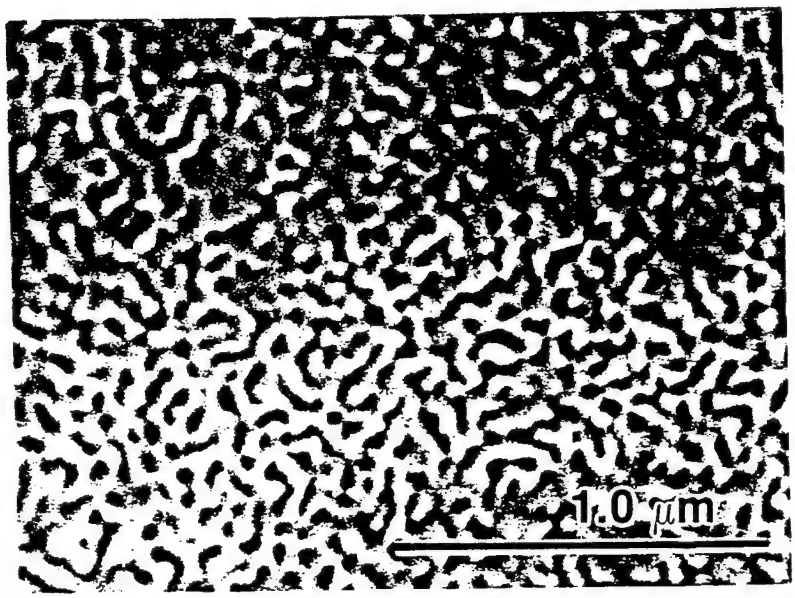

Fig. 8 (a) SEM micrograph of YAG powders showing high amount of internal porosity (courtesy of Dr. J. L. Shull)

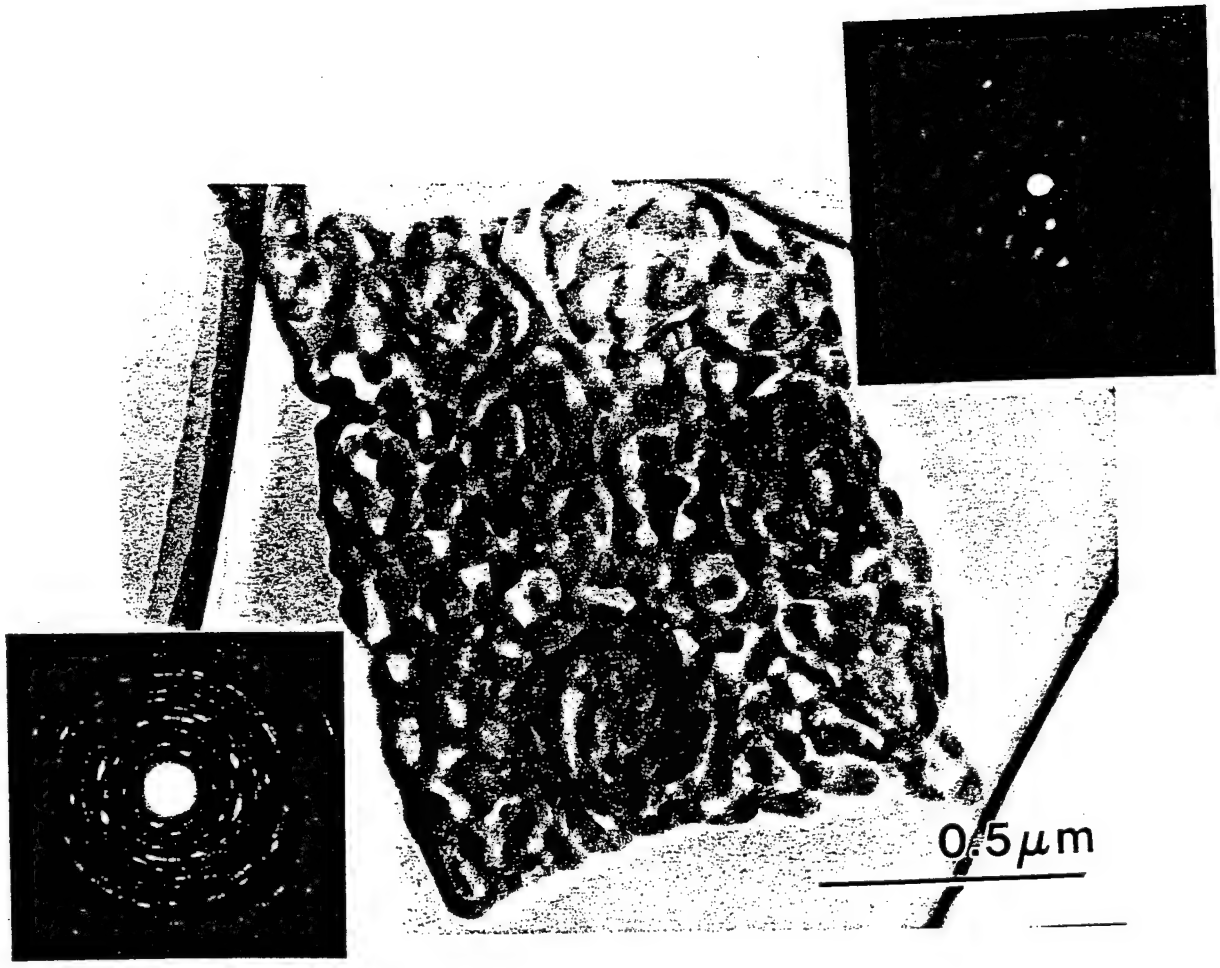

Fig. 8 (b) TEM micrograph of YAG powders showing a porous particle.

Nano-Size, Amorphous Cordierite Powder Prepared by a Solution-Polymerization Route

Sang-Jin Lee* and Waltraud M. Kriven*

Department of Materials Science and Engineering, University of Illinois at Urbana-Champaign, Urbana, Illinois 61801, USA

Abstract

A nano-size, amorphous-type cordierite ($2MgO{\cdot}2Al_2O_3{\cdot}5SiO_2$) powder was made by attrition milling a calcined precursor which was prepared by a solution-polymerization route. A Pechini resin and a PVA solution were used in the solution-polymerization process as the organic carriers. In case of the cordierite prepared using PVA solution, the maximum densification was achieved much earlier than in the case of the Pechini resin process. The densification process of the amorphous cordierite was a viscous-flow sintering type and depended on the amount of amorphous silica. The densification was inhibited by the crystallization of silica in both cases and it was the reason for the coarse microstructure of the sintered cordierite. Sintered cordierite did not show the presence of any amorphous silica phase as was observed in the case of the solution-polymerization route employing PVA solution.

The cordierite having a dense microstructure and a thermal expansion coefficient of $2.2 \times 10^{-6}/°C$, was synthesized from nano-size particles prepared by attrition milling. Effective attrition milling was possible in less than an hour.

* Member, The American Ceramic Society.

I. Introduction

Cordierite ceramics have intrinsic low thermal expansion coefficients, dielectric constant and density, coupled with high chemical and thermal stability. Therefore, cordierite ceramics are expected to be used as heat exchangers for gas turbine engines, industrial furnaces and integrated circuit substrates.[1-3] However, it has been impossible to sinter pure cordierite without any sintering aid because of the narrow sintering range near the incongruent melting point of cordierite.[4] Addition of sintering aids such as K_2O or TiO_2, which increased the density from less than 90 % to 98 % of theoretical, resulted in a large thermal expansion, an increase of dielectric constant and a decrease in crystallization temperature.[5-7] The preparation of homogeneous and fine, reactive cordierite powder which can be sintered without the addition of impurity, therefore, is considered to be indispensable.

It is well known that alkoxy-derived gel powders are very fine and reactive.[8] However, in multi-component systems such as cordierite ceramics, the difference in hydrolysis rates of each alkoxide caused inhomogeneity in the resultant oxides.[9] Yoldas[10] demonstrated that the degree of hydrolysis of alkoxides could be controlled by the hydrolysis temperature, types of catalyst and concentration of alkoxides and water. However, it has been difficult to determine the optimum conditions for hydrolysis. Morever, gel-derived compacts often suffer from the commencement of crystallization before densification is completed, leaving large pores unremoved. In the case of silica-containing gels, it is very difficult to remove the remaining pores after the onset of crystallization. This is because the densification by atomic diffusion is much slower than the densification by viscous sintering which is the dominant mechanism for densification before crystallization.[11] Therefore, it is important that the kinetics of viscous sintering are substantially faster than those of crystallization, to obtain dense sintered bodies.

In this work, the preparation of fine, reactive and homogeneous cordierite powders by a solution-polymerization route[12,13] is discussed, and the sintering behavior of these powders is studied. The solution-polymerization route, which is very simple and low cost, employed the Pechini resin[14,15] or the PVA solution[16] as the organic carrier of the pre-ceramic powders. The Pechini resin consists of citric acid, as the chelating agent, and ethylene glycol, to promote polymerization during the esterification process.[14,17] A rather simple-structured and inexpensive polymer, PVA, has a steric entrapment route on polymerization.[16] Both cases are suggested to involve the formation of a soft and bulky precursor. The purpose of this study was to obtain a fully densified and high-purity α-cordierite ceramic using the solution-polymerization route. In addition, to achieve

densification before crystallization, powder prepared from this method was subjected to attrition milling[18,19] before sintering.

II. Experimental Procedure

(1) Powder preparation and sintering

The powders were synthesized from $Mg(NO_3)_2 \cdot 6H_2O$ (reagent grade, Aldrich Chemical Co., Milwaukee, WI); $Al(NO_3)_3 \cdot 9H_2O$ (reagent grade, Aldrich Chemical Co., Milwaukee, WI) and Ludox AS-40 Colloidal silica (40 wt% suspension in water, Du Pont Chemicals, Wilmington, DE). For each precursor, the nitrate salts and the colloidal silica were dissolved in deionized water in stoichiometric proportions. As an organic carrier, either the Pechini resin or the PVA solution was added to the mixture. The 85 wt% Pechini resin,[15] which consisted of 50 mol% citric acid monohydrate and 50 mol% ethylene glycol, was used in this process. The PVA solution was made from 5 wt% PVA (degree of polymerization-1700) dissolved in water. The proportions of the PVA to cation sources in the solution were adjusted in such a way that there were 4 times more positively charged valences from the cations than the negatively charged functional ends of the organics.[16] The resulting solutions were heated and stirred until a crisp, aerated gel was formed. The gel was finely ground and calcined in an air at 750 °C for 1h.

To produce finer particles, the calcined powders were subjected to attrition milling at 180 rpm for various milling times. The charge included 10g calcined powders with 700g zirconia ball media (ball diameter : 5mm). The jar volume was 600 ml and 100 ml iso-propyl alcohol was used as a solvent for milling. Each of the attrition milled and dried powders were uniaxially pressed at 20 MPa followed by iso-static pressing at 25,000 psi for 10 min. The pellet-shaped green compacts were sintered at various temperatures, with 1h soaking time, and finally the furnace was cooled down to room temperature.

(2) Characterization

The particle size distribution and specific surface area of powders were studied using an X-ray absorption spectrometer (Sedigraph Model 5000ET, Micromeritics) and nitrogen gas absorption (Model ASAP 2400, Micromeritics, Norcross, GA). The phase variation of the precursors for cordierite was examined as a function of temperature using an X-ray spectrometer (DMax automated powder diffractometer, Rigaku/USA, Danvers, MA) operated with CuKα radiation (40 kv and 40 mA). The density for the sintered specimens was estimated by the Archimedes method using distilled water as the displacement liquid. The relative density was calculated using the density of the α-cordierite (2.512 g/cm^3) as the theoretical density. The linear shrinkage behavior of

compacted amorphous cordierite as a function of temperature, and the thermal expansion coefficient of the sintered specimens were determined using a dilatometer (Netzsch Dilatometer, 402E, Germany) with a heating rate of 10 °C/min. The morphology of powders and microstructure of sintered bodies were studied by scanning electron microscopy, SEM (ISI DS-130, International Scientific Instruments, Santa Clara, CA) and transmission electron microscopy, TEM (Philips EM-420, Philips instruments, Inc., Mahwah, NJ) equipped with energy dispersive spectroscopy, EDS (EDAX PV 9900, EDAX International, Inc., Prairie View, IL). The SEM samples were prepared by polishing and chemical etching in 20 % HF for 30 sec. For TEM powder specimens, holey formvar films were supported on copper grids. Some powder was then sprayed on the film and carbon coated. The TEM specimen for sintered cordierite was prepared by standard ceramic polishing, dimpling and ion-milling techniques.

III. Results

(1) Densification behavior and phase changes

Both precursors were very soft and porous and easy to grind. A very fine powder was obtained only by hand grinding for a few minutes. Fig. 1 shows a particle size distribution and SEM micrographs of the calcined powders derived from different organic carriers. The powder derived from the Pechini resin had a narrow particle size distribution with particle sizes ranging from 3 μm to 50 μm. Most of the particles were of irregular shape with sharp corners and edges. In the case of the powder derived from PVA solution, though the powder morphology was very similar to the powder prepared with Pechini resin, it had a wider particle size distribution with particle sizes ranging from 1 μm to 100 μm.

Fig. 2 shows variation of phase for amorphous cordierite, derived from the Pechini resin, as a function of heating temperature. Crystalline spinel phase appeared at 900 °C and persisted till 1250 °C. On the other hand, silica remained amorphous up to 1150 °C. As temperature further increased to 1200 °C, amorphous silica crystallized to quartz. α-cordierite started to form at 1250 °C by the solid-state reaction between quartz, cristobalite and spinel. The α-cordierite was formed directly, without a sequential formation of crystalline cordierite (amorphous→μ→α). All phases turned to α-cordierite at 1350 °C.

In comparison, the X-ray diffraction ~~spectra~~ patterns of amorphous cordierite derived from PVA solution are shown in Fig. 3. The precursor remained amorphous at 900 °C. However, in contrast to the Pechini resin process, μ-cordierite appeared with crystalline spinel at 1000 °C. The μ-cordierite was detected below 1200 °C and coexisted with α-

cordierite at a temperature ranging from 1100 °C to 1200 °C. However, as the temperature increased to 1200 °C, μ-cordierite phase disappeared and crystallized to α-cordierite. The onset temperature of α-cordierite was lower than for the Pechini resin process. Only α-cordierite remained at 1300 °C.

Fig. 4 shows the linear shrinkage of amorphous-type cordierite compacts as a function of temperature. The cordierite compact prepared with the PVA solution densified rapidly between 700 °C and 1000 °C. However, the densification stopped at the temperature of crystallization of μ-cordierite. At temperatures above 1200 °C, the powder compact continued to swell slightly. On the other hand, the densification of the powder compact prepared with the Pechini resin occurred continuously until α-cordierite was formed at 1250 °C. The densification was not affected by the crystallization of spinel phase. These results indicate that the densification, in both cases, stops at the crystallization point of amorphous silica. The powder compact derived from the Pechini resin also showed a little swelling above 1300 °C.

Fig. 5 shows variation of bulk density for cordierite compacts at different sintering temperatures. The bulk density of sintered specimens derived from PVA solution had a maximum value at 1100 °C. The bulk density of α-cordierite was higher than the true density in the temperature range from 1000 °C to 1200 °C, because μ-cordierite and spinel phase were the matrix phases of the sintered body. The reduction in density above 1100 °C, which is related to the swelling in the shrinkage curve (Fig. 4), can be ascribed to the formation of α-coedierite, with no more densification occurring. In the case of the powder compact derived from Pechini resin, the maximum density was displayed at 1250 °C and then the reduction in density occurred due to the formation of α-cordieirte. The higher bulk density, than the true density of α-cordierite at above 1100 °C, is attributed to the spinel, quartz and cordierite-type glass phases in the matrix. Even though only α-cordierite was detected in the sintered body by X-ray diffraction at 1350 °C (Fig. 2), that the density was higher than true density of α-cordierite indicated that the cordierite-type glass phases still remained in the matrix after densification.

Morever, the thermal expansion coefficient (3.8×10^{-6}/°C) of the sintered specimen was higher than that of pure α-cordierite. This result confirmed the fact that the sintered body did not consist of only α-cordierite, but also had some cordierite-type glassy phases. In contrast, the close match of the thermal expansion coefficient (2.1×10^{-6}/°C)[1] of the sintered specimen, prepared with PVA solution, with that of α-cordierite shows that the sintered specimen had high purity. The low thermal expansion coefficient meant that most of the μ-cordierite and the other phases changed into α-cordierite through solid-state atomic diffusion above 1100 °C.

The observed densification behavior reflected that the main sintering mechanism was by viscous-flow sintering of the cordierite-type glass phases in both cases. In the PVA solution process, the viscous-flow sintering stopped at the temperature at which amorphous silica crystallized to μ-cordierite. In the case of the Pechini resin process, however, the densification by viscous-flow lasted longer than the powder compact prepared with PVA solution due to the residual cordierite-type glass. This is the reason for the enhanced densification observed in the Pechini resin process.

The scanning electron micrographs of sintered cordierite specimens are shown in Fig. 6. The micrograph of the sintered specimen derived from the Pechini resin was more dense than that from the PVA solution process. The circular-type pores confirmed that viscous-flow sintering had occurred. On the other hand, the sintered specimen derived from PVA solution retained some large pores after viscous sintering. This was because the amorphous silica was depleted by crystallization of μ-cordierite before full viscous-flow sintering occurred. The formation of μ-cordierite at around 1000 °C also occurred in the sol-gel powder preparation process.[8] This means that the PVA solution process is a more atomistically homogeneous synthesis method in comparison with the Pechini resin process. Therefore, the sintered cordierite specimen prepared with the PVA solution had a high purity, with a negligible amorphous silica content. However, the sintered density did not reach the full density of cordierite. If enough densification occurs before the crystallization of the amorphous silica begins, it is possible to prepare dense cordierite ceramics. Hence, it is necessary to obtain a fine and reactive powder, which can enable near full densification at an early stage, for producing a high-density cordierite from the solution-polymerization route.

(2) Densification behavior of attrition milled powder

The calcined powder derived from PVA solution was subjected to attrition milling to prepare fine powder for achieving full densification before crystallization. To obtain sintered cordierite having least amount of amorphous phase, modification of the PVA solution process was important. Fig. 7 shows the variation of linear shrinkage and density of compacted amorphous cordierite as a function of attrition milling time. In general, the longer the attrition milling time, the larger was the shrinkage observed. Nearly 29% linear shrinkage occurred in the sample sintered at 950 °C when the milling was done for only 15 min. The shrinkage improved remarkably up to the milling time of 60 min. The change in shrinkage with increasing milling time was insignificant after 60 min. A large shrinkage of about 36% was observed when the milling was done for 60 min. The 36% shrinkage was obtained when the specimen was sintered at 950 °C which is the temperature before

crystallization to μ-cordierite. The density of the specimens sintered at 950 °C was higher than the true density for all milling times. This was because the main phases of the matrix were amorphous silica and some μ-cordierite. In the case of the specimen sintered at 1300 °C, the shrinkage for the same milling time was a little lower than that of the specimens sintered at 950 °C because of the formation of α-cordierite with no more viscous-flow sintering. Accordingly the density also decreased due to the open structure caused by formation of α-cordierite. The measured thermal expansion coefficient of the specimen, attrition milled for 60 min and sintered at 1300 °C, was 2.2×10^{-6}/°C. Both the density and the thermal expansion coefficient of this specimen were quite close to those of pure α-cordierite. Fig. 8 shows a transmission electron micrograph of the amorphous cordierite powder attrition milled for 60 min. The powder consisted of very fine primary particles, 30 nm in size, and had a BET specific surface area of 181 m^2/g. These results were almost similar to the nano size particles prepared by the sol-gel process.[8,11] EDS microanalysis (Fig. 8) showed that the attrition milled and calcined powder retained a stoichiometric composition of cordierite and only 0.01 wt% impurity was added during the attrition milling. In addition, the average composition calculated from 3 data points by EDS analysis shows that the powder had a uniform spatial distribution of constituent phase on a nano-size scale. The micrographs of the polished and chemically etched surfaces of the specimens, attrition milled for two different times and sintered at 1300 °C, are shown in Fig. 9(a), (b). The both microstructures were much more dense than that of an unattrition-milled specimen shown in Fig. 6(b). In case of the specimen attrition milled for 60 min, the pore size was smaller than the specimen attrition milled for 240 min. Fig. 10 shows TEM bright-field internal texture and corresponding SAD pattern of the specimen attrition milled for 60 min. The cordierite crystallite, approximately 0.8 μm in diameter, was observed and the SAD pattern showed reflections from crystalline α-cordierite called indialite (stable hexagonal form) without any amorphous ring pattern.

IV. Discussion

The mechanism of sintering of the amorphous cordierite powders prepared by solution-polymerization route consists of viscous-flow and subsequent crystallization with coalescence. In the case of the Pechini resin process, the sintering process was observed until the final stage. Free silica cations were produced during the process and resulted in amorphous silica phase in the matrix. The chelation of the dissolved metal ions by the carboxylic acid end of the citric acid was incomplete in the Pechini resin process. The chelating action is suggested to be responsible for the formation of a stable, atomistically homogeneous, pre-ceramic organometallic. However, the stabilization of the metal ions in

the organics was not enough in the multi-component system when the Pechini resin was used.

In the case of PVA solution method, the polymer only had hydroxyl functional groups and steric entrapment of the metal ions was achieved by using these large chain molecules. The crystallization of μ-cordierite from amorphous silica at an early stage of sintering and depletion of amorphous silica after sintering are a result of this steric entrapment of the metal cations. Hence a chemically homogeneous structure, at the molecular-scale level, was possible.

The nano-size powder prepared by mechanical attrition milling, with wet grinding condition, was very effective in improving densification. It enabled these particles, with 30 nm size, to attain nearly full densification by viscous-flow sintering. Though increased shrinkage resulted on attrition milling for longer times, the longer milling time increased the contamination due to media wear. Therefore, it is desirable to optimize the milling time to reach near full densification with least possible contamination. In the viscous-flow sintering of the nano-size particles, some spherical-type pores remained in the matrix which is typical of glass powder sintering (Fig. 6, 9). On the other hand, the sintered density using the nano-size particles did not increase even though the shrinkage increased with milling times of more than 60 min (Fig. 7(b)). This is caused by increase in size of the residual pores in the sintered body. The larger pores may be due to particle agglomeration during viscous sintering, and then coalescence of cordierite grains after the viscous sintering stopped with no further shrinkage. The driving force for particle agglomeration and coalescence of grains increased with the increase in surface area of the powder.

V. Conclusions

A dense and pure α-cordierite was obtained from nano-size powder by applying attrition milling to the calcined powder prepared by a solution-polymerization route employing aqueous PVA solution. The solution-polymerization process was a simple and inexpensive technique for producing multi-component systems, such as a cordierite, on a molecular-scale level. The nano-size amorphous-type cordierite powder attrition milled for 60 min had a BET specific surface area of 181 m^2/g and stoichiometric cordierite composition. The powder was densified fully before the onset of crystallization to μ-cordierite at 950 °C. The attrition milling was very effective on the soft and porous, amorphous-type, cordierite powder.

Acknowledgement: We gratefully acknowledge the valuable assistance of Dr. Z. Xu with the TEM/EDS analysis. This work was partially supported by the US Air Force Office of Scientific Research through Dr. Alexander Pechenik under grant number F 49620-93-1-0227.

References

1. I.M. Lachman, R.D. Bagley, and R.M. Lewis, "Thermal Expansion of Extruded Cordierite Ceramics," *Ceram. Bull.*, **60**[2] 202-205 (1981).
2. H. Ikawa, T. Otagiri, O. Imai, M. Suzuki, K. Urabe, and S. Udagawa, "Crystal Structures and Mechanism of Thermal Expansion of High Cordierite and Its Solid Solutions," *J. Am. Ceram. Soc.*, **69**[6] 492-498 (1986).
3. K. Watanabe and E. Giess, "Coalescence and Crystallization in Powdered High-Cordierite ($2MgO{\cdot}2Al_2O_3{\cdot}5SiO_2$) Glass," *J. Am. Ceram. Soc.*, **68**[4] C-102-103 (1985).
4. R.S. Lamar and M.F. Warner, "Reaction and Fired-Property Studies of Cordierite Compositions," *J. Am. Ceram. Soc.*, **37**[12] 602-610 (1954).
5. B.H. Mussler and M.W. Shafer, "Preparation and Properties of Mullite-Cordierite Composites," *Ceram. Bull.*, **63**[5] 705-710 (1984).
6. W. Hutton and J.S. Thorp, "The Vibrational Spectra of MgO-Al_2O_3-SiO_2 Glass Containing TiO_2," *J. Mater. Sci.*, **20**[2] 542-551 (1985).
7. G.H. Beall, "Glass Ceramics"; pp. 157-173 in Advances in Ceramics, vol 18, *Commercial Glasses*. Edited by D.C. Boyd and J.F. MacDowell. American Ceramic Society, Columbus, OH, 1986.
8. H. Suzuki, K. Ota, and H. Saito, "Preparation of Cordierite Ceramics from Metal Alkoxides (Part I)," *Yogyo-Kyokai-Shi*, **95**[2] 28-32 (1987).
9. T. Hayashi and H. Saito, "Preparation of CaO-SiO_2 Glass by the Gel Method," *J. Mater. Sci.*, **15**[8] 1971-77 (1980).
10. B.E. Yoldas, "Modification of Polymer-Gel Structures," *J. Non-Crystal. Solids*, **63**[1,2] 145-54 (1984).
11. J. Werckmann, P. Humbert, C. Esnouf, J.C. Broudic, and S. Vilminot, "Microscopic Characterization of Sol-Gel Processed Cordierite," *J. Mater. Sci.*, **28**, 5229-5236 (1993).
12. M. Pechini, "Method of Preparing Lead and Alkaline-Earth Titanates and Niobates and Coating Method Using the Same to Form a Capacitor," U.S. Pat. No. 3 330 697, July 11, 1967.
13. D. Budd and D.A. Payne, "Preparation of Strontium Titanate Ceramics and Internal

Boundary Layer Capacitors by the Pechini Method," *Mater. Res. Soc. Symp. Proc.*, **32**, 239 (1984).

14. L.W. Tai and P.A. Lessing, "Modified Resin-Intermediate Processing of Perovskite Powder: Part I. Optimization of Polymeric Precursors," *J. Mater. Res.*, 7[2] 502-510 (1992).
15. L.W. Tai and P.A. Lessing, "Modified Resin-Intermediate Processing of Perovskite Powder: Part II. Processing for Fine, Nonagglomerated Sr-Doped Lanthanum Chromite Powders," *J. Mater. Res.*, 7[2] 511-519 (1992).
16. M.A. Gulgun and W.M. Kriven, "A Simple Solution-Polymerization Route for Oxide Powder Synthesis"; pp. 57-66 in Ceramic Transactions, Vol. 62, *Science, Technology, and Commercialization of Powder Synthesis and Shape Forming Processes*. Edited by J.J Kingsley, C.H. Schilling, and J.H. Adair. American Ceramic Society, Westerville, OH, 1996.
17. P.A. Lessing, "Mixed-Cation Oxide Powder via Polymeric Precursors," *Am. Ceram. Soc. Bull.*, **68**[5] 1002-1007 (1989).
18. J.E. Becker, "Attritor Grinding of Refractories," *Am. Ceram. Soc. Bull.*, 75[5] 72-74 (1996).
19. H.J. Fecht, "Nanostructure Formation by Mechanical Attrition," *Nanostructured Mater.*, 6[1-4] 33-42 (1995).

Figure Captions

Fig. 1. Effect of organic carriers on the particle size distribution of the calcined powders. SEM micrographs showing the effect of the organic carriers in the precursors on the particle size distribution of the calcined powders derived from (a) Pechini resin and (b) PVA solution.

Fig. 2. X-ray diffraction ~~spectra~~ patterns of amorphous cordierite derived from Pechini resin at various heating temperature (holding time at each temp. : 1h).

Fig. 3. X-ray diffraction ~~spectra~~ patterns of amorphous cordierite derived from PVA solution at various heating temperature (holding time at each temp. : 1h).

Fig. 4. Linear shrinkage of compacted amorphous cordierite prepared with Pechini resin and PVA solution as a function of sintering temperature.

Fig. 5. Bulk density of the amorphous-type cordierite powder compacts sintered at various temperatures for 1h. Thermal expansion coefficient of the specimens sintered at 1300 °C for 1h.

Fig. 6. SEM photographs of polished surface of sintered cordierite specimens derived from (a) Pechini resin and (b) PVA solution sintered at 1300 °C for 1h (etching condition : 20 % hydrofluoric acid for 30 sec).

Fig. 7. Linear shrinkage and density of compacted amorphous cordierite sintered at (a) 950 °C and (b) 1300 °C for 1h, derived form PVA solution after various attrition milling times.

Fig. 8. TEM micrograph and EDS spectrum of the amorphous cordierite powder, which is derived from PVA solution and attrition milled for 60 min.

Fig. 9. SEM micrographs of the cordierite specimens attrition milled for (a) 60 min, (b) 240 min and sintered at 1300 °C for 1h.

Fig. 10. TEM brigh-field image with corresponding SAD pattern of the specimen attrition milled for 60 min and sintered at 1300 °C for 1h.

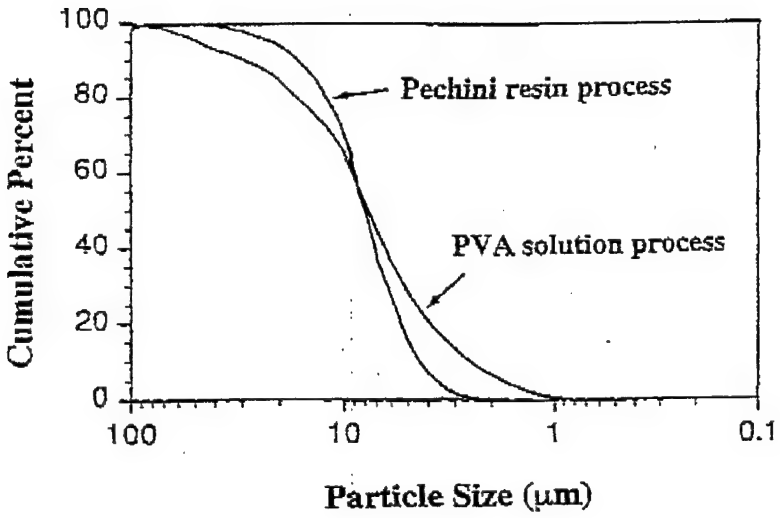

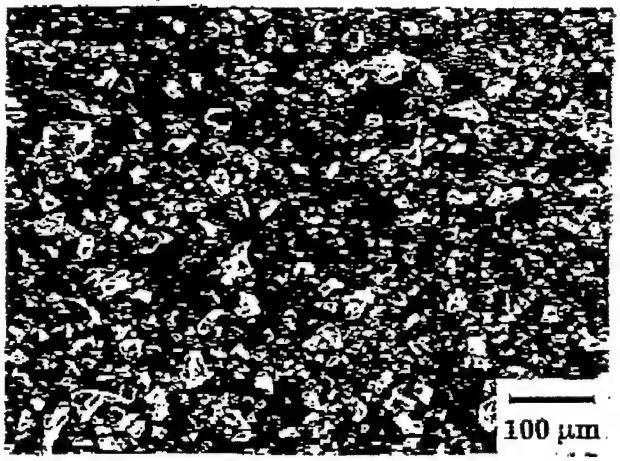

(a) Pechini

(b) PVA

Figure 1

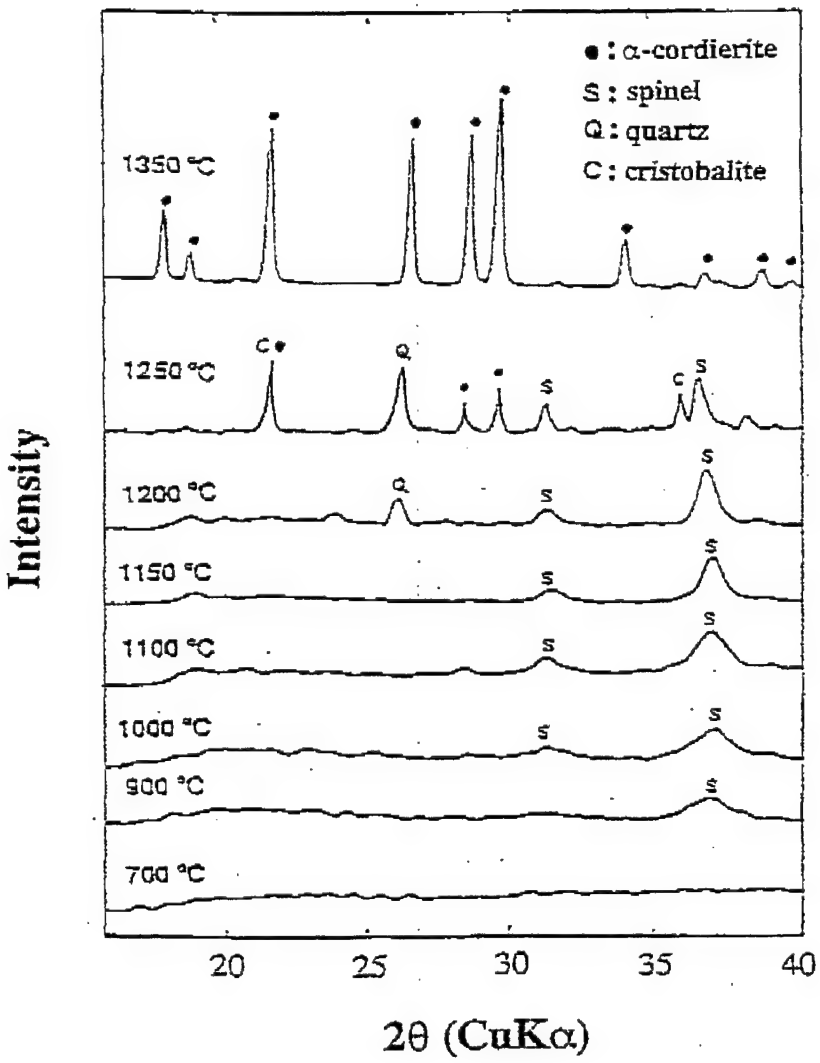
●: α-cordierite
S: spinel
Q: quartz
C: cristobalite
1350 °C
1250 °C
1200 °C
1150 °C
1100 °C
1000 °C
900 °C
700 °C
Intensity
20
25
30
35
40
2θ (CuKα)

Figure 2

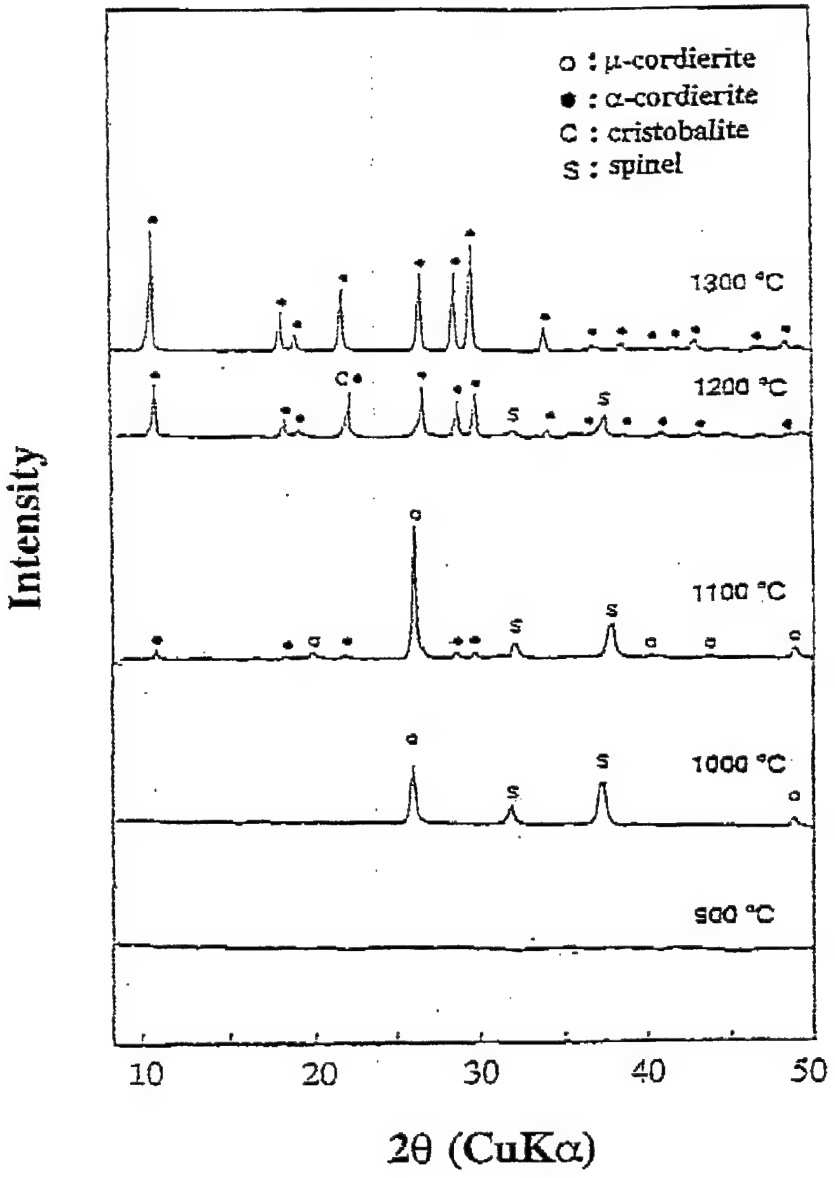
o : μ-cordierite
● : α-cordierite
C : cristobalite
S : spinel
1300 °C
1200 °C
1100 °C
1000 °C
900 °C
Intensity
10
20
30
40
50
2θ (CuKα)

Figure 3

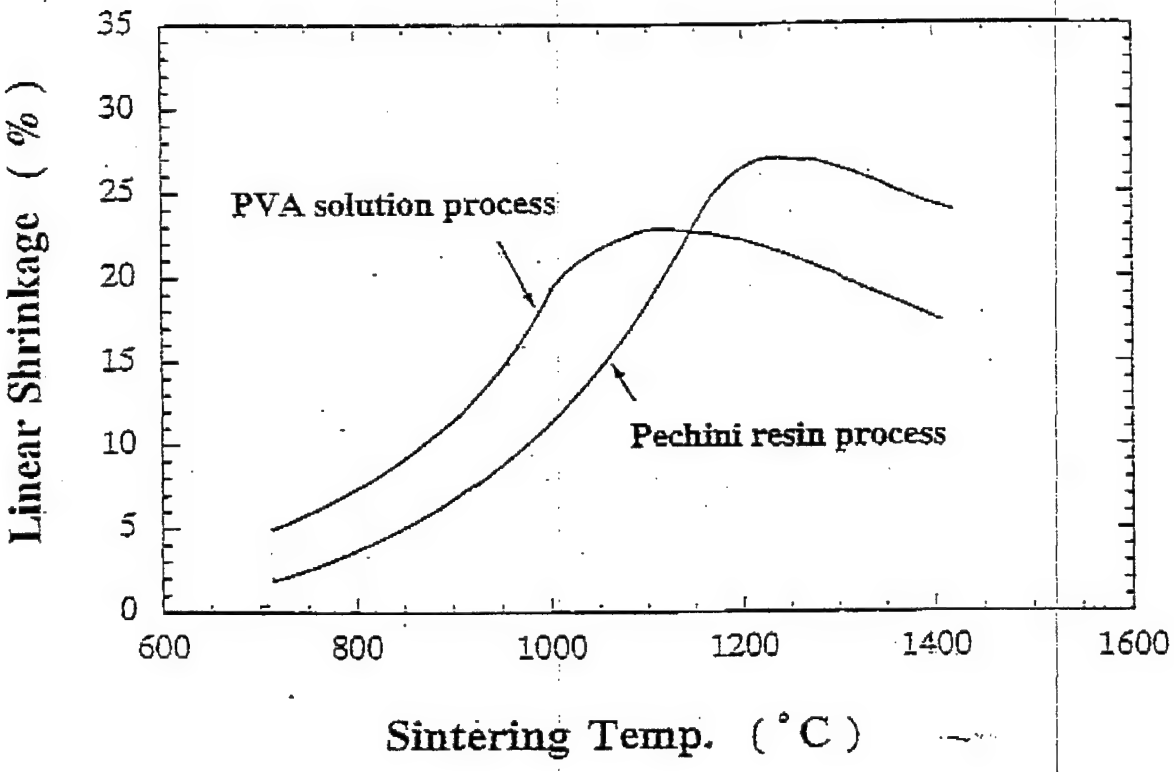
Linear Shrinkage (%)
35
30
25
20
15
10
5
0
600
800
1000
1200
1400
1600
PVA solution process
Pechini resin process
Sintering Temp. (°C)

Figure 4

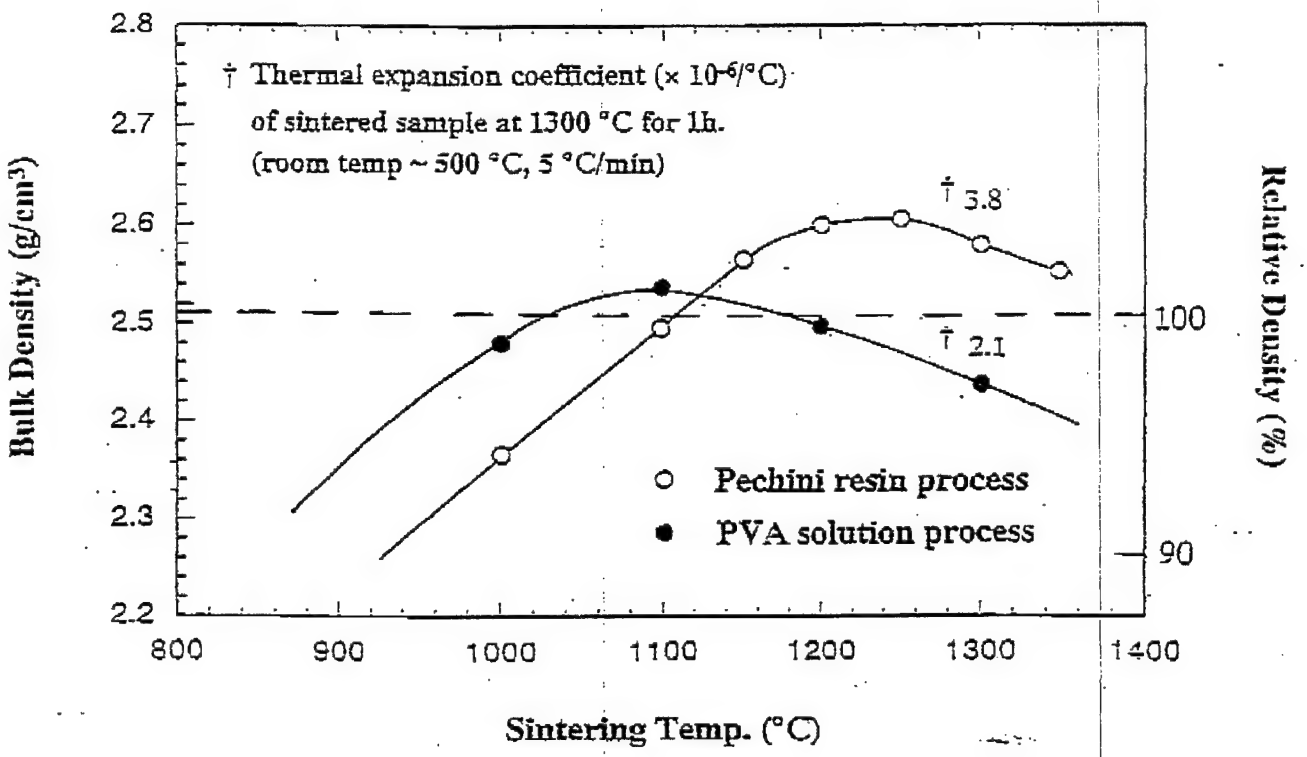
† Thermal expansion coefficient (× 10⁻⁶/°C)
of sintered sample at 1300 °C for 1h.
(room temp ~ 500 °C, 5 °C/min)
† 3.8
† 2.1
Pechini resin process
PVA solution process
Bulk Density (g/cm³)
Relative Density (%)
Sintering Temp. (°C)
2.8
2.7
2.6
2.5
2.4
2.3
2.2
100
90
800
900
1000
1100
1200
1300
1400

Figure 5

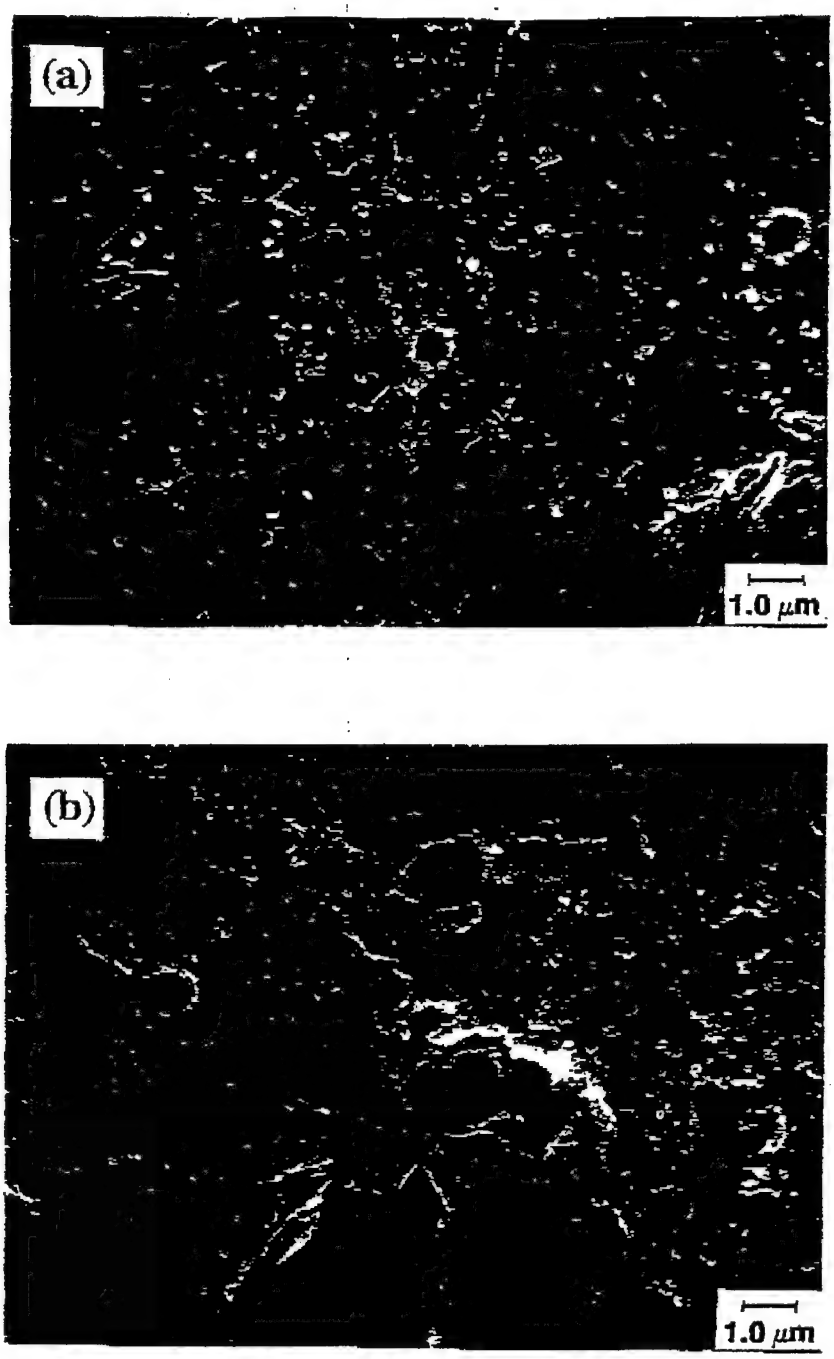

Figure 6

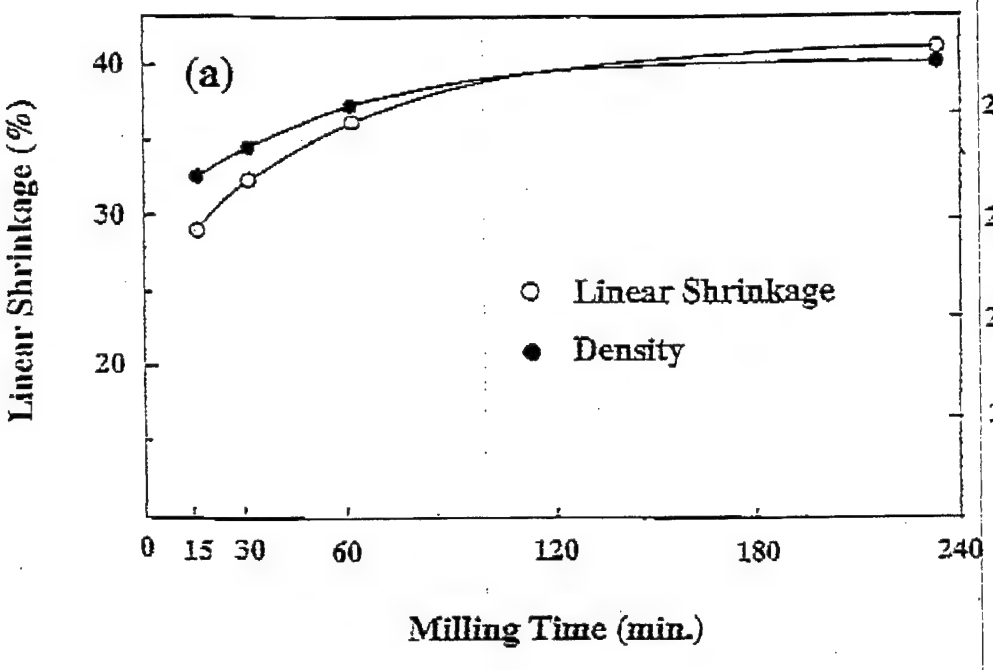

Sintered at 950°C

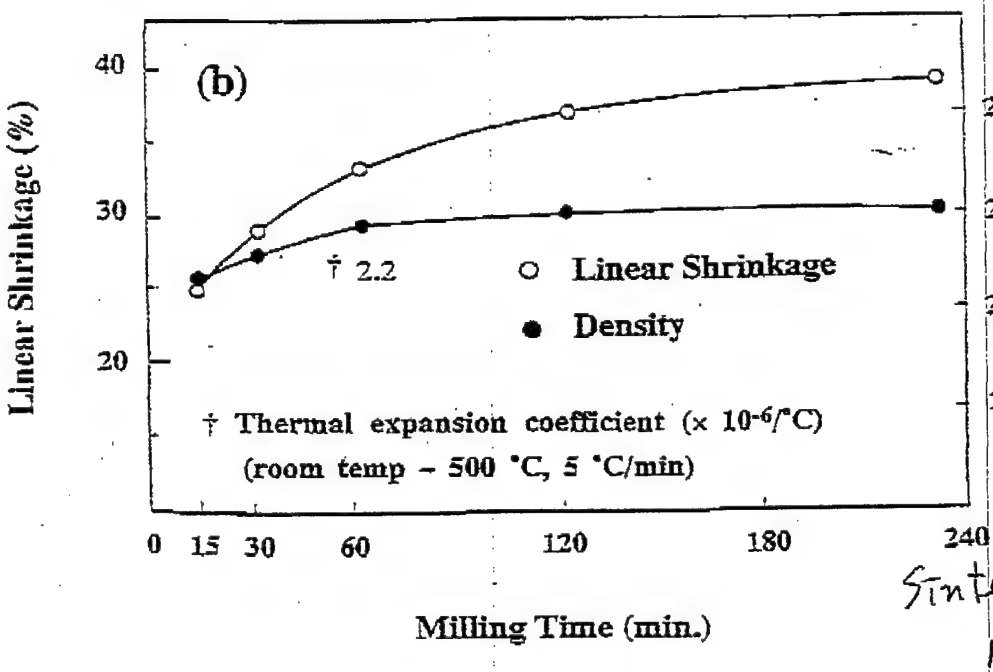

Sintered at 1300°C.

Figure 7

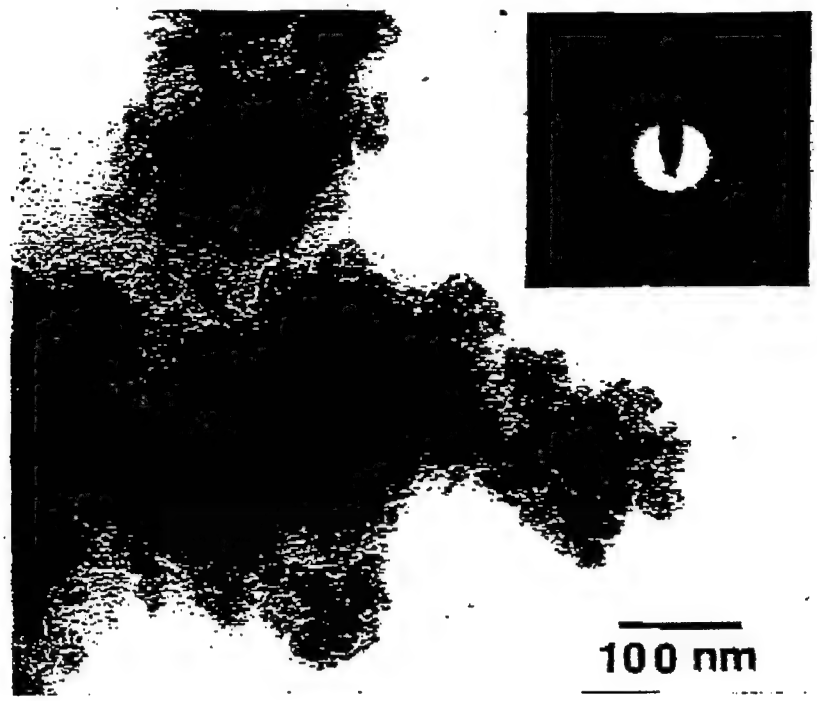

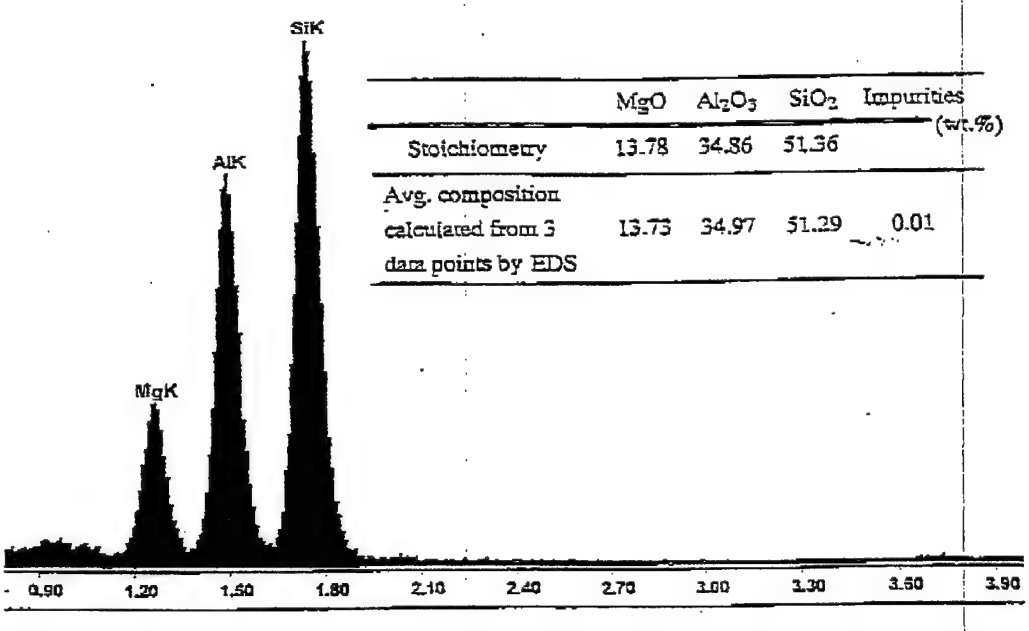

	MgO	Al_2O_3	SiO_2	Impurities (wt.%)
Stoichiometry	13.78	34.86	51.36	
Avg. composition calculated from 3 dam points by EDS	13.73	34.97	51.29	0.01

Figure 8

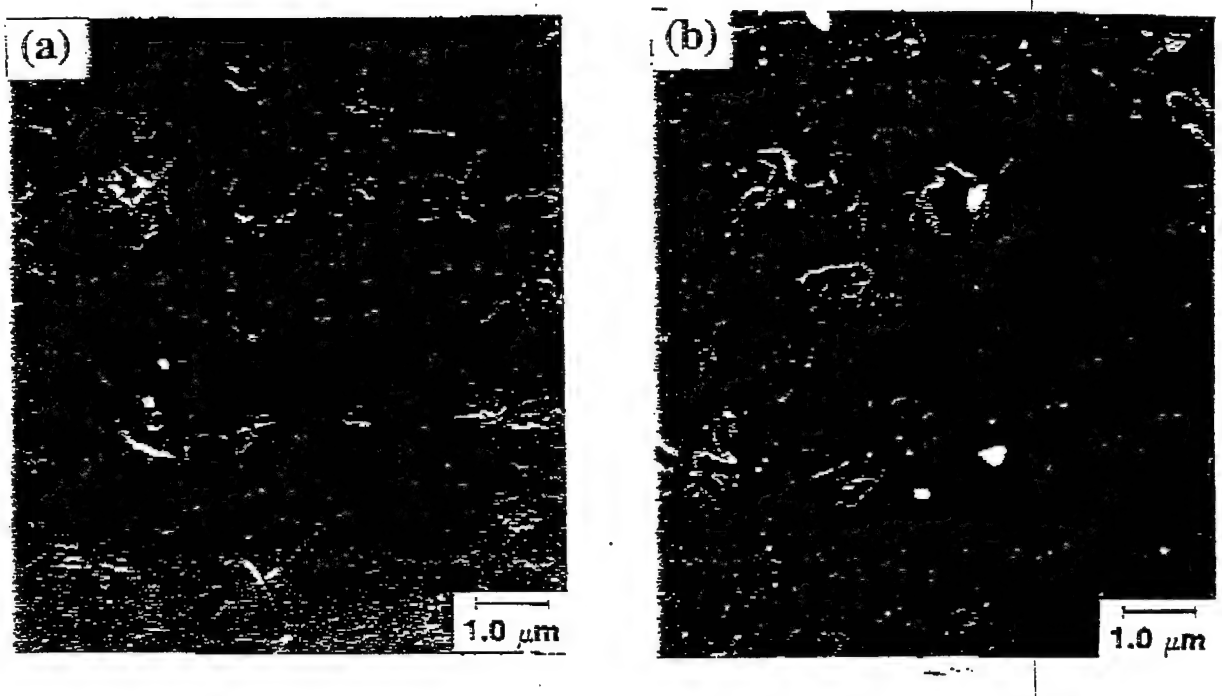

Figure 9

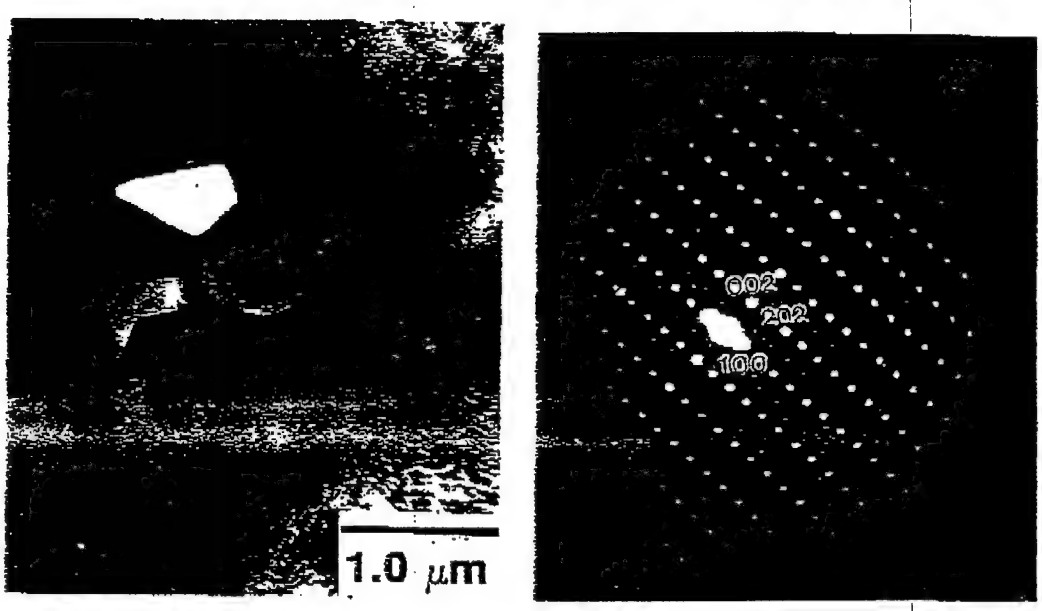

Figure 10

SYNTHESIS AND CHARACTERIZATION OF MULLITE AND YAG FIBERS GROWN FROM DEEPLY UNDERCOOLED MELTS

Dong Zhu, Mohammad H. Jilavi and Waltraud M. Kriven

Department of Materials Science and Engineering
University of Illinois at Urbana-Champaign
Urbana, IL 61801

ABSTRACT

Mullite ($3Al_2O_3 \cdot 2SiO_2$) and YAG ($Y_3Al_5O_{12}$) fibers were pulled out from deeply undercooled melts using a CO_2 laser. The as-pulled fibers were amorphous. The tensile strengths and microstructures of mullite fibers were examined before and after recrystallization. The fracture behavior and composition distribution of YAG fiber on fracture surfaces were observed using SEM and EDS.

INTRODUCTION

Structural fibers that exhibit high strength, low creep, and oxidation resistance at high temperatures are a key requirement in the development of advanced ceramic-ceramic composite materials.[1-3] Oxide materials offer considerable potential to meet this need; many oxides have the required high intrinsic properties. Mullite and YAG fibers[4-5] have been recently developed with anticipated creep properties at high temperatures. However, the synthesis of oxide fibers with sufficiently high practical properties and acceptably low production cost has not yet been achieved.

We have recently shown that oxide glass fibers can be formed from many new materials by pulling the fibers from deeply undercooled melts in which melt viscosities are sufficient for fiber pulling operations. This paper presents our initial investigations on the recrystallization and structure of mullite and YAG glass fibers, in the course of work to develop the fibers for high temperature structural applications.

EXPERIMENTAL PROCEDURES

Fiber Synthesis

Bulk crystalline oxide materials were first formed into dense specimens of ~0.3 cm diameter by melting in a laser hearth melter.[6] Mullite of stoichiometric $3Al_2O_3 \cdot 2SiO_2$ composition was obtained from Kyoritsu (KM mullite 101, Kyoritsu, Nagoya, Japan) and yttrium aluminate garnet (YAG) of $Y_3Al_5O_{12}$ was fabricated by an organic PVA complex polymerization method [7]. The specimens were then levitated and melted with a CO_2 laser beam. Initial experiments demonstrated that deep undercooling of the melt was possible when the heating laser intensity was reduced under the containerless processing conditions[8]. Melt temperatures equal to 0.8 of the absolute melting point were typically obtained, and some of the materials formed bulk glass specimens upon cooling to ambient temperatures. Fibers were pulled from the levitated drops of undercooled liquid by inserting a 100 μm diameter tungsten stinger into the molten drop and quickly withdrawing the stinger with a spring or stepper motor driven actuator. Fiber pulling velocities ranged from 5 to 120 cm/s.

The materials were chosen for their capability to provide high temperature strength, high modulus, chemical stability in oxidizing environments, creep resistance, and/or compatibility with matrix and interface-modifying coatings.

Fiber Characterization

Scanning electron microscopy (SEM) and microchemical analysis (EDS) were used to evaluate the surface morphology, the diameter of fibers along their lengths, fiber cross section, the fracture surface of fibers, and the chemical composition of the fibers. Transmission electron microscopy (TEM) and selected area electron diffraction (SAD) techniques in a Philips CM12 TEM were used to characterize fiber microstructure. Fibers prepared by ion milling, were examined both lengthwise and in cross-section.

Crystallization and Annealing

Glass fibers of the mullite composition were annealed in argon at temperatures of 1100°, 1200°, 1300°, and 1500°C for one hour. Lengths of fiber were placed on a carbon foil holder and heated at a rate of 5°C/min to the annealing temperature.

Mechanical Evaluation

Tensile strengths of glass and recrystallized fibers were measured using an Instron Material Testing Machine. The fiber diameters were 20-30 μm, the gauge length was fixed at 23 mm, approximately 1000 times that of the fiber diameter. Test fibers were bonded into a specially designed frame with "M-Bond" epoxy adhesive. The measurement technique and interpretation was consistent with ASTM standard D3379-75. Tests were performed in an Instron 1205 tensile machine operated under

computer control. Fibers were pulled at a constant strain rate of 5 μm/s. A high sensitivity load cell was used to measure load. A computer was used to record the load and displacement as a function of time. Broken fibers were examined by optical microscopy to determine the cross section so that stress could be determined.

RESULTS AND DISCUSSION

Glass Fiber Synthesis and Mechanical Evaluation

Table 1 presents results of fiber synthesis experiments. In some cases, the composition is given in terms of the mole percentage of its component oxides. Typical glass fiber diameters are indicated in column 2. Tensile strengths were measured for a few glass and recrystallized mullite and YAG fibers as given in the third column.

Table 1. Fiber materials, diameters, and tensile strengths

Material	Fiber Diameters, μm	Tensile Strength, GPa
$60\%Al_2O_3$-$40\%SiO_2$ Mullite (glass)	1 ~ 50	5.7 ± 0.6
Mullite recrystallized at 1100°-1200°C	8 ~ 19	0.7 ~ 1.0
50-72%Al_2O_3 and 28-50%SiO_2 (glass)	1 ~ 50	not tested
62.5%Al_2O_3 and 37.5%Y_2O_3 YAG (glass)	8 ~ 43	2.4 ± 0.1

The fibers were pulled at rates of 5 to 120 cm/s. The fiber diameter could be controlled via the melt viscosity (degree of undercooling) and the pulling rate. The preferred temperature range for drawing fibers was typically 70-140°C below the melting point for $Al_2O_3 \cdot SiO_2$ and the YAG compositions, and was not measured for forsterite compositions. At higher temperatures, rather short fibers were obtained, or the stinger pulled from the melt without drawing a fiber. At lower temperatures, the fiber drawing force tended to pull the entire sample from its levitated position. In preliminary experiments the fibers were pulled at rates which increased continuously, leading to tapered fibers. Later experiments, using the stepper-motor driven puller which rapidly accelerated to a constant pulling rate, led to uniform fiber diameters.

Microstructure Characterization

Fibers pulled at constant velocity using the stepper motor-driven puller had uniform diameters of 10-40 μm. These fibers were pulled in lengths up to 50 cm.

They were easy to handle and could be bent to a radius of 2 ~ 3 mm. Figs. 1 (a) and (b) are SEM micrographs of the surfaces of mullite and YAG fibers respectively. The fiber surfaces were smooth, homogeneous and free from imperfections.

Fibers made from mullite ($3Al_2O_3 \bullet 2SiO_2$) were examined by TEM. Fig. 2 is a micrograph of a thinned section of a mullite fiber. The corresponding diffraction rings obtained by selected area diffraction (SAD) at several points on the fiber were diffuse indicating that the fiber was amorphous. The absence of extinction contours and grain boundaries confirmed this observation.

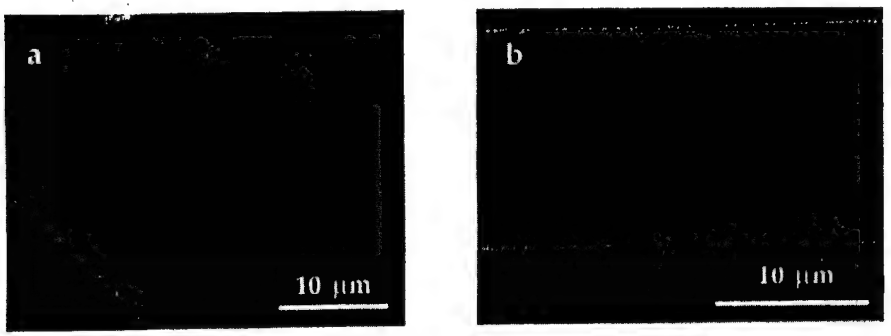

Fig. 1 Scanning electron micrograph of (a) mullite and (b) YAG fiber surfaces. The fiber surface was smooth, homogeneous and free from imperfections.

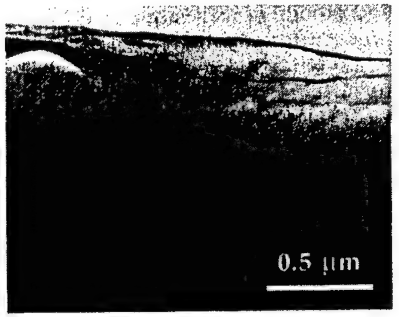

Fig. 2 TEM micrograph of an amorphous mullite fiber. The specimen surface ripples are artifacts from the ion milling operation used to prepare the specimen. The corresponding diffuse diffraction pattern indicated that the material was amorphous.

Fracture Behavior of YAG Fibers

After tensile testing, the fracture surface of YAG fibers was observed using SEM, as shown in Fig. 3. The arrows in the pictures indicate the crack initiation. The diameter of the fracture section was approximately 40 μm. In Fig. 3 (a), the characteristics of cleavage fracture initiated from the fiber surface. Fig. 3 (b) is the closed view of the origination area of cleavage. On the fiber surface, some large and small pittings were found, as indicated by P and p respectively. These pittings are considered to be initiating origins causing cleavage fracture.

Composition Analysis

In general fibers grown from boules of $3Al_2O_3 \bullet 2SiO_2$ composition retained their stoichiometry. However, chemically inhomogeneous regions were occasionally found near the ends of some fibers or in the fibers of 70 mol% composition that were pulled during the initial experiments.

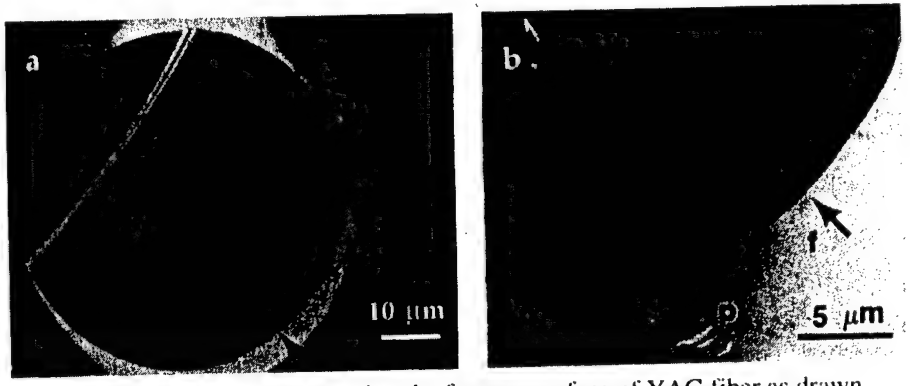

Fig. 3 SEM micrographs showing the fracture surface of YAG fiber as drawn. The arrows indicate the initiation of crack. (a) The diameter of fracture section was about 40 μm. (b) The originating area of cleavage.

EDS X-ray was detected at different locations on the fracture surface of YAG fiber to show inhomogeneous distribution of composition. Fig. 4 (a) shows X-ray spectra on the core of fiber and from the crack initiation area as indicated by the frame and the arrow in Figs. 3 (a) and (b) respectively. Fig. 4 (b) is an X-ray spectrum from the YAG fiber surface. The peak intensity ratio of Al / Y in the core of the YAG fiber is higher than the ratio in the surface areas. No considerable difference in spectra was observed between the crack initiation area and the fiber surface. The results of EDS analysis of the YAG fiber are summarized in Table 2. The composition in the core of the YAG fiber was very close to the stoichiometry of $Y_3Al_5O_{12}$. However, either on the surface or subsurface of the YAG fiber, the Y content was much higher than the theoretical composition.

The inhomogenouos compositional distribution of YAG fibers may be caused by vaporization of material components during melting and pulling of the fibers.

Recrystallization Studies

The fibers pulled from stoichiometric mullite ($3Al_2O_3 \bullet 2SiO_2$) were amorphous. The fibers were annealed in air. Fibers annealed at 1500°C broke into several pieces. Fibers annealed at 1300°C retained their shape but were too delicate to handle. Fibers annealed at 1100°C and 1200°C could be handled and tensile tests were performed on several of these fibers. The retained strength was ~1 GPa.

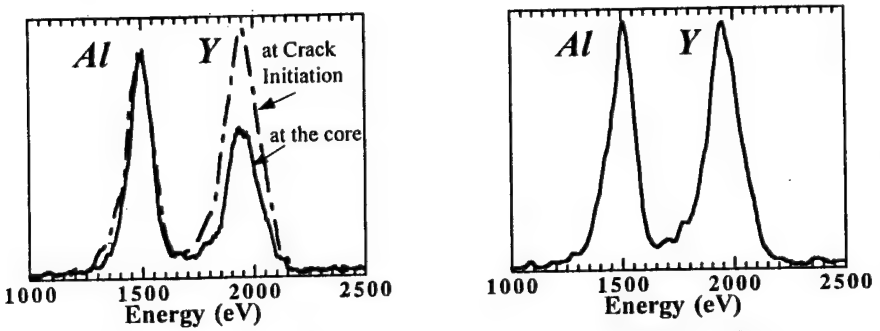

(a) Fracture Surface (b) Fiber Surface

Fig. 4 EDS X-ray spectra of YAG fiber.

Table 2 Compositional distribution in YAG fiber.

Area for EDS		Nominal *wt%*				Oxide *wt%*			
		Al	ΔAl	Y	ΔY	Al_2O_3	ΔAl_2O_3	Y_2O_3	ΔY_2O_3
Stoichiometry		33.6		66.4		42.9		57.1	
Core of fiber	Ave.	32.1	-1.5	67.9	+2.5	41.3	-1.6	58.8	+1.7
	SD	0.85		0.85		1.03		1.02	
Crack init.	Ave.	18.3	-15.3	81.7	+15.3	24.8	-18.1	74.7	+17.6
	SD	3.21		3.21		4.02		4.01	
Fiber surface	Ave.	23.5	-10.1	76.5	+10.1	31.4	-11.5	68.7	+11.6
	SD	2.90		2.90		3.43		3.46	

Δ The deviation from stoichiometry.

Fibers annealed at 1200°C were examined by TEM. Fig. 5 shows that the microstructure was polycrystalline with a sub-micron grain size. Bright field (BF) and selected area electron diffraction (SAD) of a typical individual grain are given in Fig. 5 (a) and (b) which was indexed as stable $3Al_2O_3 \cdot 2SiO_2$ mullite. This was confirmed by microchemical analysis using energy dispersion X-ray spectroscopy (EDS) in the TEM.

Microstrutural analysis shows that the fibers have a smooth and homogeneous surface. The tensile strength of the amorphous mullite fibers is approximately 6 GPa which significantly exceeds the 2.1 GPa strength of commercially available fine grained alumina fibers (Nextel 720®). Mullite fibers of the $3Al_2O_3 \cdot 2SiO_2$ composition were crystallized at 1200°C into random orientations and sub-micron grain size. Their tensile strength was of the order of 1 GPa. This method of crystallization by heating the whole fiber at once, at the annealing temperature, yielded a microstructure which suggested that nucleation occurred at multiple sites and in an uncontrolled way. The crystal structures of mullite

($3Al_2O_3 \cdot 2SiO_2$) is based on the high pressure sillimanite ($Al_2O_3 \cdot SiO_2$) polymorph [9-11]. They are basically chain structures, consisting of chains of edge-shared AlO_6 octahedral arranged parallel to the orthorhombic [c] axis, and placed at the corners and center of each unit cell. In sillimanite, there are a further four chains of alternating AlO_4 and SiO_4 corner-shared tetrahedral which are arranged symmetrically within the unit cell. In mullite, only three chains of AlO_4/SiO_4 tetrahedral are arranged within each unit cell so as to be statistically randomized to X-ray diffraction, but give rise to the complex incommensurate modulations observed by TEM.[12-14] Thus extremely high strength and creep resistance would be expected from single crystal fibers having the [c] axis aligned parallel to the fiber length. One may speculate that even a polycrystalline, textured fiber with aligned [c] axes[15] should yield significantly improved tensile strengths, as compared to randomly crystallized polycrystalline fibers.

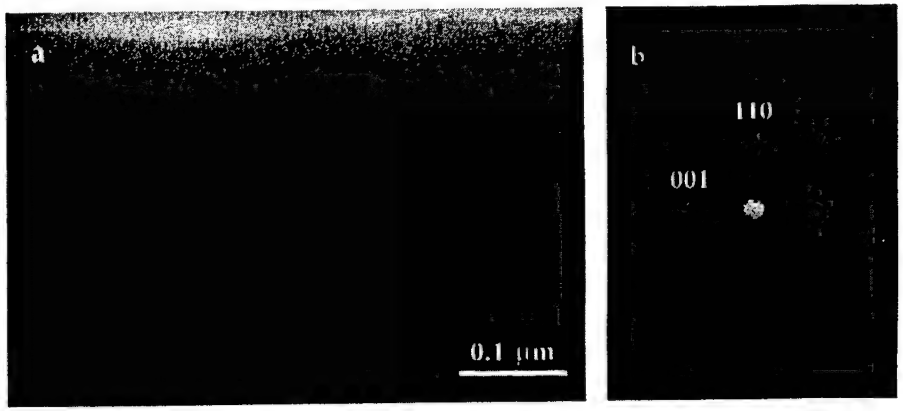

Fig. 5 (a) Bright field TEM micrograph of an individual mullite grain and (b) corresponding selected area diffraction pattern indexed as $3Al_2O_3 \cdot 2SiO_2$ mullite in the $[1\,\bar{1}\,0]$ zone axis.

SUMMARY

Oxide glass fibers with fracture strengths up to 6 GPa can reproducibly be made by pulling from undercooled molten oxide precursors. Glass fibers (e.g. mullite, YAG) can be recrystallized to form equilibrium phases corresponding to the composition of the starting material. Alumino-silicates of the $3Al_2O_3 \cdot 2SiO_2$ composition crystallize into the equilibrium 3:2 mullite form.

ACKNOWLEDGEMENT

This work was supported by a Small Business Innovation Research (SBIR) Grant number F49620-95-C-0067 through the US Air Force Office of Scientific Research, under the supervision of Dr. Alexander Pechenick.

REFERENCES

1. R.A. Lowden and M.A. Karnitz, "A Survey of the Status of Ceramic Reinforcement Technology and Its Relationship to CFCCs for Industrial Applications," Oak Ridge National Laboratory, Oak Ridge, TN (1996).
2. A.G. Evans, "Perspective on the Development of High Toughness Ceramics," J. Am. Ceram. Soc., **73** [2] 187-206 (1990).
3. R.J. Kerans, R.S. Hay, N.J. Pagano and T.A. Parthasarathy, "The Role of Fiber- Matrix Interfaces in Ceramic Composites," Am. Ceram. Soc. Bull., **68** [2] 429-442 (1993).
4. A. Sayir and L.E. Matson, "Growth and Characterization of Directionally Solidified $Al_2O_3/Y_3Al_5O_{12}$ (YAG) Eutectic Fibers," NASA Conf. Publications 10082 High Temp. Review, Oct 29th - 30th (1991), pp. 83.1-83.13.
5. J.M. Collins, H.E. Bates and J.J. Fitzgibbon, "Growth and Characterization of Single Crystal YAG Fibers," Materials Directorate, Wright Laboratory, Air Force Material Command, Wright Patterson AFB, OH Report WL-TR-94-4085, June 1994.
6. J.K.R. Weber, J.J. Felten and P.C. Nordine, "New Method for High Purity Ceramic Synthesis," Rev. Sci. Instrum., **67**, 552-24 (1996).
7. M. A. Gulgun and W. M. Kriven, "A Simple Solution-Polymerization Route for Oxide Powder Synthesis," Ceramic Transactions **62** (1995) 57 - 66.
8. J.K.R. Weber, D.S. Hampton, D.R. Merkley, C.A. Rey, M.M. Zatarski and P.C. Nordine, "Aero-acoustic Levitation - A Method for Containerless Liquid Phase Processing at High Temperatures," Rev. Sci. Instrum., **65**, 456-465 (1994).
9. C. W. Burnham, "The Crystal Structure of Mullite," Yearb. Carnegie Inst., **62**, 158- 165 (1963).
10. S. Durovic, "Refinement of the Crystal Structure of Mullite," Chem. Zvesti, **23**, 113-128 (1969).
11. S. O. Agrell and J. V. Smith, "Cell Dimensions, Solid Solutions, Polymorphism and Identification of Mullite and Sillimanite," J. Am. Ceram. Soc., **43** [2] 69-76 (1960).
12. W. E. Cameron, "Mullite: A Substituted Alumina," Am. Mineral. **62**, 747-755 (1977).
13. W. E. Cameron, "Composition and Cell Dimensions of Mullite," Am. Ceram. Soc. Bull., **56** [11] (1977).
14. W. M. Kriven and J. A. Pask, "Solid Solution Range and Microstructures of Grown Mullite," J. Am. Ceram. Soc., **66** [9] 649-654 (1983).
15. W. M. Kriven, R. A. Gronsky and J. A. Pask, "Dislocations and Low-angle Boundaries in Mullite," to be published.

SOLAR REFLECTOR COATINGS FOR SPACE APPLICATIONS

Yoshiro Harada and Mukund Deshpande
IIT Research Institute, 10 W. 35 St.
Chicago, IL 60616

INTRODUCTION

The optical characteristics of spacecraft surfaces are fundamental parameters in controlling its temperature. Passive thermal control coatings with designed solar absorptance and infrared emittance properties have been developed for various space conditions and environments. In this environment, the coatings must be stable and maintain their desired optical and mechanical properties for the course of a particular mission ranging up to a lifetime of thirty years.

In the early days of spacecraft materials' development, ultraviolet (UV) irradiation in vacuum testing was the principal means for evaluating optical stability. Additionally, the contributions of high energy electron and proton radiation, micrometeoroids and space debris, system-generated contamination and atomic oxygen (AO), were also recognized and addressed. The particularly degrading effects of AO have been observed from experiments on the Space Shuttle[1] and most recently from the Long Duration Exposure Facility (LDEF).

Our studies to develop spacecraft thermal control coatings for different missions have been directed primarily toward optical stability in this severe environment. In addition, our focus has been on coating systems which can be applied on relatively large surfaces under ambient conditions and also cured at room temperature. Maintaining the simplicity of the processing procedure was considered an important factor in obtaining desired materials reproducibility in optical and mechanical properties.

This paper reviews stable inorganic and polymeric materials which we have developed for different orbital missions, both near earth and geosynchronous. Physical characteristics of these coatings such as hardness, flexibility, and

MICROSTRUCTURE AND INTERFACIAL PROPERTIES OF LASER ABLATION COATED, FIBER-REINFORCED CERAMIC COMPOSITE

Dong Zhu, Helen Chung*, Mohammad H. Jilavi and Waltraud M. Kriven
Dept. of Materials Science and Engineering
*Dept. of Mechanical and Industrial Engineering
University of Illinois at Urbana-Champaign
Urbana, IL 61801

ABSTRACT

Titania (TiO_2), titanium aluminate ($TiO_2 \cdot Al_2O_3$), and enstatite ($MgSiO_3$) multilayer films were deposited on to a sapphire (Al_2O_3) fiber by the pulsed laser ablation technique using a KrF excimer laser. $MgSiO_3$ was used for the debonding interphase, and TiO_2 and $TiO_2 \cdot Al_2O_3$ were used to protect $MgSiO_3$ and Al_2O_3 from chemical reaction during processing and operation of composite. The composite was hot pressed by embedding coated fibers in Al_2O_3 matrix. SEM and EDS were used to analyze the microstructure and microcomposition of the coating layers before and after hot pressing. The partial decomposition of $MgSiO_3$ to SiO_2 glassy phase was observed during hot pressing. A push-out experiment was also conducted to determine interfacial properties of the hot pressed composite.

INTRODUCTION

Fiber coating is a key technique used in the fabrication of ceramic matrix composites. Pulsed excimer laser ablation (PELA) deposition is a newly developed technique for ceramic fiber coating [1]. The technique [2] uses high power UV laser radiation from a pulsed excimer laser as an external energy to vaporize solid target materials and to deposit thin films in a vacuum chamber. The whole deposition process, from surface heating by optical irradiation to plasma emission and deposition, is completed in nanoseconds to produce a smooth and stoichiometric coating. PELA has been successfully applied to deposit high Tc superconductor film [3, 4].

Recently, PELA was used to deposit graphite, SiC and $MgSiO_3$ on SiC and sapphire fibers [1] to show a uniform and dense coating. Potentially, PELA can be used as a large scale continuous coating technique.

$MgSiO_3$ is a potential debonding interphase for oxide composites. However, since it is not compatible with Al_2O_3, a multilayer coating system with isolating layers of TiO_2 was designed [5]. This work uses PELA to deposit multilayer coating of ceramics on sapphire fiber to develop a ceramic matrix composite with a weakened interphase. We studied the microstructure of coating layers and measured the mechanical properties of the composite.

EXPERIMENTAL PROCEDURE

2.1 Fiber and coating materials

The sapphire fibers (Saphikon, Inc., Milford, NH) were used in the work with a diameter of 125 μm. The continuous fibers were cut into about 5 cm length. The short fibers were washed in trichloroethylene to remove any trace of organic impurities, and subsequently washed alternatively in nitric acid and ammonium hydroxide to remove inorganic impurity. The final washing was done with DI water. The surface cleaned fibers were dried overnight in vacuum oven at 160°C.

In order to obtain a multilayer coating, TiO_2, TiO_2•Al_2O_3, and $MgSiO_3$ were used as coating materials respectively in this work. The commercial powders of TiO_2 and Al_2O_3 were ordered from Aldrich Chemical Co. (Milwaukee, WI) and Alcoa Co. (Pittsburgh, PA) respectively. The mechanical mixture with a molar ratio of 1:1 for the two powders was made by ball milling. Then the mixed powder was sintered at 1500°C for 2 hours followed by CIP. TiO_2 was sintered at 1400°C for 1 hr. $MgSiO_3$ powder was made from chemically derived powder, using basically the same procedure as in previous work [6]. $MgSiO_3$ was sintered at 1400°C for 1 hr.

2.2 Multilayer coating

The experimental apparatus for the pulsed laser ablation system for multi-layer, thin film deposition consisted of a stainless steel high vacuum chamber pumped by a turbomolecular pump with a base pressure of 10^{-7} Torr. A 45 ns pulse duration KrF excimer laser (Lambda Physik, EMG201 MSC) with 248 nm wavelength, 320 mJ pulse energy, and 10 Hz pulse repetition rate was focused to a spot size of 2.6 mm^2 on a disc-shaped target. The laser beam impact the target at an angle of 45° to the surface. The target disk with size of approximate 3 cm in diameter was rotated in 16 rpm during the process in order to achieve a uniform ablation rate.

Three different materials, *i. e.*, sintered TiO_2•Al_2O_3, TiO_2 and $MgSiO_3$ were used as targets. The fiber was single crystal Al_2O_3 (sapphire). The cleaned fibers were unidirectionally arranged in one plane and fixed with a tape at each ends. The space between the fibers was approximate 0.2 mm.

The fiber preform was moved into the vacuum chamber and was placed on a flat glass substrate, and faced to the target at a distance of about 1 cm. During the

coating process, the chamber was filled with oxygen gas to a few tens of millitorrs to suppress the oxide decomposition and compensate for oxygen loss. The coating was done discontinuously for each layer, *i.e.* after one side was coated, the fiber preform was flipped over to coat the other side. A total of 5 layers with 3 materials, TiO_2•Al_2O_3 / TiO_2 / $MgSiO_3$ / TiO_2 / TiO_2•Al_2O_3, were coated alternatively. The thickness of each layer could be controlled by adjusting the laser pulse repetition frequency. The resultant layers had a thickness of approximate 20 μm for $MgSiO_3$, and 10 μm for the other materials.

2.3 Composite and analysis

The coated fibers were embedded in Al_2O_3 powder and hot pressing was carried out at 1200°C for 1 hour under a pressure of 34 MPa in an argon atmosphere. The hot pressed composite was sliced to about 0.7 mm thickness perpendicular to the fiber direction. The cut sections were surface ground, and polished to a final finish of 1 μm.

The scanning electron microscopy (SEM, H-800, Hitachi, Japan) was conducted on coated fibers and polished sections of composite to determine the coating quality and microstructure. In order to determine the distribution of composition within coating layers, the BSE mode as well as EDS examination were used in the SEM analysis.

The interfacial properties of the composite were measured by the single-fiber push-out technique using a universal material testing machine (4502, Instron Co., Canton, MA) with a diamond punch.

The annealing procedure was at 1250°C for 5 hours after hot pressing, to determine the effect of annealing on interphase properties.

RESULTS AND DISCUSSION

3.1 Laser ablation coated sapphire fiber

The SEM morphology of a cross section of the as-multiple-coated fiber is shown in Fig. 1. The TiO_2• Al_2O_3 layers with thickness of approximate 8 μm are located between Al_2O_3 fiber or matrix and TiO_2 layers. They isolated TiO_2 and Al_2O_3 layers to avoid chemical reaction during hot pressing and annealing. The thickness of the TiO_2 layers was about 10 μm. The TiO_2 is chemically compatible with $MgSiO_3$ which was used as a weakening interphase in the composite. The thickness of $MgSiO_3$ layer was approximately 18 μm.

From Fig. 1, the densification and smoothness of coated layers was quite different from inside to outside. The inside TiO_2• Al_2O_3 layer showed a very uniform continuous circumferential coating and a smooth interface with the TiO_2 layer. The coating was dense and adhered well to both fiber and TiO_2 layer. The

inside TiO_2 layer seemed not so good as the inside TiO_2• Al_2O_3 layer. This layer was still quite dense. However, obvious radiated microcracks were observed. The surface of the layer appeared like periodic hills. The period corresponded to the distance between cracks.

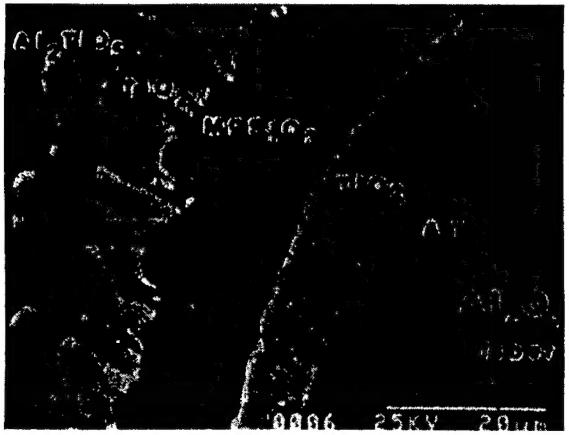

Fig. 1 The multiple layers coated by PELA on the sapphire fiber.

In this preliminary investigation, the target materials was ~ 1 cm from the fiber substrates, rather the ~ 30 cm from used in earlier experiment [1]. Therefore, unlike the two inside layers, the $MgSiO_3$ layer was not dense and contained numerous microcracks. The surface of the layer was rather rough. Large radiating cracks could be observed. These cracks and pores resulted in a corrugated surface which affected further deposition of next the two layers. The outside two layers were dense, but radiating cracks originally from the $MgSiO_3$ layer caused the coating to be rough and discontinuous. The final surface of the coated fiber was quite rough.

3.2 Microstructure of multilayer-coated, fiber-reinforced composite

Fig. 2 shows a BSE SEM micrograph as hot-pressed composite. Fig. 2 (a) is low magnification view of the cross section. The thickness of the coating layer was not uniform due to hot pressing. The shape of the coated fiber was changed to an overall circle, the short axis was parallel to the hot pressing direction. However, it was hard to distinguish the TiO_2• Al_2O_3 and TiO_2 layers. The thicknesses of inside layers were 3 ~ 5 μm, 8 ~ 20 μm for the $MgSiO_3$ layer and 5 ~ 15 μm for the outside layers.

Fig. 2 (b) is higher magnification view of the pressed composite. Some pores were observed within the $MgSiO_3$ layer. In the BSE mode, contrast appeared area indicating difference in composition within the deposited layer $MgSiO_3$.

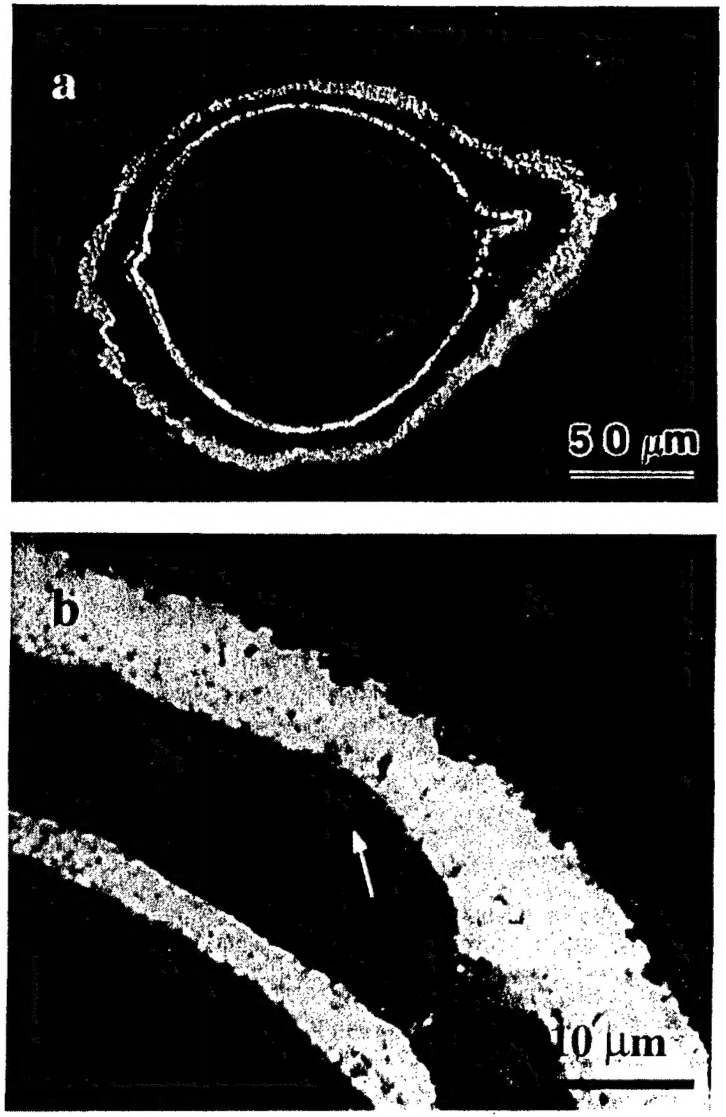

Fig. 2 SEM micrograph of multilayer-coated fiber in as-hot pressed composite.

3.3 Mechanical properties of the debonding interphase

Push-out testing of the hot pressed composite was conducted before and after annealing. The interfacial stress - displacement curves are shown in Fig. 3.

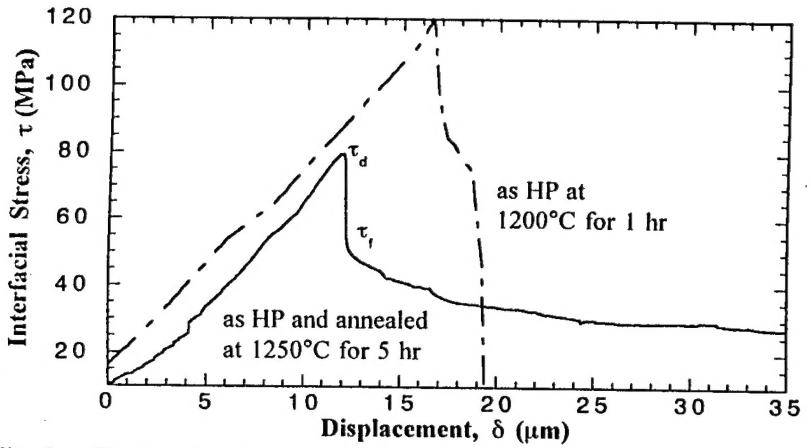

Fig. 3 The interfacial stress - displacement curves of push-out experiment.

The fiber of the as-hot pressed composite could not be pushed out until matrix broke at an interfacial stress reaching 120 MPa. After annealing at 1200°C for 5 hours, however, a typical interfacial stress - displacement behavior was recorded during push-out of a single fiber in the composite. The push-out curve consisted of a linear elastic loading and a non-linear loading of a fiber sliding against the matrix. The linear stage terminated at the interfacial strength $\tau_d \approx 80$ MPa where the load dropped catastrophically to a lower stress $\tau_f \approx 50$ MPa which corresponded to the beginning of relative sliding between the fiber and the matrix. Beyond this point the load decreased as the sliding fiber exited from the bottom side of the specimen. The $\tau_d \approx 80$ MPa was much lower than the maximum interfacial stress before annealing indicating that interphase weakening occurred during annealing.

3.4 Microcomposition of interphase

In order to determine the change in composition, microanalysis was applied to the coating layer after hot pressing. Fig. 4 shows energy - dispersive spctroscopy (EDS) spectra from the matrix to the fiber at different spots.

Figs. 4 (a) and (i) show the Al peak of Al_2O_3 in the fiber and matrix respectively. Either Al or Ti peaks appear in Fig. 4 (h) indicating the $TiO_2 \cdot Al_2O_3$ composition in the interfacial region. Only the Ti peak was detected in both Figs. 4 (b) and (f) corresponding to the stable TiO_2 layers after hot pressing. The composition of mixture was observed at interfacial regions between TiO_2 and $MgSiO_3$, as shown by peaks of Mg, Si and Ti in Figs. 4 (c) and (f). The result was caused by mixing up TiO_2 and $MgSiO_3$ during hot pressing.

Figs. 4 (d) and (e) show dark and bright regions respectively in the $MgSiO_3$ layer. In the bright region, both Mg and Si peaks revealed a $MgSiO_3$ composition as

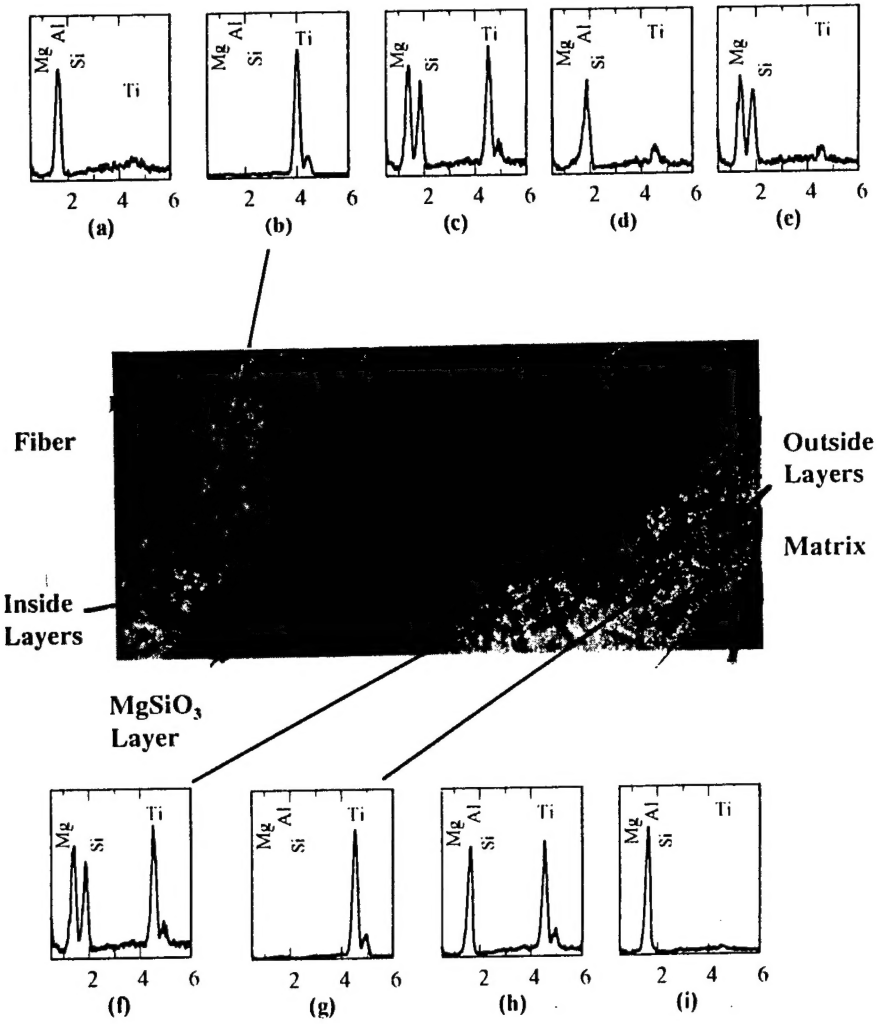

Fig. 4 Composition distribution along the coating layers.

shown in Fig. 4 (e). However, in the dark region nearby, only a Si peak appeared in Fig. 4 (d) indicating $MgSiO_3$ decomposition to SiO_2 during heat treatment. Although some SiO_2 was observed, the amount of glassy phase was very small. However, the glassy phase could increase on annealing. This is considered to contribute to interphase weakening during annealing.

SUMMARY

Multilayer coating was conducted on the sapphire fiber by pulse excimer laser ablation. $MgSiO_3$ was used as weakening interphase in the fiber reinforced composite. TiO_2 and TiO_2• Al_2O_3 were coated between the Al_2O_3 fiber and matrix to protect $MgSiO_3$ from chemical reaction with Al_2O_3 in the processing and application of the composite. The as-hot pressed composite was analyzed using SEM and EDS. The results showed that the TiO_2 coating layer remained stable after hot pressing. However, the $MgSiO_3$ layer was partially decomposed into SiO_2 glassy phase during processing. The push-out testing was performed to determine the effect of annealing on the mechanical properties of the interphase. The annealing resulted in interfacial strength decrease due to the decomposition of more glassy phase.

ACKNOWLEDGMENT

The work was supported by the US Air Force of Scientific Research, through Dr. Alexander Pechenike under Grant AFOSR-F49620-93-1-0227.

REFERENCES

[1] C. M. Huang, Y. Xu, F. Xiong, A. Zangvil and W. M. Kriven, "Laser ablated coatings on ceramic fibers for ceramic matrix composites", *Mater.Sci. & Eng.*, **A191**, 249 (1995)
[2] G. K. Hubler, "Pulsed laser deposition", *MRS Bull.*, **17**, [2], 26 (1990)
[3] D. Dijkkamp, T. Venkatesan, X. D. Wu, S. A. Shaheen, N. Jisrawi, Y. H. Min-Lee, W. L. McLean and M. Croft, "Proparation of Y-Ba-Cu oxide superconductor thin films using pulsed laser evaporation from high Tc bulk material", *Appl. Phys. Lett.*, **51**, 861 (1987)
[4] X. D. Wu, D. Dijkkamp, S. B. Ogale, A. Inam, E. W. Chase, P. E. Micelli, C. C. Chang, J. M. Tarascon and T. Venkatesan, "Epitaxial ordering of oxide superconductor thin film on (100) $SrTiO_3$ prepared by pulsed laser evaporation", *Appl. Phys. Lett.*, **51**, 861 (1987)
[5] W. M. Kriven, unpublished work, 1996
[6] C. M. Huang, D. H. Kuo, Y. J. Kim and M. W. Kriven, "Phase stability of chemically derived enstatite ($MgSiO_3$) powders", *J. Am. Ceram. Soc.*, **77**, [10], 2625 (1994)

THERMAL STABILITY AND CHEMICAL CORROSION RESISTANCE OF NEWLY DEVELOPED CONTINUOUS Si-Zr-C-O TYRANNO FIBER

Kiyoshi Kumagawa, Hiroyuki Yamaoka, Masaki Shibuya, Takemi Yamamura
Tyranno Fiber Development Project, Ube Industries Ltd., Ube City 755, Japan

ABSTRACT

A new continuous inorganic fiber, Si-Zr-C-O fiber, containing zirconium instead of titanium (Si-Ti-C-O fiber), has been successfully developed. This new Si-Zr-C-O fiber exhibits improved thermal stability and chemical corrosion resistance and has a decreased oxygen content. This reduction in oxygen content of Si-Zr-C-O fiber can be achieved by changing additives, from titanium alkoxide to a zirconium complex during the polymerization process of the precursor polymer. Continuous Si-Zr-C-O fiber "ZM" and "improved ZM" produced by oxidation curing had oxygen contents of 10 and 7.6 wt%, respectively. The oxygen content of "ZE" produced by electron beam curing was reduced to 1.7 wt%. The thermal stability and oxidation resistance of both ZM fiber and improved ZM fiber were superior to those of Si-Ti-C-O fiber (LoxE) produced by electron beam curing which has an oxygen content of only 5wt%. The crystalline grain growth of ZM fiber up to 1773K for 1 hour in argon gas and the level of decomposition of ZM fiber during heat treatment in CO gas at 1773K for 3 hours were very low in comparison with those of LoxM fiber (Si-Ti-C-O) by oxidation curing and LoxE fiber. Furthermore, concerning chemical corrosion resistance, when ZM and LoxM fibers were immersed in salt(NaCl) water and then heat treated at 1273K in air for 2 hours, LoxM fiber containing titanium was considerably damaged, but ZM fiber exhibited minimal damage.

INTRODUCTION

Si-Ti-C-O Tyranno Fiber has some good properties as a results of the presence of titanium. One is good weavability for use in 2D or 3D fabric due to the smaller diameter (8.5-12.5 microns), considerable elongation (1.7-2.2%) and longer length per spool of filaments (1000-2000m/spool). Another is high tensile strength (3.0-3.5GPa) due to the stability of the spinning process which is important in preventing damage to the surface of the fiber. These properties render the fiber suitable for low temperature usage, such as in plastic matrix composites (PMC), but not very suitable for high temperature usage, such as in ceramic matrix composites (CMC). Si-Ti-C-O fiber has also been developed by reducing the oxygen content of the fiber using an improved oxidation curing process (LoxM) or an electron beam curing process (LoxE). Recently Si-Ti-C-O